

# MECHANICS OF MATERIAL REMOVAL IN ABRASIVE JET MACHINING AND STUDY OF PROCESS PARAMETERS

By  
ADITYA PRASAD VERMA

MIE

1985

D

VER

MIEC

TH  
PR  
VERMA



DEPARTMENT OF MECHANICAL ENGINEERING

INDIAN INSTITUTE OF TECHNOLOGY KANPUR

JANUARY, 1985

# MECHANICS OF MATERIAL REMOVAL IN ABRASIVE JET MACHINING AND STUDY OF PROCESS PARAMETERS

A Thesis Submitted  
in Partial Fulfilment of the Requirements  
for the Degree of  
DOCTOR OF PHILOSOPHY

By  
ADITYA PRASAD VERMA

*to the*

DEPARTMENT OF MECHANICAL ENGINEERING  
INDIAN INSTITUTE OF TECHNOLOGY KANPUR  
JANUARY, 1985

1995 JUL 1997  
CENTRAL LIBRARY  

---

Acc. No. **A** 99168

Thesis  
621.91  
159m

ME-1995-D-VER-MEC

19/10/83  
22

# CERTIFICATE

This is to certify that the present work entitled 'MECHANICS OF MATERIAL REMOVAL IN ABRASIVE JET MACHINING AND STUDY OF PROCESS PARAMETERS' has been carried out under my supervision and has not been submitted else-where for the award of a degree.

G.K. Lal

G.K. Lal  
Professor  
Department of Mechanical Engineering  
Indian Institute of Technology, Kanpur  
(INDIA)

1-10-83



## ACKNOWLEDGEMENTS

I wish to express my deep sense of gratitude to my supervisor Dr. G.K. Lal, Professor, Department of Mechanical Engineering for his affectionate guidance throughout the course of this work.

I am extremely thankful to Dr. A.C. Jain, Professor, Department of Aeronautical Engineering for his valuable suggestions and discussions at various stages during the course of this work. I would like to express my sincere thanks to Dr. A.K. Ghosh, Dr. M.K. Muju, Department of Mechanical Engineering and Dr. D. Yadav, Department of Aeronautical Engineering for their assistance and suggestions in carrying out this work.

I wish to express my thanks to Dr. S.D. Shukla (Ex-Director) and Dr. A.K. Vashisht, Director, H.B. Technological Institute, Kanpur for their kind encouragements for the successful completion of this work.

I am thankful to Sri J. Singh, Sri R.M. Jha and Sri B.P. Bhartiya and Mr. Panna Lal for their assistance and cooperation which I received during the course of the experiments. I acknowledge with thanks the invaluable cheerful cooperation of Dr. S.J. Pande, Sri A.K. Srivastava Sri I.K. Bhat and Sri S.C. Srivastava for successful completion of this work.

I am thankful to Sri D.K. Sarker and Sri R.S. Shukla for making photographs of the experimental setup and Sri B.L. Arora, Sri S.S. Kushwaha and Sri G.K. Shukla for making the neat tracings. Thanks are also due to Sri J.P. Gupta for typing the manuscript and Sri Maiku Lal for cyclostyling.

Finally, I would like to put on record my appreciation for the unselfish encouragement which I received from my wife and love seeking children.

Aditya Prasad Verma

## TABLE OF CONTENTS

	<u>Page</u>
LIST OF TABLES	ix
LIST OF FIGURES	x
NOMENCLATURE	xix
SYNOPSIS	xxx
 CHAPTER 1 : INTRODUCTION AND REVIEW OF LITERATURE	 1
1.1 Introduction	1
1.1.1 Abrasive Jet Machining	2
1.1.2 Applications	3
1.1.3 Limitations	5
1.2 Variables in Abrasive Jet Machining	5
1.2.1 Carrier Fluid	6
1.2.2 Abrasives	7
1.2.3 Nozzle	9
1.2.4 Machining Variables	10
1.2.5 Work Material	12
1.3 Impact Erosion	12
1.3.1 Ductile Erosion	13
1.3.2 Brittle Erosion	23
1.4 Present Work	32

## CHAPTER 2 : THEORETICAL ANALYSIS OF ABRASIVE

PARTICLE VELOCITY	45
2.1 Introduction	45
2.2 Basic Assumptions	46
2.3 Aerodynamic Response Time	47
2.4 Behaviour of Particulate Flow	52
2.4.1 Equation of State	55
2.4.2 Continuity Equation	56
2.4.3 Limit of Continuum	
Approximation	57
2.4.4 Equation of Motion	60
2.4.5 Energy Equation	63
2.5 Particle Velocity in the Nozzle	64
2.5.1 Equation of Heat Transfer	
for Flow Over Spherical	
Particle	67
2.5.2 Dimensionless Variables	69
2.5.3 Flow Governing Equations in	
Dimensionless Form for the	
Gas-solid Particle Flow	
Through Nozzle	71
2.6 Particle Velocity in the Jet	75
2.6.1 Potential Core Length	80

Page

2.6.2	Flow Governing Equations of Gas-Solid Particle Free Jet	83
2.6.3	Flow Governing Equations in Dimensionless Form for Gas-Solid Particle Free Jet.	86
2.7	Numerical Solution Technique	88
CHAPTER 3	: THEORETICAL ANALYSIS OF MATERIAL REMOVAL RATE	92
3.1	Introduction	92
3.2	General Feature of Elastic-Plastic Indentation Fracture	93
3.3	Plastic Deformation Threshold	95
3.4	Quasi-Static Approach to Dynamic Impact	99
3.5	Mechanics of Erosion	100
3.5.1	Lateral Crack Depth	101
3.5.2	Lateral Crack Length	108
3.6	Material Removal Rate	113
CHAPTER 4	: EXPERIMENTS	122
4.1	Introduction	122
4.2	Experimental Set-up	122
4.3	Design Considerations	124

	<u>Page</u>
4.4 Preliminary Experiments	128
4.5 Experimental Conditions	131
4.6 Experimental Results	132
4.6.1 Erosion	133
4.6.2 Nozzle Wear	136
CHAPTER 5 : DISCUSSION	163
5.1 Erosion	163
5.2 Nozzle Wear	174
CHAPTER 6 : CONCLUSIONS AND SCOPE FOR FURTHER RESEARCH	184
6.1 Conclusions	184
6.2 Scope for Further Research	187
BIBLIOGRAPHY	188
APPENDIX I : Dimensionless Form of the Cross-sectional Area of Nozzle and its Derivative	198
APPENDIX II : Maximum Contact Force During Elastic Collision	203
APPENDIX III: Saltation Velocity for Horizontal Conveying	206
APPENDIX IV : Design of Mixing Chamber and Mixture Conveying Tube	212
APPENDIX V : Calculation of Mixture Ratio	214
APPENDIX VI : Particle Velocity Ratio at Nozzle Inlet	215
APPENDIX VII: Input Parameters for Theoretical Evaluation of Particle Velocity and Erosion Rate	217

## LIST OF TABLES

	<u>Page</u>
Table 1.1 : Typical applications of some commercial abrasives [After Bhattacharyya (4)].	35
Table 1.2 : Dimensions and nozzle life for various types of nozzles and nozzle materials [After Bhattacharyya (4)].	35
Table 3.1 : Elastic constants of different glasses [51] and $[\frac{E_t}{3(1-\nu_t)} - \frac{\nu_t}{Y_t}]^{1/3}$ values.	117
Table 3.2 : Lateral crack depth.	118
Table 5.1 : Values of the experimental constants $c_6$ and $c_7$ .	179

## LIST OF FIGURES

	<u>Page</u>
Figure 1.1 : Schematic diagram of abrasive jet machining.	36
Figure 1.2 : Effect of gas pressure on material removal rate [After Bhattacharyya (4)].	37
Figure 1.3 : Variation of maximum material removal rate with grain size at various pressures for SiC abrasive (a) $14.7 \times 10^6$ N/m <sup>2</sup> , (b) $29.4 \times 10^6$ N/m <sup>2</sup> and (c) $39.6 \times 10^6$ N/m <sup>2</sup> [After Neema and Pandey (6)].	38
Figure 1.4 : Variation of maximum axial velocity of particle with length to diameter ratio of the nozzle for different nozzle exit diameters (a) 6 mm, (b) 9 mm and (c) 12 mm [After Wolak et al. (7)].	39
Figure 1.5 : Variation of maximum axial velocity of particle with the nozzle length for different nozzle diameters and loading ratios [After Wolak et al. (7)].	40
Figure 1.6 : Effect of stand-off distance on material removal rate [After Sarkar and Pandey (5)].	41



- Figure 1.7 : Weight removal as a function of particle impingement angle for (a) plate glass and (b) 1100-0 aluminium eroded by 120 mesh (127  $\mu\text{m}$ ) grit of angular silicon carbide. Particle velocity : 500 fps [After Sheldon and Finnie (11)]. 42
- Figure 1.8 : Effect of pressure on material removal rate for different work materials (a) cemented carbide and (b) glass. Abrasive : aluminium oxide; particle size : 40  $\mu\text{m}$  [After Sarkar and Pandey (5)]. 43
- Figure 1.9 : Volume removal as a function of the hardness for metals eroded at  $\theta = 20^\circ$  and velocities of 76 m/sec and 137 m/sec.  $d_p$  : 250  $\mu\text{m}$  SiC [After Finnie et al. (10)]. 44
- Figure 2.1 : Effectiveness of momentum transfer from solid particles to the gas [After Soo (90)]. 91
- Figure 2.2 : Velocity profile of air jet spreading [After Abramovich (104)]. 91

- Figure 3.1 : Schematic diagram of the cracking occurring during a loading-unloading cycle with a small spherical indenter. 119
- Figure 3.2 : Pressure distribution at contact area (a) elastic impact (b) elastic-plastic impact. 120
- Figure 3.3(a) : Load, crack length data for radial, median and lateral cracks in zinc sulphide, obtained for a spherical indenter, 800  $\mu\text{m}$  dia. [After Evans and Wilshaw (50)]. 121
- Figure 3.3(b) : Normalized lateral crack length as a function of the normalized fracture toughness [After Evans and Wilshaw (50)]. 121
- Figure 4.1 : Schematic layout of abrasive jet machining set-up. 139
- Figure 4.2(a) : Experimental set-up of abrasive jet machining. 140
- Figure 4.2(b) : Photograph of mixing chamber, secondary abrasive chamber and vibrator unit. 141

Figure 4.3 : Calibration curves of abrasive flow rate for different particle sizes (a) 25  $\mu\text{m}$ , (b) 30  $\mu\text{m}$ , (c) 38  $\mu\text{m}$  and (d) 48  $\mu\text{m}$ . 142

Figure 4.4 : Nozzle wear profiles (a) initial profile, (b) after 5 min, (c) after 10 min, (d) after 15 min and (e) after 20 min.  
Hardness : 50 HRc;  $d_{\text{no}}$  : 0.78 mm;  $l_n$  : 4.5 mm;  $\beta$  :  $30^\circ$ ;  $d_p$  : 38  $\mu\text{m}$ ;  $\alpha$  : 0.201. 143

Figure 4.5 : Variation of nozzle wear volume with operating time (a) wear volume from inlet and exit diameters and (b) wear volume from difference of weight. Hardness: 10 HRc;  $d_{\text{no}}$  : 0.78 mm;  $l_n$  : 6.35 mm;  $\beta$  :  $30^\circ$ ;  $d_p$  : 30  $\mu\text{m}$ ;  $\alpha$  : 0.154. 144

Figure 4.6 : Variation of material removal rate and penetration rate with stand-off distance. (a) Volumetric material removal rate and (b) Penetration rate.  $d_p$  : 30  $\mu\text{m}$ ;  $\alpha$  : 0.148; nozzle pressure : 147.15  $\text{kN/m}^2$  (gauge); cutting time : 60 sec. 145

Figure 4.7 : Machined cavity profile at different stand-off distances (a) 2 mm, (b) 6 mm, (c) 10 mm, (d) 14 mm, (e) 16 mm and (f) 20 mm.  $d_p$  : 30  $\mu\text{m}$ ;  $\alpha$  : 0.148; nozzle pressure: 147.15  $\text{kN/m}^2$  (gauge); cutting time : 60 sec. 146

Figure 4.8 : Variation of material removal rate with stand-off distance for different mixture ratios (a) 0.095, (b) 0.148, (c) 0.201 and (d) 0.268.  $d_p$  : 30  $\mu\text{m}$ ; nozzle pressure: 147.15  $\text{kN/m}^2$  (gauge). 147

Figure 4.9 : Variation of penetration rate with stand-off distance for different mixture ratios (a) 0.095, (b) 0.148 and (c) 0.268.  $d_p$  : 30  $\mu\text{m}$ ; nozzle pressure: 147.15  $\text{kN/m}^2$  (gauge). 148

Figure 4.10: Variation of top diameter of the machined cavity with stand-off distance for different mixture ratios (a) 0.095, (b) 0.148, (c) 0.201 and (d) 0.268.  $d_p$ : 30  $\mu\text{m}$ ; nozzle pressure : 147.15  $\text{kN/m}^2$  (gauge). 149

Figure 4.11: Variation of volume erosion factor with stand-off distance for different particle sizes (a) 25  $\mu\text{m}$ , (b) 30  $\mu\text{m}$ , (c) 38  $\mu\text{m}$  and (d) 48  $\mu\text{m}$ . Nozzle pressure : 147.15  $\text{kN/m}^2$  (gauge). 150

Figure 4.12: Variation of optimum material removal rate with mixture ratio for different particle sizes (a) 25  $\mu\text{m}$ , (b) 30  $\mu\text{m}$ , (c) 38  $\mu\text{m}$  and (d) 48  $\mu\text{m}$ . Nozzle pressure : 147.15  $\text{kN/m}^2$  (gauge); stand-off distance : 16 mm. 151

Figure 4.13 : Variation of penetration rate with stand-off distance for different particle sizes (a) 25  $\mu\text{m}$ , (b) 30  $\mu\text{m}$  and (c) 48  $\mu\text{m}$ .  $\alpha$  : 0.148; nozzle pressure : 147.15  $\text{kN/m}^2$  (gauge).

152

Figure 4.14 : Variation of material removal rate with nozzle pressure for different mixture ratios (a) 0.052, (b) 0.088, (c) 0.109 and (d) 0.143.  $d_p$  : 30  $\mu\text{m}$ ; stand-off distance : 16 mm.

153

Figure 4.15 : Variation of diametral wear rate with nozzle length for different operating times (a) 6 min, (b) 9 min, (c) 12 min, (d) 15 min and (e) 18 min. Hardness : 10 HRc;  $d_{no}$  : 0.78 mm;  $l_n$  : 6.3 mm;  $\beta$  :  $30^\circ$ ;  $d_p$  : 30  $\mu\text{m}$ ;  $\alpha$  : 0.154.

154

Figure 4.16 : Variation of the wear index with the operating time for different nozzle length to exit diameter ratios (a) 8.41, (b) 10.47, (c) 12.88 and (d) 16.68. Hardness: 50 HRc;  $d_{no}$  : 0.97 mm;  $\beta$  :  $30^\circ$ ;  $d_p$  : 38  $\mu\text{m}$ ;  $\alpha$  : 0.201.

155

Figure 4.17 : Variation of the wear index with the nozzle length to exit diameter ratio for different operating times (a) 5 min, (b) 10 min and (c) 15 min. Hardness: 50 HRc;  $d_{no}$  : 0.97 mm;  $\beta$  :  $30^{\circ}$ ;  $d_p$  : 38  $\mu$ m;  $\alpha$  : 0.201.

156

Figure 4.18 : Variation of the wear index with the operating time for different nozzle exit diameters (a) 1.62 mm, (b) 1.17 mm, (c) 0.9 mm and (d) 0.8 mm. Hardness : 50 HRc;  $l_n$  : 12 mm;  $\beta$  :  $30^{\circ}$ ;  $d_p$  : 38  $\mu$ m;  $\alpha$ :0.201.

157

Figure 4.19 : Variation of the wear index with the nozzle diameter for different operating times (a) 5 min, (b) 10 min and (c) 15 min. Hardness : 50 HRc;  $l_n$  : 12 mm;  $\beta$  :  $30^{\circ}$ ;  $d_p$  : 38  $\mu$ m;  $\alpha$  : 0.201.

158

Figure 4.20 : Variation of the wear index with the operating time for different entrance angles (a)  $120^{\circ}$ , (b)  $90^{\circ}$  and (c)  $60^{\circ}$ . Hardness : 50 HRc;  $d_{no}$  : 0.96 mm;  $l_n$  : 5.28 mm;  $d_p$  : 38  $\mu$ m;  $\alpha$  : 0.201.

159

Figure 4.21 : Variation of the wear index with the operating time for different mixture ratios (a) 0.096, (b) 0.088, (c) 0.201 and (d) 0.249. Hardness : 50 HRc;  $d_{no}$ : 0.97 mm;  $l_n$  : 8.16 mm;  $\beta$ : $30^{\circ}$ ;  $d_p$ :38  $\mu$ m. 160

Figure 4.22 : Variation of the wear index with the mixture ratio for different operating times (a) 5 min, (b) 10 min and (c) 15 min. Hardness: 50 HRc;  $d_{no}$ : 0.97 mm;  $l_n$ : 8.16 mm;  $\beta$  :  $30^{\circ}$ ;  $d_p$  : 38  $\mu$ m. 161

Figure 4.23 : Variation of the wear index with the operating time for different particle sizes (a) 30  $\mu$ m and (b) 38  $\mu$ m. Hardness: 50 HRc;  $d_{no}$ : 0.97 mm;  $l_n$ : 8.16 mm;  $\beta$  :  $30^{\circ}$ ;  $\alpha$  : 0.201. 162

Figure 5.1 : Variation of  $\lambda$  with dimensionless stand-off distance for different mixture ratios (a) 0.095, (b) 0.148, (c) 0.201, (d) 0.268 and (e) mean curve.  $d_p$ : 30  $\mu$ m; nozzle pressure : 147.15 kN/m<sup>2</sup> (gauge). 180

- Figure 5.2 : Variation of theoretical as well as experimental volumetric material removal rate with stand-off distance for different mixture ratios (a) 0.095, (b) 0.148, (c) 0.201 and (d) 0.268.  $d_p$ : 30  $\mu\text{m}$ ; nozzle pressure : 147.15  $\text{kN/m}^2$  (gauge). 181
- Figure 5.3 : Theoretical estimate of (a) abrasive particle velocity and (b) carrier fluid velocity at different sections of the nozzle.  $d_{no}$ : 0.97 mm;  $l_n$ : 16.18 mm;  $\beta$  :  $30^\circ$ ;  $d_p$  : 38  $\mu\text{m}$ ;  $\alpha$  : 0.201. 182
- Figure 5.4 : Theoretical estimate of abrasive particle velocity at different sections of the nozzle for various exit diameters (a) 1.62 mm, (b) 1.17 mm, (c) 0.9 mm and (d) 0.8 mm.  $l_n$  : 12 mm;  $\beta$  :  $30^\circ$ ;  $d_p$ : 38  $\mu\text{m}$ ;  $\alpha$  : 0.201. 183
- Figure I.1 : Geometry of convergent-straight nozzle. 202
- Figure III.1: Saltation velocity  $(u_{gs})_{\min}$  of uniform sized solid particles in a 6.35 cm ID tube [After Zenz (115)]. 211



## NOMENCLATURE

$a_f$	radius of curvature of fractured space
$a_e$	radius of projected area of elastically deformed contact
$a_p$	radius of projected area of plastically deformed contact
$(a_p)_{\max}$	maximum value of the radius of projected area of plastically deformed contact
$a_t$	radius of projected area of total contact
$A_{0-5}$	constants, appear in various places in text
$\Delta A_c$	infinite-simal cross-sectional area in the centre of potential core
$A_n$	cross-sectional area of nozzle
$A_{n1}$	cross-sectional area of nozzle at inlet
$A_p$	mean particle projected area
$A_{sp}$	mean particle surface area
$b$	thickness of the mixing zone of submerged jet
$b_l$	thickness of the mixing zone at the end of potential core of submerged jet
$B$	time constant of particle-fluid momentum transfer
$B^{\text{jet}}$	time constant of particle-fluid momentum transfer in the jet

$c_{1-7}$	constants, appear in various places in text
$c_{pg}$	specific heat of carrier fluid at constant pressure
$c_{pp}$	specific heat of solid particle material
$c_s$	particle velocity ratio at nozzle inlet
$C_o$	size of plastic zone
$C_d$	corrected drag coefficient
$C_{ds}$	Stokes drag coefficient
$C_l$	lateral crack length
$d_n$	nozzle diameter
$d_{n1}$	nozzle diameter at inlet
$d_{n2}$	nozzle diameter at the end of I convergent region
$d_m$	diameter of mixing chamber
$d_p$	particle diameter
$ds$	distance travelled by particle in time $dt$
$d_t$	tube diameter
$d_{mt}$	diameter of mixture conveying tube
$d_{no}$	nozzle exit diameter
$d_{pc}$	critical diameter of particle for elastic-plastic deformation
$D_g$	dilation tensor for fluid phase
$D_p$	dilation tensor for particle phase

$E_p$	modulus of elasticity of particle material
$E_t$	modulus of elasticity of target (workpiece) material
$f_{1-4}$	dimensionless functions
$f_c$	correction factor to Stokes drag formula
$f_{ogi}$	component of body force on fluid phase
$f_{bpi}$	component of body force on particle phase
$F_e$	contact force during elastic collision
$(F_e)_{\max}$	maximum contact force during elastic collision
$F_p$	contact force during plastic indentation
$(F_p)_{\max}$	maximum contact force during plastic indentation
$g$	function of concentration profile
$g_c$	acceleration due to gravity
$G_t$	shear modulus of target (workpiece) material
$h$	coefficient of heat transfer between the particles and the carrier fluid
$H_t$	Vicker's hardness of target material
$k_g$	coefficient of thermal conductivity for the gas phase
$k_p$	coefficient of thermal conductivity for the particle phase
$K$	stress intensity factor of target (workpiece) material
$K_c$	fracture toughness of target (workpiece) material

$K_m$	effectiveness of particle medium
$l_1$	distance from inlet to the end of I convergent region of the nozzle
$l_2$	distance from inlet to the end of II convergent region of the nozzle
$l_n$	nozzle length
$L$	characteristic length of the flow system
$m$	Weibull's constant
$m_p$	mass of particle
$\dot{M}$	mass flow rate of mixture
$\dot{M}_g$	mass flow rate of gas
$M_p$	mass of impacting particles
$\dot{M}_p$	mass flow rate of particles
$n_{1-3}$	exponents, appear in various places in text
$n_p$	number density
$N_p$	number of impacts per unit time
$N_{Nu}$	Nusselt number
$N_{Pr}$	Prandtl number
$N_{Re}$	particle Reynolds number
$N_{Re}^{jet}$	particle Reynolds number in jet region
$P$	pressure of gas-particle mixture

$P_l$	pressure of gas-particle mixture at nozzle inlet
$P_g$	partial pressure of gas phase
$P_p$	partial pressure of particle phase
$q_{av}$	average surface pressure during elastic collision
$q_{max}$	maximum surface pressure during elastic collision
$\tilde{Q}$	volume fraction of solid particles
$r_f$	fictitious radius of curvature of indenting particle
$r_p$	radius of impacting particle
$R$	ratio of vertical and horizontal force components acting on cutting tip of particle
$R_g$	gas constant
$S_K$	Stokes number
$t$	time
$t_g$	time for the motion following fluid path
$t_p$	time for the motion following particle path
$T_g$	temperature of fluid
$T_p$	temperature of particle
$T_{gl}$	temperature of fluid at nozzle inlet
$T_{pl}$	temperature of particles at nozzle inlet
$u_g$	velocity of fluid
$u_p$	velocity of particle

$u_{go}$	velocity of fluid at nozzle exit
$u_{gl}$	velocity of fluid at nozzle inlet
$u_{gc}$	centre line velocity of fluid-phase at the end of potential core
$u_{gi}$	$i$ th component of the velocity of fluid-phase
$u_{pi}$	$i$ th component of the velocity of the particle phase
$u_{pc}$	threshold velocity
$u_{pe}$	elastic impact velocity
$u_{Gm}$	centre line velocity of fluid (air) in air-abrasive jet
$u_{pm}$	centre line velocity of particles in air-abrasive jet
$u_{gs}$	saltation velocity for horizontal conveying of solid particles
$(u_{gs})_{\min}$	minimum saltation velocity for horizontal conveying of solid particles
$(u_{gs})'_{\min}$	corrected minimum saltation velocity for horizontal conveying of solid particles
$u_{gch}$	minimum velocity of carrier fluid for vertical conveying of solid particles
$u_{gst}$	minimum safe velocity of carrier fluid in the mixture conveying tube
$u_{pim}$	particle impingement velocity

$u_{pimn}$	normal component of particle impingement velocity
$u_{pimt}$	tangential component of particle impingement velocity
$v'_{pimt}$	residual tangential component of particle impingement velocity
$U$	characteristic velocity
$v$	volume of erosion per impact
$V$	volume of erosion
$V_c$	cutting wear volume
$V_d$	deformation wear volume
$V_r$	volumetric material removal rate
$W^*$	wear index
$W_d$	diametral wear rate
$x$	distance considered in the direction of flow
$x_c$	potential core length
$x_d$	stand-off distance
$x_i$	$i$ th component of the space coordinate
$X_e$	elastic impact energy
$X_p$	plastic deformation work
$X_{im}$	impact energy of impinging particle
$y_l$	ordinate of the inner edge of the boundary layer at the end of the potential core

$\gamma_t$	yield stress of target material in simple tension
$z_e$	elastic penetration depth
$z_l$	lateral crack depth
$z_m$	maximum depth of indentation
$z_p$	depth of concavity due to plastic deformation
$z_t$	total deformation depth during elastic-plastic impact
$(z_p)_{\max}$	maximum depth of concavity due to plastic deformation
$\alpha$	mixture ratio
$\beta$	semi-entrance angle of the nozzle
$\beta_1$	semi-entrance angle for I convergent region of the nozzle
$\beta_2$	semi-entrance angle for II convergent region of the nozzle
$\Gamma_g$	energy source for the mixture
$\Gamma_p$	energy source for the particle
$\delta$	boundary layer thickness for flow over a sphere
$\delta_{ji}$	Kronecker delta
$(\Delta_g)_{ji}$	deformation tensor for fluid phase
$(\Delta_p)_{ji}$	deformation tensor for particle phase
$\varepsilon_c$	cutting wear factor



$\epsilon_d$	deformation wear factor
$\epsilon_v$	volume erosion factor
$\zeta_g$	bulk viscosity of fluid phase
$\zeta_p$	bulk viscosity of particle phase
$\eta$	concentration profile
$\theta$	impingement angle
$\theta_o$	limiting value of impingement angle
$\lambda$	particle-particle interaction function
$\mu_g$	viscosity of the gas phase in the mixture
$\bar{\mu}_g$	viscosity of the fluid phase material
$\mu_m$	viscosity of mixture
$\mu_p$	viscosity of particle phase in the mixture
$\nu_p$	Poisson's ratio for particle material
$\nu_t$	Poisson's ratio for target (workpiece) material
$\rho_g$	bulk density of fluid phase
$\bar{\rho}_g$	density of fluid phase material
$\bar{\rho}_{go}$	density of fluid phase material at nozzle exit
$\bar{\rho}_{gs}$	density of fluid phase material in the mixing chamber
$\rho_m$	density of mixture in the boundary layer of the gas-solid mixture jet

$\rho_{mo}$	density of mixture in potential core of the gas-solid mixture jet
$\rho_p$	bulk density of particle phase
$\hat{\rho}_p$	material density of the particle
$\sigma_o$	Weibull's constant
$\sigma_f$	flow stress of the target material
$\sigma_{st}$	shear stress at yielding in simple tension
$\sigma_{yt}$	elastic load limit for target material
$\tau_f$	characteristic time of the flow system
$\tau_p$	particle relaxation time
$\gamma$	coefficient of friction at the indenter and target interface
$\emptyset$	particle concentration in the jet
$\emptyset_o$	particle concentration at the nozzle exit
$\Psi_p$	source function of particles
$\Omega$	material constant (ratio of target hardness to yield stress)

### Subscripts

$_{ji}$  tensor

### Superscripts

\* dimensionless, reduced, or characteristic quantities.

## Mathematical Symbols and Operations

$\propto$  means proportional

$<$  means less than

$\leq$  means equal to or less than

$\geq$  means equal to or greater than

$\approx$  means approximately equal

## SYNOPSIS

### MECHANICS OF MATERIAL REMOVAL IN ABRASIVE JET MACHINING AND STUDY OF PROCESS PARAMETERS

A Thesis Submitted  
in Partial Fulfilment of the Requirements  
for the Degree of  
DOCTOR OF PHILOSOPHY

by

ADITYA PRASAD VERMA

to the

DEPARTMENT OF MECHANICAL ENGINEERING  
INDIAN INSTITUTE OF TECHNOLOGY KANPUR

JANUARY, 1985

In Abrasive Jet Machining (AJM) fine-grained abrasive particles mixed in suitable proportion with high pressure carrier gas, usually air, are directed through a suitably designed nozzle. The nozzle imparts high velocity to the carrier gas and thereby to the abrasive particles at the nozzle exit. This high velocity air-abrasive mixture jet is then directed onto the workpiece surface. Material removal occurs due to erosion caused by the impact of high velocity abrasive particles onto the workpiece.

Literature survey reveals that erosion caused by impact of solid particles entrained in a fluid stream is a complex phenomenon and is not fully understood. Further, adequate data of its governing parameters are not available. Some of these parameters are interdependent and difficult to control. The erosion study in such situations involves determination, from the fluid flow conditions, of the number, direction and velocity of abrasive particles striking onto the workpiece surface and then the estimation of material removed from the workpiece. In the present work an attempt has been made to carryout theoretical as well as experimental study of the erosion phenomena in AJM.

In the first phase of the present study, the flow governing equations in dimensionless form for two-phase flow in the nozzle as well as jet region have been developed. These non-linear differential and algebraic equations have been solved to estimate the velocity of abrasive particles in the air-abrasive jet.

During solid particle impacts, erosion loss in brittle materials occurs due to intersection of lateral cracks from adjacent impacts. These cracks are produced on the workpiece below the impact site due to the residual stress field. Considering a quasi-static approach and using semi-empirical fracture mechanics relationships, the expressions for lateral

crack length ( $C_1$ ) and lateral crack depth ( $z_1$ ) have been obtained in terms of various impact parameters in the second phase of the work. Subsequently, a theoretical model of material removal rate has been developed.

In polishing, deburring and other finishing operations the volume of eroded material is of importance, while in micro-drilling and cutting operations it is the erosion depth (depth of penetration) which is more relevant. In the third phase of the study, experimental investigations have been carried out to investigate the effects of input parameters such as grain size, mixture ratio, nozzle pressure, stand-off distance etc. on the volumetric material removal rate, penetration rate, eroded cavity diameter etc. For this purpose an experimental Abrasive Jet Machine has been designed and fabricated which provides for precise control of various input parameters.

The performance characteristics of machining operations in AJM also depend on the nozzle geometry. The nozzle imparts high velocity to the expanding carrier fluid (air) and thereby to the abrasive particles. High velocity air-abrasive particle mixture while expanding causes wear at the inner surface of the nozzle. Nozzle wear is, therefore, of interest not only from the point of view of cost but also from the point of view of characteristic performance of the unit and

machining accuracy. In the fourth phase of the study, experiments have been carried out to investigate the effects of nozzle diameter, nozzle length and entrance angle on nozzle wear. Other parameters which have been considered are mixture ratio and abrasive particle size. Experiments have also been carried out with split nozzles to examine the wear profile of the inside nozzle surface.

Experimental results indicate that both volumetric material removal rate and penetration rate depend on stand-off distance, mixture ratio, nozzle pressure and grain size. Both volumetric material removal rate as well as penetration rate first increase with increase in stand-off distance and then decrease giving an optimum value. Theoretical curves also indicate this and there appears qualitative agreement between the two. The experimental results further reveal that the maximum values of material removal rate and penetration rate occur at different values of stand-off distance, with maximum material removal rate occurring at a higher value. This indicates that operations such as deburring and finishing should be carried out at larger stand-off distances, whereas smaller stand-off distances should be chosen for micro-drilling etc.

Experiments on nozzle wear indicate that wear increases when nozzle length is increased and when nozzle diameter and entrance angle are decreased. Increase in mixture ratio

and size of the abrasive particles also increase the wear rate.

In the concluding portion of the work, the theoretical as well as experimental results are discussed in detail in order to understand the basic mechanics involved in the process.



## CHAPTER 1

### INTRODUCTION AND REVIEW OF LITERATURE

#### 1.1 Introduction

Recent advances in science and technology specially in the areas of nuclear and aerospace engineering have imposed a severe demand on the material requirements. As a result of this, the metallurgists and material scientists have been continuously developing newer and larger varieties of materials. These materials are of increasingly higher strength and are harder and difficult to machine. The advent of such high strength, temperature resistant, hard and brittle materials posed the serious problems to the manufacturing engineers. Besides, the processing of the parts with higher accuracies and complicated shapes have also been difficult, time consuming and uneconomical by conventional techniques of machining. In view of the seriousness of these problems the need for developing newer concepts in machining was emphasized [1].

To meet these challenges several new manufacturing processes have been developed during the last two decade or so. Unlike the conventional machining processes these processes are not affected by hardness, toughness or brittleness of the material. Further, these processes can produce intricate shapes with high degree of accuracy on any workpiece material through suitable control of the various physical parameters of the process. The newer machining processes

so developed are often called 'Unconventional Machining Processes' or 'Modern Machining Processes'. These are unconventional in the sense that they do not employ conventional tools for material removal, instead energy in its direct form is utilized.

The underlying principle of these modern machining processes is to apply some sort of energy, namely mechanical, electrical, chemical, thermal, or magnetic, to the workpiece directly and have the desired shape transformation or material removal from the work surface through use of known scientific principles. One of these new technological processes involves material removal by erosion or abrasion due to surface impact of hard particles (abrasives). The erosion of work material by impact of abrasive particles necessitates pneumatic or hydraulic pressure and fluid stream for carrying these abrasive particles. The process employing this mechanism of material removal is the Abrasive Jet Machining (AJM).

#### 1.1.1 Abrasive Jet Machining

Abrasive jet machining is a process in which material removal takes place due to the erosive action of a stream of fine grained abrasive particles impacting at high velocity onto the work surface. Fine grained abrasive particles are

fed in suitable proportion from an abrasive feeder into the mixing chamber where it is mixed with high pressure gas or air (from compressor). The mixture of air and abrasive is directed through a pipe to a suitably designed nozzle. The nozzle and the nozzle holder are attached to a nozzle feed device to adjust and locate the nozzle with reference to the work surface to be machined. The nozzle tip is held at a certain distance from the workpiece and in a definite orientation, generally normal to the surface to be machined. The distance between the nozzle tip and the workpiece surface is generally called the stand-off distance. The nozzle used imparts high velocity to the expanding carrier fluid and thereby to the jet of abrasive particles at the nozzle exit. This high velocity air-abrasive jet is directed onto the work surface to be machined. Material removal occurs due to erosion caused by the impact of high velocity abrasive particles onto the work surface. The schematic diagram of abrasive jet machining is shown in Fig. 1.1.

#### 1.1.2 Applications

Abrasive jet machining process finds its successful application for machining of hard and brittle materials. The process can also be used for machining of complicated shapes and contours. Due to absence of heat during machining,

this process has been found particularly suitable for machining of heat sensitive materials. Lavoie [2] and Ingulli [3] have mentioned a number of interesting applications of this process. Some of these are summarized below.

- (1) Clearing corrosion, oxides, dirt and other contaminants from such diverse type of parts as electronic components and leather artifacts.
- (2) Trimming of resistors to specified values.
- (3) Cutting and micro-drilling of thin sectioned fragile components made of glass, germanium, refractories, ceramics, mica etc.
- (4) Etching of trade marks, identifying numbers or other markings on machined items.
- (5) Polishing of plastic, nylon and teflon components.
- (6) Removing of parting lines and flashings from moulded parts and cleaning of intricate mould cavities.
- (7) Deburring holes which are virtually impossible to achieve by conventional deburring tools.
- (8) Frosting of interior surfaces of glass-tubes.
- (9) Reproducing of designs on a glass surface with the help of masks made of rubber, copper etc.
- (10) Cutting of very hard materials such as diamond etc.

### 1.1.3 Limitations

The application of the process is limited by the following considerations:

- (1) The capability of the process is limited because of low material removal rate (material removal rate for machining of glass has been reported to be approximately 40 gm/min. or  $0.0164 \text{ cm}^3/\text{min.}$  [4]).
- (2) The tapering effect is inherent characteristic of the process because of unavoidable flaring of the abrasive jet.
- (3) The accuracy of the process is also affected by stray cutting which again is difficult to avoid.
- (4) Abrasive may get embedded in the work surface.

### 1.2 Variables in Abrasive Jet Machining

The variables which influence the material removal rate, surface finish and accuracy of machining in AJM have been summarized below.

- (a) Carrier fluid :
  - (i) pressure,
  - (ii) viscosity and
  - (iii) density,

(b) Abrasive :

- (i) type of abrasive grain and
- (ii) size of abrasive grain,

(c) Nozzle :

- (i) geometry of the nozzle (i.e. length, diameter, entrance angle etc.) and
- (ii) nozzle material,

(d) Machining variables :

- (i) stand-off distance,
- (ii) shape of cut,
- (iii) angle of impingement,
- (iv) mixture ratio and
- (v) jet velocity,

(e) Work material.

### 1.2.1 Carrier Fluid

The carrier fluid used in AJM should be non-toxic, cheaply available and capable of being dried and cleaned without any difficulty. For better accuracy and efficient machining it should be of less flaring characteristic after discharging from the nozzle exit. The carrier fluid which can be used are air, carbon dioxide, or nitrogen.

The air is most widely used because of its cost and easy availability. Even clean and dry shop air, directly from the air lines, can be used after suitable filtering.

The pressure of the carrier fluid influences the material removal rate in AJM. For machining of glass with aluminium oxide abrasive Bhattacharyya[4] has found that the material removal rate first increases linearly and then tends to saturate with further increase in pressure (Fig. 1.2). A similar effect has been reported by Sarkar and Pandey [5]. In the existing literature on the subject, no mention has been made about the influence of viscosity and density of the carrier fluid on material removal rate. It is, however, believed that a low viscous and lighter fluid would give higher material removal rate in comparison with heavy gas or fluid.

### 1.2.2 Abrasives

The choice for abrasive type depends upon the type of machining (roughing or finishing), cost of machining, properties of workpiece material, type of operation etc. The abrasive grain should be sharp and irregular for better cutting action and fine enough to remain in suspension with the carrier fluid. For cutting purposes aluminium oxide and silicon carbide abrasives are generally used. For

deburring, polishing and cleaning purposes dolomite, glass beads etc. are most suitable. Sodium bi-carbonate being hygroscopic is rarely used for light finishing operations. The working temperature with sodium bi-carbonate abrasive should be kept below  $50^{\circ}\text{C}$  above which it will loose water and the exit velocity from the nozzle will be reduced. Re-use of abrasive is not recommended because of decreased cutting ability and contamination with the abraded particles of the work material may cause clogging of nozzle passage.

Material removal rate in AJM depends upon the size and shape of the abrasive grain. Coarse grain being more irregular have better cutting action compared to fine grain abrasive. Also, fine grain abrasives having sticking characteristic make the flow irregular and increase the choking tendency in the nozzle and flow system. The most favourable grain sizes for AJM are 10 to 50  $\mu\text{m}$ . Neema and Pandey [6] have shown that for an specified machining condition there exists an optimum grain size for maximum material removal rate. Their experimental results for machining of glass with silicon carbide abrasive are shown in Fig. 1.3 which indicates that the optimum grain size under these conditions is 40  $\mu\text{m}$ . Fine grain abrasives give better surface finish and are recommended for polishing, deburring and other finishing operations. Table 1.1 gives typical applications of some commercially available abrasives.



### 1.2.3 Nozzle

The abrasive particles mixed with carrier fluid at high pressure is allowed to expand through the nozzle. During expansion the carrier fluid gains high velocity and interacts with the abrasive particles. As a result of this abrasive particles also accelerate and attain high velocity at the nozzle exit. The fluid particles, having smaller inertia compared to abrasive particles, accelerate faster. Hence, large length and small entrance angle of the nozzle enables the carrier fluid to have sufficient time to impart momentum to the abrasive particle. But, on the other hand, a larger length will have increased wall friction. This will cause further reduction in the particle velocity. Thus, there exists an optimum length of nozzle which will give maximum particle velocity for an specified entrance angle and loading ratio (the ratio of the mass flow rate of particle to the mass flow rate of air). The optimum nozzle length for parallel side nozzle of circular cross-section with 250  $\mu\text{m}$  silicon carbide particles has been found to be of the order of 20 times the nozzle diameter (Fig. 1.4). Wolak et al. [7], however, found that the optimum length to be independent on the loading ratio (Fig. 1.5).

The nozzle used in AJM has to withstand severe erosive action due to flow of air and abrasive mixture. Thus, it must be made of high wear resistant material. The common materials for nozzle are sapphire and tungsten carbide.

Depending on the requirements, the nozzle may be either straight or right angled with various sizes of round and rectangular cross-sections. The dimensions of various kinds of round and rectangular slot nozzles of different materials and their nozzle life are indicated in Table 1.2.

#### 1.2.4 Machining Variables

Ingulli [3], Bhattacharyya[4] and Pandey et al. [5 and 6] have shown that the stand-off distance has considerable effect on the material removal rate as well as the accuracy of machining in AJM. They have found that the material removal rate first increases with increase in stand-off distance and then decreases with further increase giving an optimum value (Fig. 1.6). A large stand-off distance results in the flaring up of the jet which leads to poor accuracy [3-5].

During the study of erosion of a surface by impact of solid particles Wellinger and Uetz [8], Finnie [9] and Finnie et al. [10] have revealed strong dependence of erosion rate on the angle of impingement, hardness of the target surface and velocity of impacting particles. Sheldon and Finnie [11] in their study have shown that the brittle materials give maximum volume removal rate when the impingement angle is nearly 90 degrees, while ductile materials give maximum erosion when impingement angle is between 10 to 30 degrees (Fig. 1.7).

The kinetic energy of the impinging particles of the jet, is utilized for material removal in AJM, which is a function of the particle velocity. Thus, material removal rate is dependent on the pressure of the carrier fluid at nozzle inlet, nozzle design, abrasive type, grain size and mixture ratio. Not only the flow characteristics of gas-particle flow system but the number of particles taking part into erosive cutting of abrasive jet also depends upon the mixture ratio. The mixture ratio  $\alpha$  is generally defined as the ratio of abrasive particles mass flow rate  $\dot{M}_p$  to the mass flow rate of gas (air) and abrasive particles mixture ( $\dot{M}_g + \dot{M}_p$ ). Thus,

$$\alpha = \frac{\dot{M}_p}{\dot{M}_p + \dot{M}_g} \quad (1.1)$$

At a particular pressure, material removal rate increases with increase in abrasive flow rate and is influenced by the size of the abrasive particle. After reaching an optimum value, the material removal rate decreases with further increase in abrasive flow rate [4].

#### 1.2.5 Work Material

Abrasive jet machining is recommended for machining of brittle materials such as glass, mica, ceramics and refractories. Most of the ductile materials are difficult to machine by this process. The material removal rate appears to be related to the hardness of the work material (Fig. 1.8).

#### 1.3 Impact Erosion

It is important to consider the response of target material under the action of solid particle impact before analysing any erosion process. This response may be 'ductile' or 'brittle'. In ductile materials, large plastic strain precedes fracture and material is removed by the displacement action of the impacting particle. By contrast, brittle material fractures without observable plastic deformation and material is removed by the propagation<sup>a</sup> and intersection of different systems of cracks formed

at the impact site. Although the concepts of ideally ductile and ideally brittle behaviour are over simplification, they do describe to a certain degree of approximation the behaviour of many real materials and allow analytical solutions to be developed. The mechanisms by which ductile and brittle solids erode must be understood before one can make realistic analysis for some real engineering materials having intermediate type of behaviour.

#### 1.3.1 Ductile Erosion

Various experimental and theoretical studies have been carried out to understand the process of erosion of a ductile metal. Experimental studies on fly-ash erosion by Fisher and Davis [12] have revealed that erosion loss increases with increase in both impact velocity and stand-off distance. Stoker [13] has shown that erosion rate is dependent on the impingement angle of the impacting particle.

Perhaps the first scientific approach for the study of erosion phenomenon in ductile materials under the action of a stream of solid particles has been made by Finnie [14]. The theory assumes that a hard, angular particle, impinging upon a smooth surface at an angle  $\theta$  from the work surface will cut into the surface much like a sharp tool. He solved equations of motion of cutting tip of the particle

with the assumption that the ratio  $R$ , of the vertical component to the horizontal component of the force acting on the cutting tip of the particle, remains constant through-out the impact. Depending on the impingement angle  $\theta$ , two kinds of cutting processes have been identified : (a) the particle cuts into the ductile surface, and subsequently leaves it removing the fragment of chip; and (b) the particle is stopped during its scooping action at some depth when its kinetic energy is exhausted. The limiting value of the impingement angle  $\theta_0$  distinguishing between these two situations has been expressed as

$$\theta_0 = \tan^{-1} \left( \frac{R}{6} \right) . \quad (1.2)$$

Finnie [14] has shown that the eroded volume  $V$  from the target surface by impacting particles of mass  $M_p$  and velocity  $u_{pim}$  is given by

$$V = \frac{M_p f(\theta) u_{pim}^2}{2\sigma_f} , \quad (1.3)$$

where  $\sigma_f$  is the flow stress of the target material and  $f(\theta)$  is a function of impingement angle and has been expressed as

$$f(\theta) = \frac{(\sin 2\theta - 3\sin^2\theta)}{2} ; \quad 0 < \theta \leq \theta_0 \quad (1.4)$$

and

$$f(\theta) = \left( \frac{\cos^2\theta}{6} \right) ; \quad \theta_0 \leq \theta < 90^\circ \quad (1.5)$$

This model is quite successful in explaining many features of solid particle erosion. However, quantitative discrepancies appear concerning the effect of flow stress, the velocity exponent and the applicability of the model itself for impingement angles close to 90 degrees. The theory predicts no erosion at normal impacts ( $\theta = 90^\circ$ ), while experimentally sizable erosion values are obtained. In the later work, Finnie and McFadden [15] have extended Finnie's original analysis by modifying the interaction forces between the particle and the target surface. They obtained the velocity exponents of about 2.5 which is close to the value found experimentally.

The erosion rate not only depends on the impingement angle but also on the shape of the erosive particles. The spherical particles give lower erosion rate than the angular particles of the same material. This was verified experimentally by using different sand grains [9].

The erosion resistance of various metals when impacted upon by angular silicon carbide particles of 250  $\mu\text{m}$  average size show a linear increase with Vicker's hardness on log-log representation (Fig. 1.9). It has also been observed that increase in hardness either by cold working or through heat treatment appears to be ineffective in raising erosion resistance [10].

By incorporating the idea of particle energy threshold, Bitter [16,17] has developed an expression to give a better account for erosion at various impingement angles. He has postulated two types of wear, 'deformation wear' and 'cutting wear', the former is caused by repeated deformation, while the later is due to the cutting action of free moving particles during collision. Brittle materials generally erode due to deformation wear, while ductile materials erode due to cutting wear. His approach is based on the computation of plastic energy dissipation from the impact parameters of a single erosive particle under elastic-plastic collision. He has shown that the deformation wear volume  $V_d$  can be expressed as

$$V_d = \frac{M_p (u_{pim} \sin \theta - u_{pe})^2}{2 \epsilon_d}, \quad (1.6)$$



where  $u_{pe}$  is the elastic impact velocity at which the elastic limit is just reached in the target material and the deformation wear factor  $\varepsilon_d$  is a material property defined as the amount of energy needed to remove a unit volume of material.

The cutting wear exists when particles strike a body at an acute angle scratching out some metal from the surface. The particle impact velocity  $u_{pim}$  is resolved into two components, one normal to the target surface and other parallel to it. The normal component of particle impact velocity  $u_{pimn}$  causes penetration of particle into the target surface, while tangential component of particle impact velocity  $u_{pimt}$  gives the scratching action. Similar to the earlier erosive cutting theory [14], two possibilities exist for the cutting action. If  $\theta < \theta_0$ , the incident particle leaves the surface with a non-zero velocity after cutting, but for  $\theta > \theta_0$  the particle velocity is zero as its kinetic energy is exhausted. For the first case ( $\theta < \theta_0$ ), if  $u'_{pimt}$  is the residual tangential component of the particle impact velocity, the energy absorbed in the process of scratching is  $\frac{1}{2} M_p (u_{pim}^2 \cos^2 \theta - u'^2_{pimt})$ . In the second case ( $\theta > \theta_0$ ), the energy absorbed in the process of scratching is  $\frac{1}{2} M_p u_{pim}^2 \cos^2 \theta$ . The cutting wear factor  $\varepsilon_c$ , defined as the quantity of energy needed to

scratch a unit volume of material from the target surface, depends on the mechanical properties of the target material. Bitter [17] has shown that the resulting cutting wear volume  $V_c$  can be expressed as

$$V_c = \frac{2M_p c_1 (u_{pim} \sin \theta - u_{pe})^2}{\sqrt{(u_{pim} \sin \theta)}} - [u_{pim} \cos \theta - c_1 \frac{(u_{pim} \sin \theta - u_{pe})^2 \epsilon_c}{\sqrt{(u_{pim} \sin \theta)}}];$$

$$\theta < \theta_0 \quad (1.7)$$

and

$$V_c = \frac{M_p [u_{pim}^2 \cos^2 \theta - c_2 (u_{pim} \sin \theta - u_{pe})^{3/2}]}{2 \epsilon_c};$$

$$\theta > \theta_0 \quad (1.8)$$

Here  $c_1$  and  $c_2$  are constants which depend on the physical and mechanical properties of the target and the erosive particle materials. The eroded volume  $V$  due to combination of both deformation wear as well as cutting wear can be expressed as

$$V = V_d + V_c \quad (1.9)$$

Neilson and Gilchrist [18] have simplified Bitter's model and have given a simpler form of cutting wear equation while retaining the deformation wear equation given in reference [16]. For different impingement angles they have expressed the erosion volume  $V$  as

$$V = V_d + \frac{M_p (u_{pim}^2 \cos^2 \theta - u_{pimt}^2)}{2 \epsilon_c} ; \quad \theta < \theta_o \quad (1.10)$$

and

$$V = V_d + \frac{M_p u_{pim}^2 \cos^2 \theta}{2 \epsilon_c} ; \quad \theta > \theta_o , \quad (1.11)$$

where  $V_d$  is the deformation wear volume given by equation (1.6) and  $\epsilon_c$  is the cutting wear factor [17].

Tilly [19] has proposed a two-stage mechanism of erosion recognizing explicitly that particles impacting at near normal incidence may fragment and the fragments may subsequently erode the exposed surfaces. He explained the reported decrease of erosion with decreasing particle size and introduced the concept of particle size threshold for effective erosion. The studies on particle size dependence of erosion [20-22] have further confirmed that erosion rate increases with increase in particle size beyond the threshold value and ultimately reaches a saturation point.

The saturation point, however, is different for different materials. From the consideration of deformation heat generation and its diffusion rate into the target material, Shewmon [23] has also shown that a particle size threshold exists below which no erosion occurs.

Sheldon and Kanhere [24] have examined the mechanism of single particle erosion of ductile materials and have developed a method to describe the deformation and machining actions observed using indentation theory and energy balance equation. Their results give the erosion volume  $V$  as

$$V = c_3 d_p^3 u_{pim}^3 \left( \frac{\bar{\rho}_p}{H_t} \right)^{3/2}, \quad (1.12)$$

where  $c_3$  is a constant,  $H_t$  is the Vicker's hardness value of target material,  $d_p$  is the diameter and  $\bar{\rho}_p$  is the material density of the impacting particle. They obtained the velocity exponent as 3 which is notably higher than the value of 2 obtained in earlier studies [9, 14-18]. Their value of the exponent is, however, comparable to the value published for multiple particle erosion [17,22]. Earlier studies [21] have indicated that the velocity exponent is independent of the type of material while later studies [25] have shown some dependence on attack angle  $\theta$ .

Hutchings and Winter [26,27] have studied the erosion process using large (3 mm diameter) spherical as well as, angular particles with particular emphasis on the geometry and mechanisms of material removal. The characteristic deformation pattern resulting from particle impact consisted of a depression and a lip or rim of displaced material. Further, they found evidence for a critical particle velocity above which material is displaced from the crater lip. The spherical particles cause ploughing while the angular particles cause cutting. The particle rake angle at the contact was found to be the controlling parameter for cutting [28-31].

Ives and Ruff [32] have observed that impact at low angle of impingement (around 20 degrees) deforms and displaces the material from the crater into a lip at the exit and sides, whereas normal impingement produces a more uniform lip of material around the crater with considerable plastic flow. The material removal under normal impacts occurs due to ploughing and flaking [33] followed by fatigue [34] under repeated impacts.

Follansbee et al. [35] have proposed an accumulated damage model for the low velocity erosion of ductile metals due to multiple impacts of spherical particles at normal incidence using an elasto-plastic finite element code.

Sundararajan [36] has also proposed a theoretical model for the extent of lip formation as well as the erosion loss during single particle impact. He has employed the criterion of critical plastic strain at which the deformation in target material localizes and results in lip formation. Later Sundararajan and Shewmon [37] have given a new model for erosion of metals. They have obtained the velocity exponent as 2.5 for normal impacts.

Levy [38] has observed that the microstructure of target material plays an important role in the solid particle erosion of ductile alloys. Foley and Levy [39] have reported that the erosion resistance of steel increases with increase in ductility upto a certain limit depending on the strain hardening coefficient. They have further reported that erosion rate increases markedly below the ductile brittle transition temperature because of major decrease in ductility.

The effects of increasing temperature on erosion have been investigated in more details during the last few years. Depending on the material being eroded, the temperature range, and the environment, different effects due to temperature have been reported by Young and Ruff [40]. The erosion rate has been found to increase with increase in temperature [41,42]. Firmie et al. as given in Ref.[25] have

reported increased erosion for aluminium and stainless steel at higher temperatures. This effect, however, had a complicated dependence on the impingement angle. Decrease in erosion rate with increasing temperature has been reported for certain alloys also [44].

Levy and Chik [45] have experimentally shown that erosion rate depends on the hardness of the impacting particles. They have reported an increase in erosion rate upto a Vicker's hardness of about  $700 \text{ kgf/mm}^2$  and thereafter it remains more or less constant, for both normal as well as oblique impacts.

### 1.3.2 Brittle Erosion

Because of lack of ductility, brittle materials are highly susceptible to micro-fracture or localized surface cracking during solid particle impact. Under continual multiple impacts, microfractures formed in brittle solids result in appreciable material loss by erosive wear. The formation of micro-cracks in brittle solids under such situations is a complex process and depends on the physical properties of the target and the projectile materials and the projectile velocity. Attempts to describe the erosive wear behaviour of brittle materials have tended to be semi-empirical. Several attempts have been made to use

quasi-static indentation results for evaluating the extent of damage produced during dynamic particle impact [46,48, 50,56,63]. This approach has been adopted by Sheldon and Finnie [46] to analyse the erosive wear phenomenon of brittle materials. They assumed that the interactions between the impacting particle and the target are perfectly elastic and Hertzian contact stresses are produced in the target during the course of indentation under the impact. These stresses result in the formation of Hertzian cracks which initiate from pre-existing flaws that lie just outside the area of contact between the particle and the target surface. The erosion loss or material removal takes place because of the interaction of these cracks. The load at which the crack propagation occurs is related to the distribution of surface flaws through Weibull statistics. Using momentum balance, the maximum depth of indentation  $z_m$  was obtained. The final cracked space is delineated by radius of curvature  $r_f$  which is assumed to be equal to that of the effective local radius of curvature of the indenting ball producing cracking when the ball penetrates to  $z_m$ . Through these the maximum fracture radius  $a_f$  (the fictitious contact radius of a ball of radius  $r_f$ ) can be obtained using the approximate geometrical relation

$$a_f^2 = 2 r_f z_m \quad . \quad (1.13)$$



The volume removed is taken approximately equal to the volume of the spherical cap defined by  $r_f$  (or  $a_f$ ) and  $z_m$ . Thus, the final expression of eroded volume  $V$  in terms of impacting particle radius  $r_p$ , the impact velocity  $u_{pim}$  and Weibull constants  $m$  and  $\sigma_0$  is expressed as

$$V = c_4 r_p^{n_1} u_{pim}^{n_2}, \quad (1.14)$$

where the exponent  $n_1$  for spherical particle is given by

$$n_1 = 3(m - 0.67)/(m-2),$$

and for angular particles is given by

$$n_1 = 3.6(m - 0.67)/(m-2).$$

The exponent  $n_2$  for both spherical as well as angular particles is given by

$$n_2 = 2.4(m - 0.67)/(m-2).$$

For particles much stiffer than the target, the constant  $c_4$  is given by

$$c_4 = \left[ \frac{E_t^{0.8(m+1)} \bar{p}_p^{1.2(m-0.67)}}{\sigma_0^2} \right]^{1/(m-2)}, \quad (1.15)$$

where  $E_t$  is the modulus of elasticity of the target material and  $\bar{\rho}_p$  is the density of the particle material. Theoretically predicted exponents  $n_1$  and  $n_2$  have been found to be in satisfactory agreement with the experimentally obtained values for several brittle materials such as glass, MgO, graphite etc. [46]. Sheldon [47] compared the experimental and theoretical values of  $c_4$  and again found reasonable agreement between the theory and experiment. The agreement, however, was not as good as that for the exponents  $n_1$  and  $n_2$ .

Inherently, this elastic-brittle treatment leads to the conclusion that erosive wear of brittle material depends on the fracture toughness [48] and on the size and the distribution of pre-existing flaws [46,49]. Investigations on the behaviour of brittle solids when quasi-statically loaded with small enough spherical indenters have revealed that the plastic flow does occur in brittle solids [48-53]. Oh et al. [49] have shown that transition from fully elastic crack formation to elastic-plastic indentation occurs, even in very brittle materials such as glass, when the diameter of the indenting particle decreases below a critical value  $d_{pc}$ . The morphology of fracture formed in brittle materials during impact can be divided into two classes, depending on whether the impacting particle is 'blunt' or 'sharp' [48,54].

Blunt particles, typified by spheres, result in the formation of cone shaped cracks (Hertzian cracks) which initiate from pre-existing surface flaws that lie in the tensile stress field outside the contact circle between the particle and the target surface [54,55]. The entire process of Hertzian crack formation is an elastic one that can be described by linear fracture mechanics. For quasi-static impact, Lawn and Wilshaw [48] and Frank and Lawn [56] have developed the requisite fracture mechanics equations for crack growth. Langiton and Lawn [57] have shown that the size of the flaw that initiates Hertzian cracks plays a secondary role in the crack growth.

Because Hertzian cracks initiate from pre-existing surface flaws, a minimum threshold stress (correspondingly a minimum impact velocity) is required for its formation [58,59]. The threshold stress for crack formation is governed by the diameter of the impacting particle and the critical stress intensity factor of the target material. Wiederhorn and Lawn [59] have obtained a theoretical expression showing the effect of particle velocity, particle material density and particle size on the strength degradation of brittle material such as glass when impacted by steel and tungsten carbide spheres. The critical load for crack growth is determined from the size of the critical flaw present on the target surface.

Knight et al. [60] have studied the crack systems produced due to impact of steel spheres (0.8 to 1.0 mm diameter) and tungsten carbide balls ( $\sim 0.4$  mm diameter) at different velocities on pyrex and soda-lime glass. They found that the crack systems produced due to impact of particles are similar to that obtained during static indentation. They further observed that a large number of fine splinter cracks are initiated beneath the impact site and propagate into the surface perpendicular to the maximum slip stress trajectories.

The sharp particle indentation (with cone, pyramid etc.) is characterized by a plastic flow at the contact zone which results in the formation of two types of crack systems - radial and lateral [50,54, 61-68]. The first type is a radial crack system oriented primarily perpendicular to the target surface, while the second type is a lateral crack system oriented parallel to the target surface [62]. The system of radial cracks is produced during the loading part of the impact cycle, whereas the system of lateral cracks is produced as the particle leaves the target surface [50,62]. Using elastic-plastic analysis, Lawn and Evans [69] have obtained a theoretical estimate of the force for radial crack formation. Further, they have shown that the critical force as well as the critical crack

size, for producing radial crack, depend on the hardness and the critical stress intensity factor of the target material. The threshold velocity, to produce the critical force which initiates the crack formation during sharp particle impact [66], is considerably lower than that for the blunt particle impact.

Evans et al. [63] have assumed that a sharp spherical particle penetrates into the target surface without distortion and the dynamic pressure is setup when the particle first hits the surface. This gives rise to a contact stress field. Using one-dimensional impact analogy, they obtained the expression for the size of the radial crack formed during impact in terms of velocity, density, size of the impacting particle and the critical stress intensity factor of the target material. From energy balance considerations Wiederhorn and Lawn [66] have developed a relation between the contact force, hardness of the target material and the maximum depth of penetration during impact. Further, they have also expressed the size of the radial crack formed during impact as a function of the target hardness, the critical stress intensity factor of the target material, the mass and velocity of the impacting particle. The final expression for the radial crack size obtained by Evans et al. [63] is quite different from

that obtained by Wiederhorn and Lawn [66]. However, both theories suggest that crack formation depends on critical stress intensity factor of the target material. The theory of Evans et al. [63] suggests a stronger dependence on the velocity of impacting particle.

The plastic zone beneath the contact point as well as the lateral crack depth during sharp particle indentation are proportional to the impression diameter [50]. Assuming that the depth at which lateral cracks are formed is proportional to the plastic zone depth, Evans et al. [63] have obtained the relationship between the depth of lateral crack  $z_l$ , particle size  $d_p$ , particle velocity  $u_{pim}$ , particle density  $\bar{\rho}_p$  and target hardness  $H_t$  as

$$\left(\frac{z_l}{d_p}\right)^2 \propto u_{pim} \sqrt{\frac{\bar{\rho}_p}{H_t}} \quad . \quad (1.16)$$

The radial cracks are primarily responsible for strength degradation, whereas the lateral cracks are responsible for erosive wear of brittle materials [50,62]. The erosion rate of brittle materials in elastic-plastic damage regime is sensitive to both the size distribution as well as the velocity of the impacting particles [70]. Experimental studies of Scattergood and Routbort [71] have

revealed that the velocity exponent in the erosion rate equation depends on the size of the impacting particles. The velocity exponent decreases with increase in the size of the particle. They found the velocity exponent to decrease from 3.4 to 2.6 when the particle size was increased from 23 to 270  $\mu\text{m}$ .

Tabakoff et al. [72] have revealed that the angle of impingement corresponding to maximum erosion depends not only on the target material but also on the impacting particle material. The erosion damage is more dependent on relative target - projectile properties than on the size and impingement velocity of the particle for a given target-projectile particle combination [73].

Mehrotra et al. [74] have considered three mechanisms of material removal under impacting particle : material chip-off when cone cracks form on the surface; material removal due to interaction of cone cracks on the flat surface and material removal due to chipping of exposed cone frustums as well as the underlying rough surface. The proposed erosion model was verified at four different particle velocities and good agreement between experimental and theoretical prediction was obtained.

Wiederhorn and Hockey [75] have applied a dimensional analysis of the variables that have significant effect on erosion. A multivariable linear regression analysis was used to fit the data to the dimensional analysis. They have shown that the dependence of erosion rate on hardness and critical stress intensity factor is greater than predicted by erosion theories [63,66].

#### 1.4 Present Work

The literature survey reveals that very little is known about the abrasive jet machining process. Most of the relevant papers seem to deal with the problem of impact erosion. In the present work an attempt has been made to carryout theoretical as well as experimental study of the abrasive jet machining process.

Material removal in AJM occurs due to erosion caused by the impact of high velocity abrasive particles carried in a fluid stream onto the workpiece surface. The erosion study in such situations involves the determination of number, direction and velocity of abrasive particles striking the work surface from fluid flow conditions and then the estimation of material removed from the workpiece. In the first phase of the study the mechanics of air-abrasive mixture flow through convergent-straight nozzle as well as



jet flow have been developed. From two-phase flow analysis a theoretical model has been proposed to estimate the velocity of abrasive particle in the air-abrasive jet.

During solid particle impacts lateral cracks are produced in brittle materials below the impact site as a result of residual stress field. Erosion loss in brittle materials occurs due to intersection of lateral cracks from adjacent impacts. On the basis of quasi-static indentation approach and using semi-empirical fracture mechanics relationships, the length of lateral crack and the depth at which lateral cracks are formed have been expressed in terms of impact parameters. Subsequently, in the second phase of the study, a theoretical model for material removal rate has been developed with the informations of lateral crack sizes.

In polishing, deburring and other finishing operations the weight/volume of the eroded material is of importance, while in micro-drilling and cutting operations it is the erosion depth (depth of penetration) which is more relevant. The third phase of study involves the experimental investigation of different parameters affecting the erosion volume, erosion depth and eroded cavity diameter etc. For this an experimental Abrasive Jet Machine has been designed and fabricated. The setup provides precise

control of the input parameters such as air and abrasive flow rates, nozzle pressure, mixture ratio and stand-off distance.

In AJM the nozzle, through which the air-abrasive mixture is expanding, is one of the very important components. The effectiveness and performance of the Abrasive Jet Machine depends on the geometry of the nozzle. The high velocity air-abrasive mixture flow through nozzle causes wear or erosion of the inner surface of the nozzle which results in changes in the geometry of the nozzle. Nozzle wear is therefore of interest not only from the point of view of cost but also from the point of view of characteristic performance of the unit. In the fourth phase of the study an attempt has been made to carryout experimental study of nozzle wear. The parameters that have been considered are nozzle length, nozzle diameter, entrance angle, mixture ratio and particle size.

In the last phase of the work, the theoretical as well as experimental results are discussed in detail in order to understand the mechanics involved in the process.

Table 1.1 : Typical Applications of Some Commercial  
Abrasives [After Bhattacharyya(4)]

Abrasives	Grain Sizes	Machining Operation
Aluminium Oxide ( $\text{Al}_2\text{O}_3$ )	12, 20, 50 $\mu\text{m}$	Cutting and grooving
Silicon Carbide (SiC)	25, 40 $\mu\text{m}$	Cutting and grooving
Sodium Bi-carbonate	27 $\mu\text{m}$	Light finishing operation below $50^\circ\text{C}$
Dolomite	76 $\mu\text{m}$	Etching and polishing
Glass Beads	0.635 to 1.27 mm	Light polishing and fine deburring

Table 1.2 : Dimensions and Nozzle Life for Various Types  
of Nozzles and Nozzle Materials [After Bhattacharyya(4)].

Nozzle Material	Round Shape Nozzle Diameter, mm	Rectangular Shape Slot Dimension, mm	Life of Nozzle, Hours
Tungsten Carbide (WC)	0.2 to 0.1	0.075 x 0.5 to 0.15 x 2.5	12 to 30
Sapphire	0.2 to 0.8	-	300

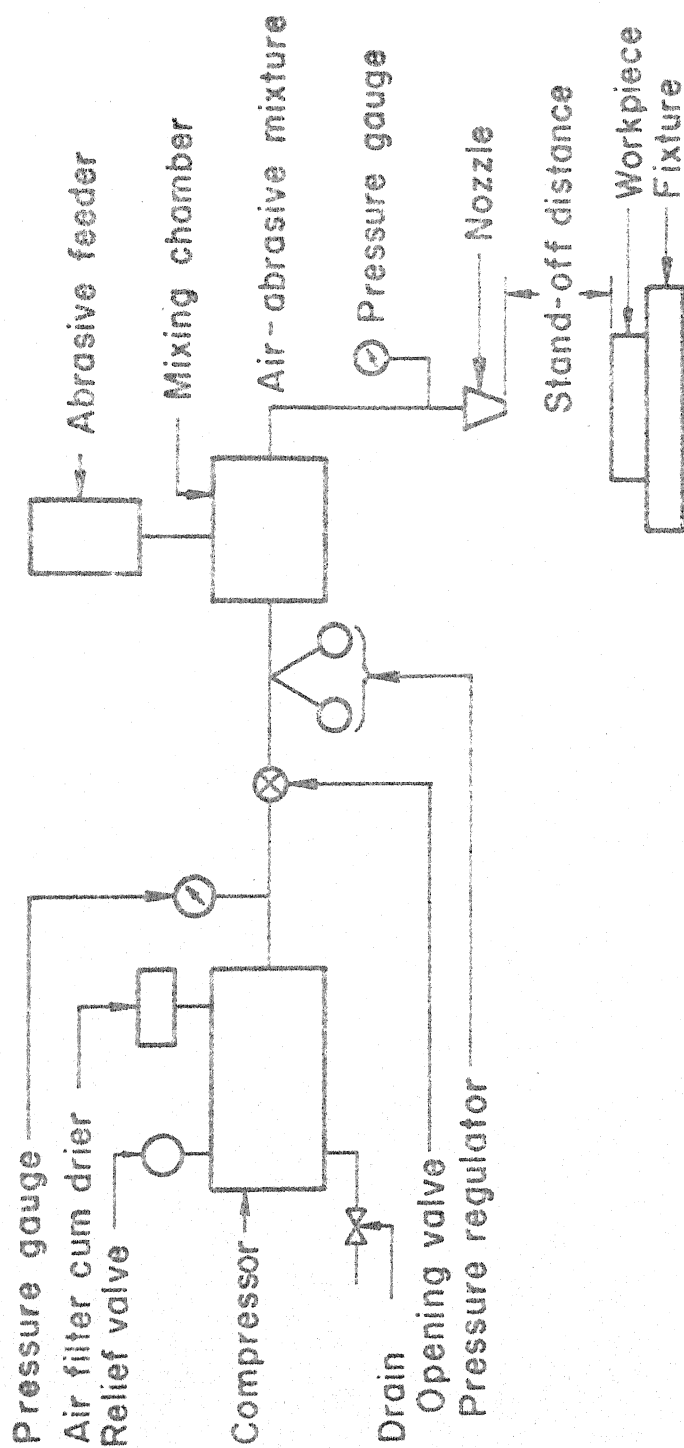


Fig. I.1 Schematic diagram of abrasive jet machining .

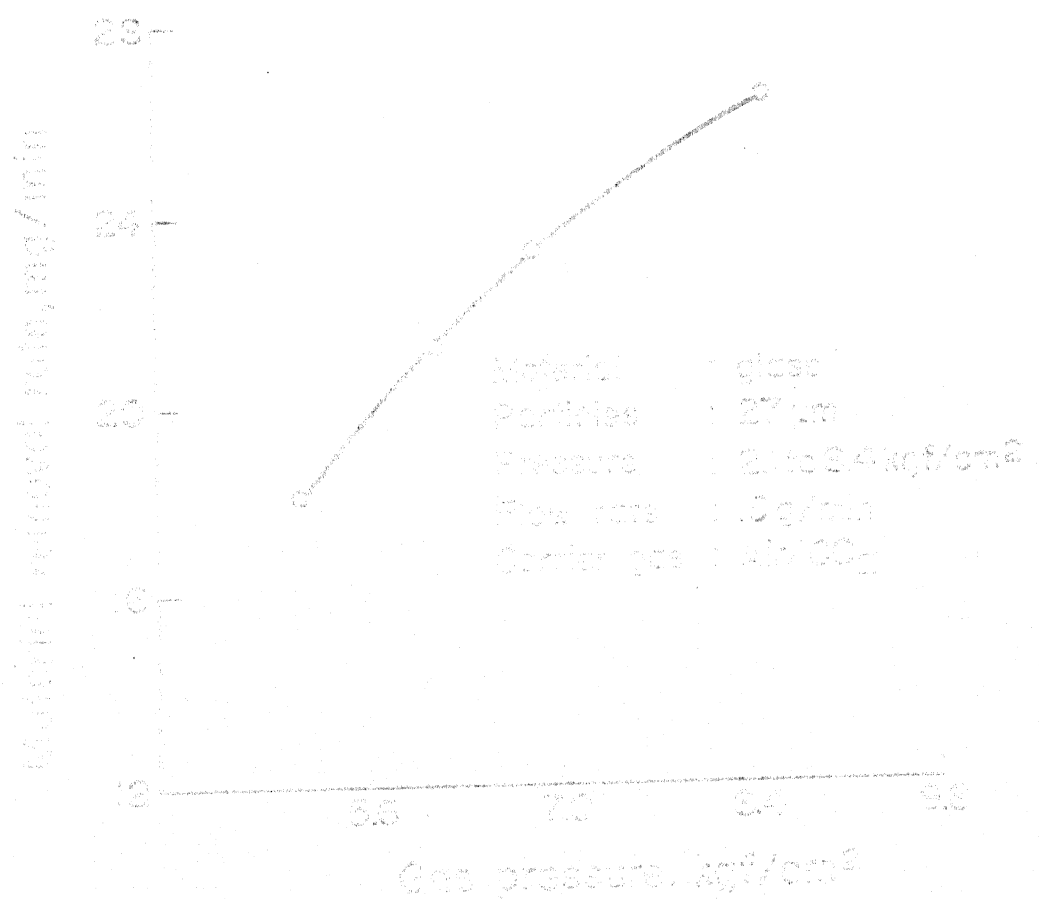


Fig.12 Effect of gas pressure on material removal rate. After Bhattacharyya (4).

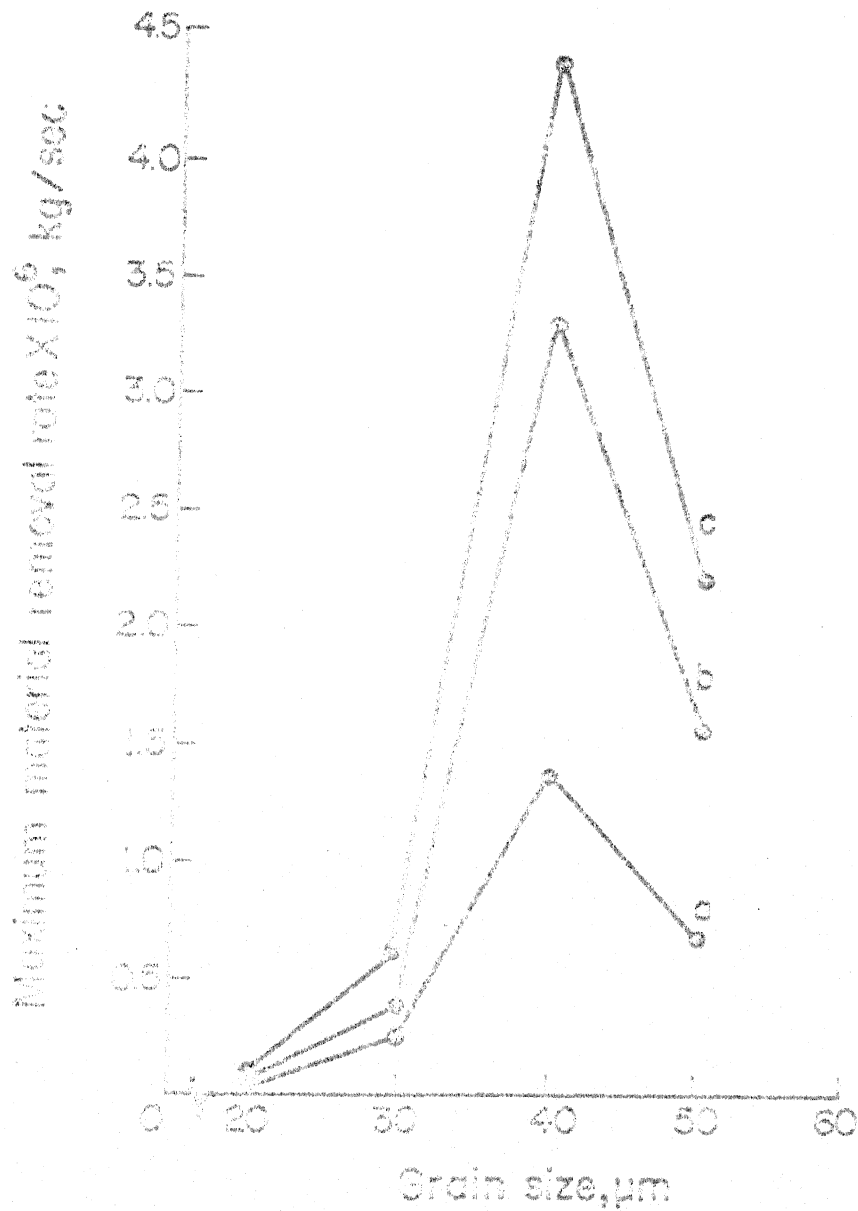


Fig.1.5 Variation of maximum material removal rate with grain size at various pressures for SiC abrasive (a)  $14.7 \times 10^6 \text{ N/m}^2$  (b)  $29.4 \times 10^6 \text{ N/m}^2$  and (c)  $39.6 \times 10^6 \text{ N/m}^2$  [After Neema and Pandey(6)].

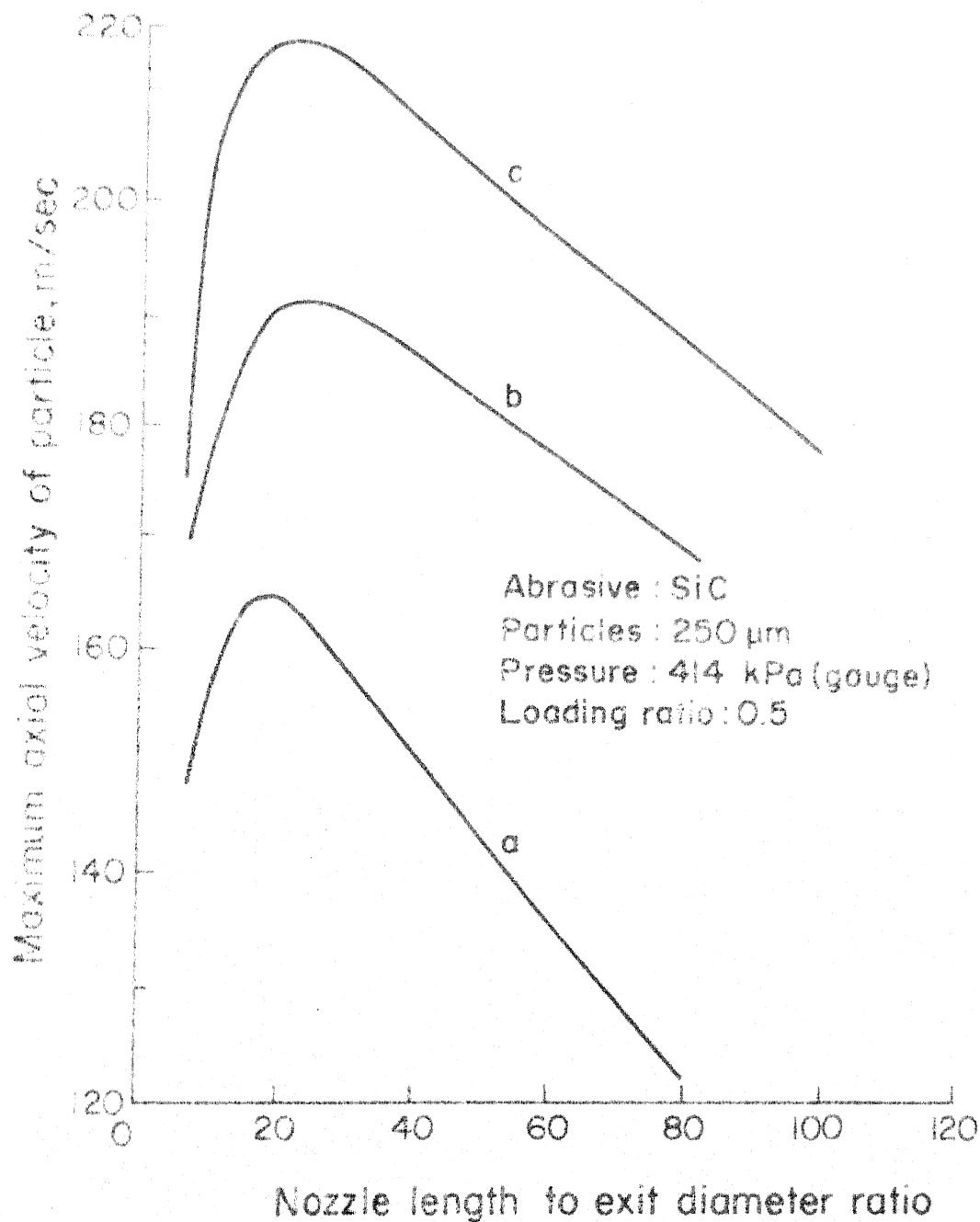


Fig. 1.4 Variation of maximum axial velocity of particle with length to diameter ratio of the nozzle for different nozzle exit diameters (a) 6 mm, (b) 9 mm and (c) 12 mm [After Wolak et al. (7)]

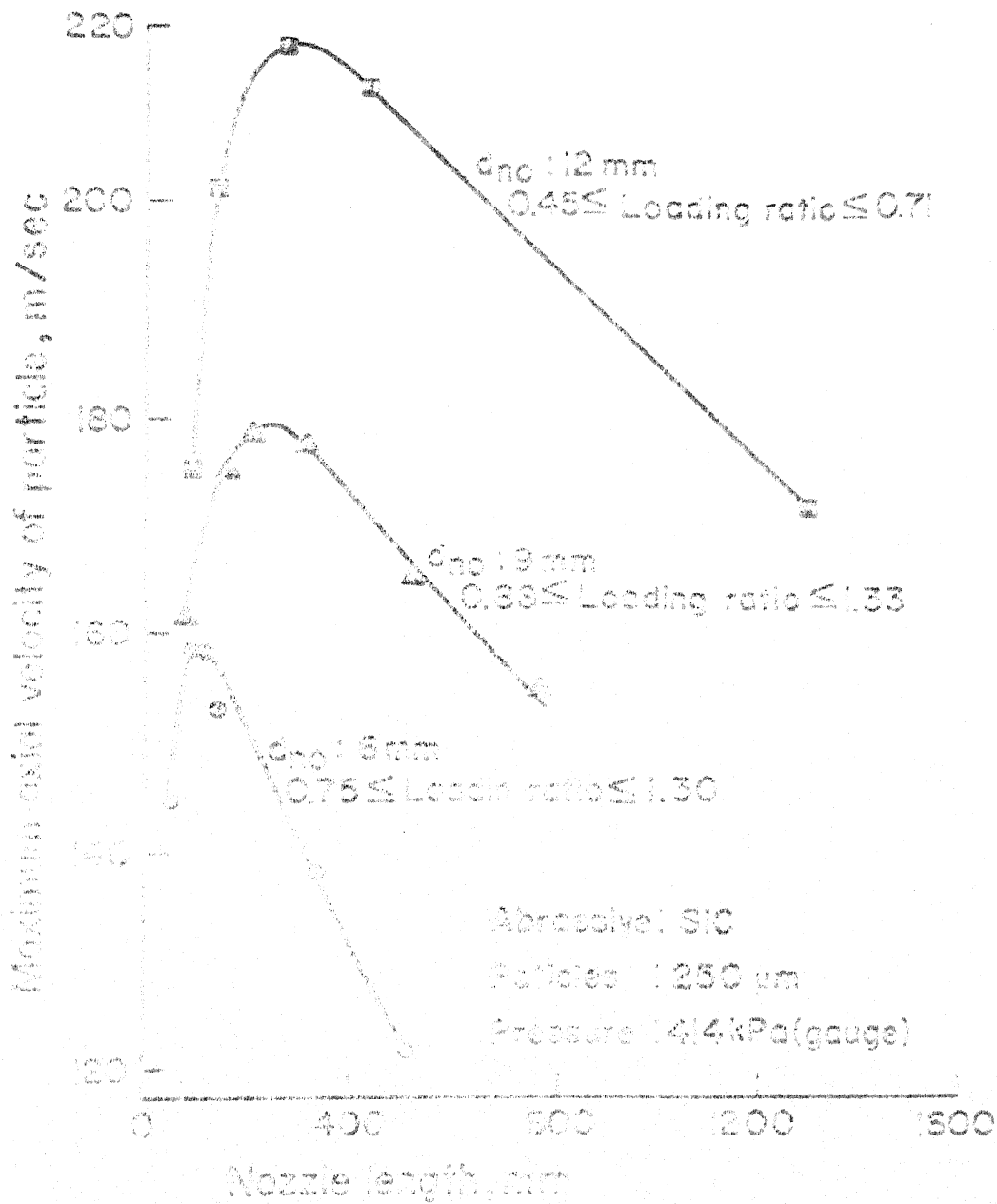


Fig. 15 Variation of maximum axial velocity of particle with the nozzle length for different nozzle diameters and loading ratios [After Wolak et al.(7)].



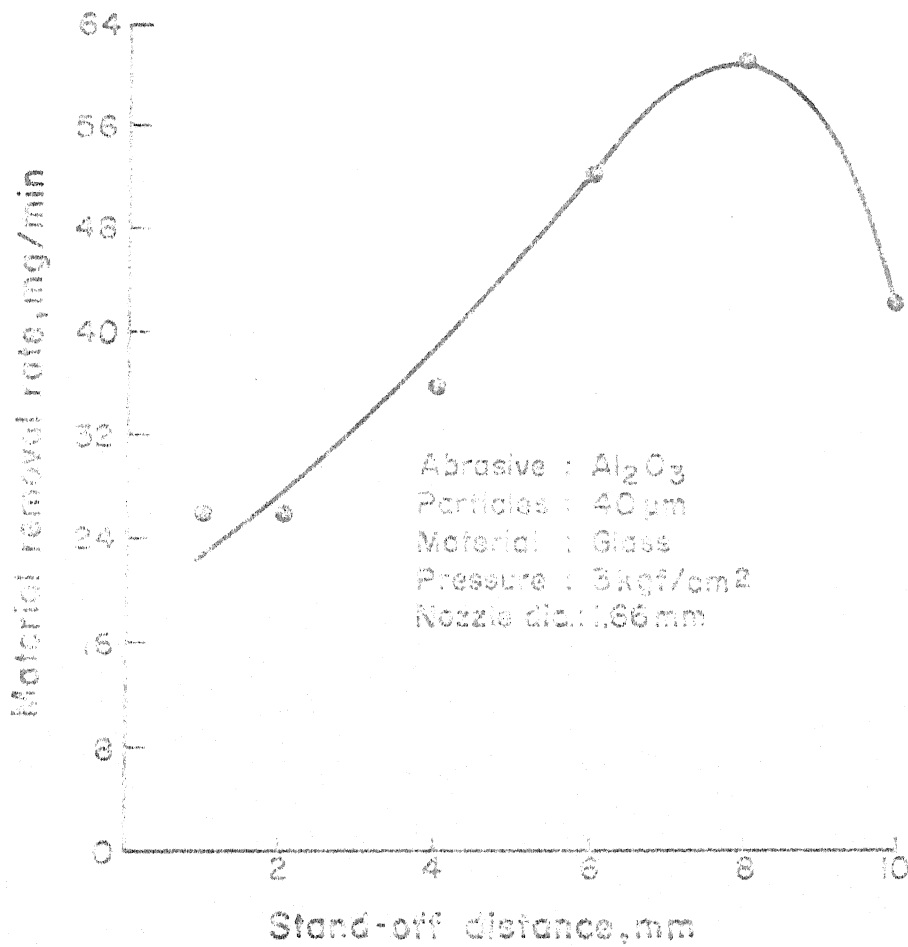


Fig. 1.6 Effect of stand-off distance on material removal rate [After Sarkar and Pandey(5)].

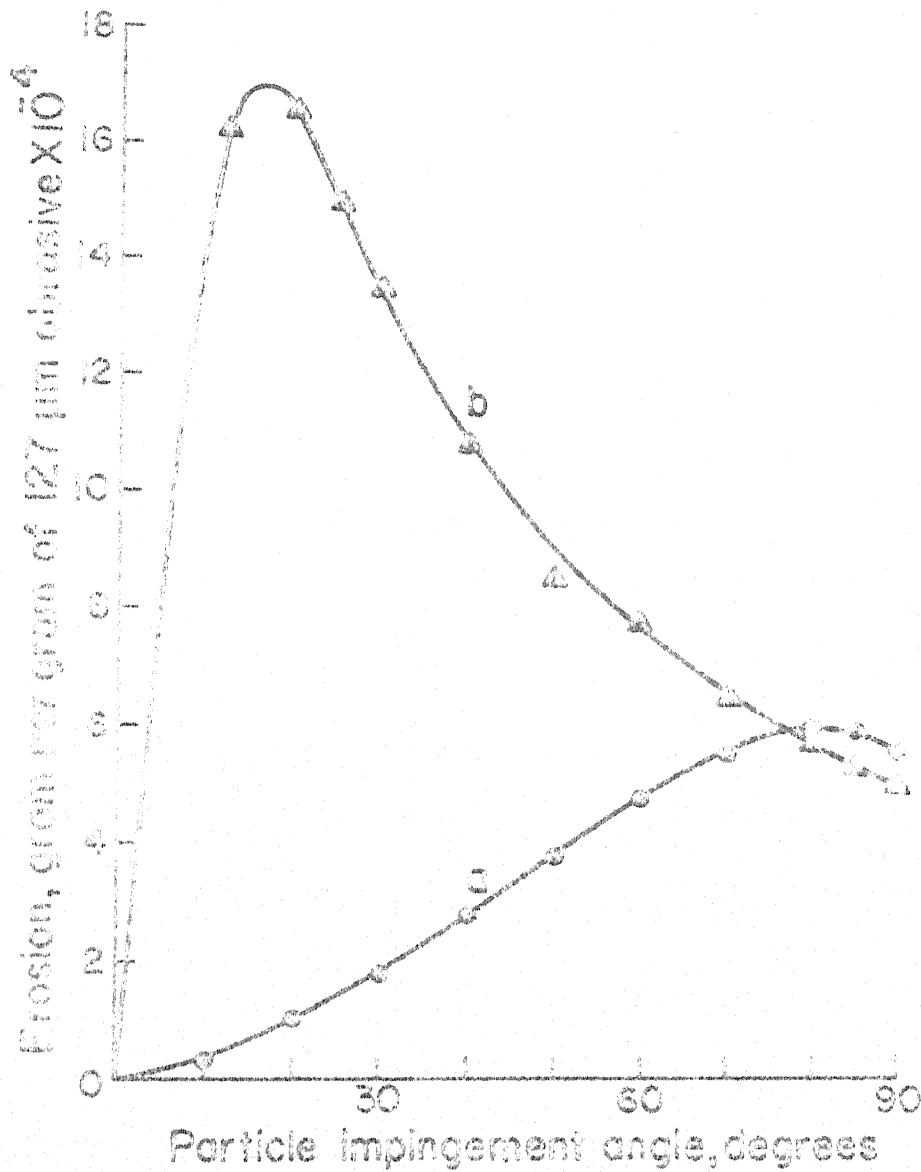
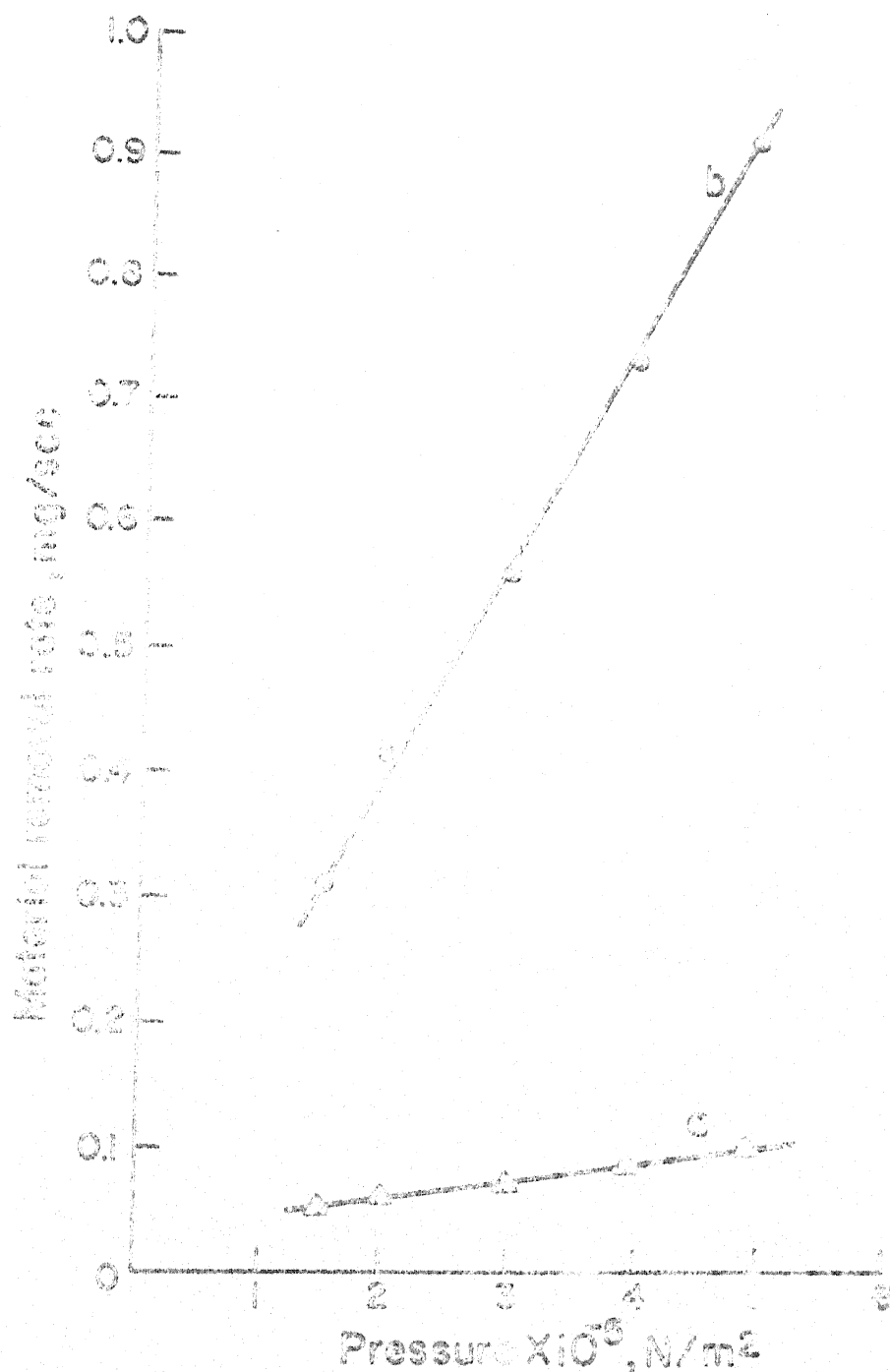


Fig. 1.7 Weight removal as a function of particle impingement angle for (a) plate glass and (b) 1100-O aluminium eroded by 120 mesh (127  $\mu$ m) grit of angular silicon carbide. Particle velocity: 500 fps [After Sheldon and Finnie (11)].



**Fig.1.8** Effect of pressure on material removal rate for different work materials (a) cemented carbide and (b) glass. Abrasive : aluminium oxide; particle size:  $40\text{ }\mu\text{m}$  [After Sorkar and Pandey(5)].

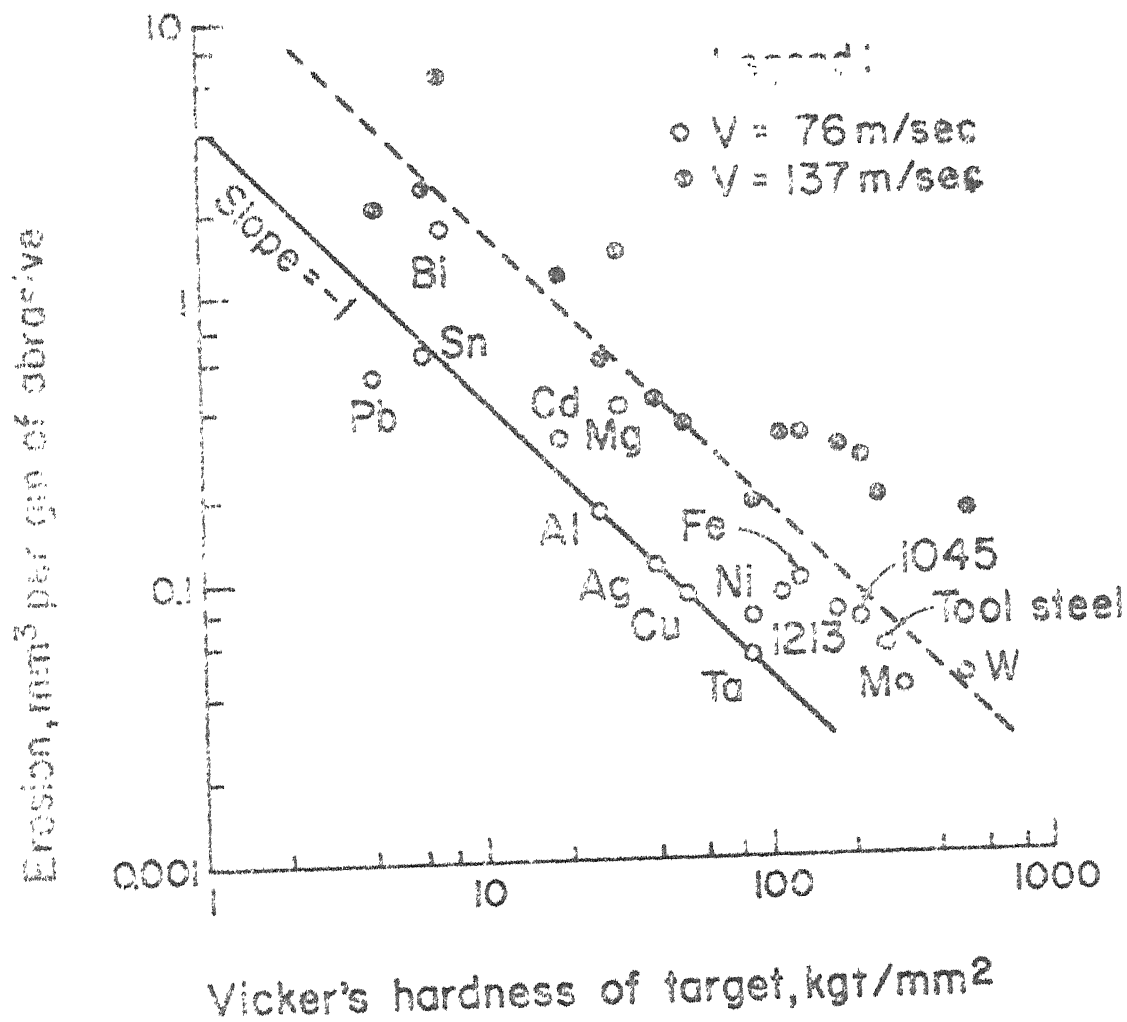


Fig. 19 Volume removal as a function of the hardness for metals eroded at  $\theta=20$  and velocities of 76 m/sec and 137 m/sec.  $d_p$ : 250  $\mu\text{m}$  SiC [After Finnie et al. (10)]

## CHAPTER 2

### THEORETICAL ANALYSIS OF ABRASIVE PARTICLE VELOCITY

#### 2.1 Introduction

For many years engineers and scientists have been interested in gas-solid particle flows which arise in many industrial applications. To mention a few gas-solid particle flow phenomena are important in sedimentation, pipe flows [76-78], fluidized beds, transport processes [79,80], propulsion and combustion [81-83], abrasive cleaning devices (sand blasting units), abrasive jet machining etc. In recent years, gas-solid particle mixture flow through rocket nozzles has received much attention [84-89].

Gas-solid particle mixture flow is a particular class of two-phase flow in which small solid particles are suspended in a gas which acts as a carrier phase. The continuum mechanics approach similar to that for single-phase flow has also been found most powerful and suitable method to deal with two-phase flow system [90]. The basic difference between single-phase flow and particulate-phase (gas-solid particle) flow lies in the mechanism of information transfer between the elements of the particulate-phase. There is no analog for pressure in a particle cloud and no information transfer exists between particles except through

the conveying phase. Momentum and energy interchange occur between two phases mainly by viscous interaction and heat transfer, other sources of interchange, like mass transfer by evaporation and condensation or chemical reactions have not been considered.

In this chapter an attempt has been made to bring out the basic characteristic features of gas-solid particle flow using certain simplifying assumptions. Various concepts for understanding gas-solid particle flow through a convergent-straight nozzle and estimation of particle velocity inside the nozzle as well as in the jet region (i.e. after exit from the nozzle) have been presented.

## 2.2 Basic Assumptions

For the treatment of particulate flow using fluid dynamical equations, the particle phase is assumed as continuum. All particles are assumed to be uniform spherical particles of identical physical properties. The particles are assumed to be sufficiently large so that Brownian motion of particle can be neglected. It will be further assumed that the particles are sparsely distributed so that flow fields around the particles are not affected by other particles. Thus, the particle cloud may be assumed to be pseudofluid and fundamental equations of motion can

also be applied for the dense phase. Also, the solid particles are assumed to be uniformly distributed at each cross-section although it is understood that they are in suspension due to turbulence and interaction exists between components of the mixture. The motion is assumed to be one-dimensional and steady and the effect of turbulence has been considered only through characteristic parameters. Mass or energy loss from the system is neglected, i.e., there is no mass exchange between the phases. The fluid phase is assumed to behave as a perfect gas and that it is inviscid except for its interaction with the particles. The body forces, viz. gravitational, electromagnetic, buoyancy etc. are neglected.

### 2.3 Aerodynamic Response Time

The density of the solid particle material is much greater than the gas density. Thus, solid particles cannot accommodate the rapid change in velocity (acceleration or deceleration) and tend to slip through the gas as they accelerate or decelerate. This particle slip velocity gives rise to a drag force acting on the carrier fluid and an equal and opposite drag force acting on the particle phase. Following the particle path and neglecting Basset force, the equation of motion for spherical solid particle of diameter  $d_p$  and material density  $\bar{\rho}_p$  in a uniform stream of gas of density  $\bar{\rho}_g$  and velocity  $u_g$  is given by [90-92]

$$\frac{\pi}{6} d_p^3 \bar{\rho}_p \frac{du_p}{dt_p} = C_d \left[ \frac{1}{2} \bar{\rho}_g (u_g - u_p)^2 A_p \right] + \frac{\pi}{6} d_p^3 \bar{\rho}_g \frac{du_g}{dt_p} + \frac{1}{2} \left[ \frac{\pi}{6} d_p^3 \bar{\rho}_g \frac{d}{dt_p} (u_g - u_p) \right] , \quad (2.1)$$

where  $A_p$  is the projected area of the solid particle perpendicular to the flow,  $C_d$  is the corrected drag coefficient,  $u_p$  is the velocity of the solid particle and  $t_p$  is the time for the motion following particle path.

The first term on the right hand side of equation (2.1) is the viscous drag term. The second term is due to pressure gradient in the fluid surrounding the particle. The third term is the force to accelerate the apparent mass of the particle relative to the fluid.

Effects of pressure gradient, apparent mass, and Basset force become important only when the density of the fluid is comparable or higher than that of the solid particles [90]. In the present case, the ratio of densities of the solid particle to that of the fluid is of the order of  $10^3$ . Thus, the terms due to pressure gradient and apparent mass are also insignificant and equation (2.1) reduces to

$$\frac{du_p}{dt_p} = \frac{3}{\pi} \left( \frac{\bar{\rho}_g}{\bar{\rho}_p} \right) \left( \frac{C_d A_p}{d_p^3} \right) (u_g - u_p)^2 . \quad (2.2)$$



The projected area  $A_p$  for spherical particle perpendicular to the direction of flow is

$$A_p = \frac{\pi}{4} d_p^2 . \quad (2.3)$$

Stokes [93] has given the drag coefficient  $C_{ds}$  for spherical particle moving in fluid as

$$C_{ds} = \frac{24}{N_{Re}} . \quad (2.4)$$

Here  $N_{Re}$ , the Reynold's number, is given by

$$N_{Re} = \frac{\bar{\rho}_g d_p (u_g - u_p)}{\bar{\mu}_g} , \quad (2.5)$$

where  $\bar{\mu}_g$  is the viscosity of the fluid phase material.

Stokes drag law holds good for  $N_{Re} \leq 1$ . For flows at higher Reynold's number, Gilbert et al. [94] has introduced a correction factor  $f_c$  in the drag equation given by Stokes [93] and expressed the corrected drag coefficient  $C_d$  as

$$C_d = f_c C_{ds} , \quad (2.6)$$

where the correction factor  $f_c$  was given as

$$f_c = (28 N_{Re}^{-0.85} + 0.48) \frac{N_{Re}}{24} . \quad (2.7)$$

Using equations (2.4), (2.5) and (2.6), the corrected drag coefficient  $C_d$  can be expressed as

$$C_d = \frac{24 \bar{\mu}_g f_c}{\bar{\rho}_g d_p (u_g - u_p)} . \quad (2.8)$$

Equation (2.2), after substitution of equation (2.3) and (2.8), becomes

$$\frac{du_p}{dt} = \frac{18 \bar{\mu}_g f_c}{d_p^2 \bar{\rho}_p} (u_g - u_p) . \quad (2.9)$$

Taking

$$B = \frac{18 \bar{\mu}_g f_c}{d_p^2 \bar{\rho}_p} , \quad (2.10)$$

which is known as the 'time constant' for momentum transfer due to drag force, equation (2.9) becomes

$$\frac{du_p}{dt} = B (u_g - u_p) . \quad (2.11)$$

Taking

$$\tau_p = \frac{1}{B} = \frac{d_p^2 \bar{\rho}_p}{18 \bar{\mu}_g f_c} , \quad (2.12)$$

equation (2.11) can be written as

$$\frac{du_p}{dt_p} + \frac{u_p}{\tau_p} = \frac{u_g}{\tau_p} . \quad (2.13)$$

For  $t_p = 0$  and  $u_p = 0$ , solution of equation (2.13) yields

$$u_p = u_g \left( 1 - e^{-\left(\frac{t_p}{\tau_p}\right)} \right) . \quad (2.14)$$

For  $t_p = \tau_p$  ,

$$u_p = u_g \frac{(e-1)}{e} . \quad (2.15)$$

This time  $\tau_p$  is defined as the particle relaxation time or aerodynamic response time. It is the time required for a particle released from rest in flowing stream to achieve 63 percent of the mean free stream velocity [90,95].  $\tau_f$  is the characteristic time of the flow system and can be expressed as

$$\tau_f = \frac{L}{U} , \quad (2.16)$$

where  $L$  is the characteristic length of the flow system and  $U$  is the characteristic velocity. Stokes number  $S_K$  is defined as the ratio of aerodynamic response time

to the characteristic time of the flow system. Thus,

$$S_K = \frac{\tau_p}{\tau_f} . \quad (2.17)$$

When Stokes number is very small, the particles have ample time to respond to property changes in the conveying phase, i.e. the particles adjust to the system very quickly and their characteristics are governed by local conditions. This state of flow is described as 'equilibrium flow'. On the other hand, when the Stokes number is very large, the particles are not able to respond to the changes in gas flow. Such a flow is generally called 'frozen flow' and the particle characteristics are governed by their initial history.

#### 2.4 Behaviour of Particulate Flow

The relative volume and mass of a component in a gas-solid particle mixture are quantified by the volume fraction and bulk density. The volume fraction is the volume of a phase per unit volume of mixture while, the bulk density is the mass of a phase in unit volume of mixture. For gas-solid particle mixture, if  $\tilde{Q}$  denotes the volume fraction of solid particles then the bulk densities of particle phase  $\rho_p$  and fluid phase  $\rho_g$  can be expressed as

$$\rho_p = \tilde{Q} \bar{\rho}_p , \quad (2.18)$$

and

$$\rho_g = (1 - \bar{Q}) \bar{\rho}_g, \quad (2.19)$$

where  $\bar{\rho}_p$  and  $\bar{\rho}_g$  are the material densities of particle and fluid phases respectively. When  $\bar{Q}$  is small,  $\rho_g \simeq \bar{\rho}_g$ .

The mixture ratio  $\alpha$  as indicated earlier is defined as the ratio of the mass flow rate of the solid particles  $\dot{M}_p$  to the mass flow rate of gas and solid particles mixture  $\dot{M}$ . Thus, mixture ratio can be expressed mathematically as

$$\alpha = \frac{\dot{M}_p}{\dot{M}}. \quad (2.20)$$

Alternatively,

$$\dot{M}_p = \alpha \dot{M}, \quad (2.21)$$

and

$$\dot{M}_g = (1 - \alpha) \dot{M}. \quad (2.22)$$

The coefficient of viscosity for the mixture of gas and solid particles is not the same as that of the gas phase alone. It is also not a constant because the density of the particle phase changes [90]. Sproull [96] has measured the viscosity of dusty gases (air and dust particles of limestone and talc) using rotating viscometer and found the viscosity of mixture to be less than that of clean air.

There appears to be some controversy about the viscosity of gas-solid particle suspension [90, 96-99]. Although there is disagreement as to whether the viscosity increases or decreases when solid particles are added to the gas, the viscosity of the mixture  $\mu_m$ , according to Einstein [See Reference (90)], can be expressed as

$$\mu_m = \bar{\mu}_g (1 + 2.5 \bar{Q}) . \quad (2.23)$$

Since,  $\bar{Q} = \frac{\rho_p}{\rho_g}$  which is of the order of  $10^{-3}$ ,  $\mu_m$  can be taken as the viscosity of the gas phase alone. Soo [90] has given

$$\mu_g \simeq \left(1 - \frac{\rho_p}{\rho_g}\right) \mu_m , \quad (2.24)$$

and

$$\mu_p \simeq \frac{\rho_p}{\rho_g} \mu_m , \quad (2.25)$$

where  $\mu_p$  is the viscosity of the particle phase and  $\mu_g$  is the viscosity of the gas phase in the mixture.

For very dilute suspension,

$$\mu_g \simeq \mu_m \simeq \bar{\mu}_g , \quad (2.26)$$

and

$$\mu_p \simeq 0 , \quad (2.27)$$

i.e., viscosity of the gas phase is approximately equal to the viscosity of gas phase material and the particle phase viscosity may be neglected.

#### 2.4.1 Equation of State

The equation of state for the gas phase is

$$P_g = R_g \rho_g T_g = R_g(1-\bar{Q}) \bar{\rho}_g T_g, \quad (2.28)$$

where  $P_g$  is the partial pressure due to gas phase,  $R_g$  is the gas constant and  $T_g$  is the temperature of gas phase. The total pressure  $P$  from the perfect gas law is

$$P = R_g \bar{\rho}_g T_g, \quad (2.29)$$

and

$$P_g = (1 - \bar{Q}) P, \quad (2.30)$$

where  $P = (P_g + P_p)$ .

Hence,

$$P_p = \bar{Q} P = \bar{Q} R_g \bar{\rho}_g T_g. \quad (2.31)$$

This indicates that when  $\bar{Q}$  is small the partial pressure  $P_p$  of the particle phase is negligible. This fact is also supported by saying that the particle phase has no analog of pressure. The equation of state for the mixture can, therefore, be expressed as

$$P = R_g \rho_g T_g . \quad (2.32)$$

#### 2.4.2 Continuity Equation

The continuity equations for the case of two-phase (gas-solid particle) flow are similar to those for a single-phase flow with the exception of source terms. These equations for uniform particle sizes are [90]

$$\frac{\partial \rho_p}{\partial t} + \frac{\partial \rho_p u_{pi}}{\partial x_i} = - \dot{w}_p ; \quad i=1,2,3 \quad (2.33)$$

for the particle phase, where  $t$  is the time,  $x_i$  is the  $i$ th component of the space coordinate,  $u_{pi}$  is the  $i$ th component of the velocity of the particle phase and

$$\frac{\partial \rho_g}{\partial t} + \frac{\partial \rho_g u_{gi}}{\partial x_i} = \dot{\Psi}_p \quad (2.34)$$

for the fluid phase. Here  $u_{gi}$  is the  $i$ th component of the velocity of fluid phase. The term  $\dot{\Psi}_p$  normally called as source function of particles, represents the mass addition to the fluid phase per unit volume of mixture caused by phenomenon such as evaporation, condensation etc. If there is no change of phase, as in the present case, the source function  $\dot{\Psi}_p = 0$ .



### 2.4.3 Limit of Continuum Approximation

When solid particles are introduced into a fluid stream there is a velocity distribution around the particle due to the relative motion. When the relative speed is high enough, the existence of wake is expected. Therefore, the concept of continuum mechanics when applied to the case of particulate suspension requires examination of the nature of fluid flow around the particles.

In the absence of shear motion, body force and chemical reaction, the equation for conservation of momentum of suspension of identical solid particles can be written as

$$\rho_g \frac{du_{gi}}{dt_g} + \rho_p \frac{du_{pi}}{dt_p} = - \frac{\partial p}{\partial x_i} , \quad (2.35)$$

where  $t_g$  and  $t_p$  are the time for the motion following fluid path and solid particle path respectively. In this equation the particle phase is treated as a true continuum, that is, not only the gas imparts its momentum to the particles but the cloud of solid particles can also transfer its momentum to the gas. This is obviously not always the case. Even in laminar flow range of relative motion, Frossling [100] have shown that the boundary layer thickness  $\delta$  for flow over a sphere can be evaluated from

$$\frac{\delta\sqrt{2}}{d_p} \sqrt{\frac{d_p \bar{\rho}_g (u_{g_i} - u_{p_i})}{\bar{\mu}_g}} \leq 3. \quad (2.36)$$

Therefore, if cloud of particles is to exert sufficient drag on the gas, the interparticle spacing must be smaller than  $(2\delta + d_p)$ .

The number density of solid particle  $n_p$  is defined as number of solid particles per unit volume of mixture. A cube of sides  $(d_p + 2\delta)$  will contain eight particles one at each corners with one eighth contribution to the considered cubical volume of mixture. Thus, the effective number of particles per unit volume of mixture is one. Hence, the number density of solid particle is

$$n_p^{1/3} \leq 2\delta + d_p \leq 2\delta. \quad (2.37)$$

This relation leads to

$$d_p n_p^{1/3} \leq \frac{\sqrt{2}}{3} \sqrt{\frac{d_p \bar{\rho}_g (u_{g_i} - u_{p_i})}{\bar{\mu}_g}}, \quad (2.38)$$

for successful transfer of momentum of mass motion between the two phases. Here the solid particles may also accelerate the fluid phase in a similar manner as gas accelerates solid

particles. When equation (2.38) is not satisfied, the fluid phase (gas) simply acts as a free stream dissipating the kinetic energy of the particles in their wakes. This physical state leads to the conclusion that outside the Stokes' law range, drag coefficient of solid particles depends on the concentration of clouds besides the Reynold's number of relative motion.

To account for all situations, Soo [90] has shown that equation (2.35) should be modified as

$$\rho_g \frac{du_{gi}}{dt_g} + K_m \rho_p \frac{du_{pi}}{dt_p} = -\frac{\partial p}{\partial x_i}, \quad (2.39)$$

with the 'effectiveness'  $K_m = 1$  for the case when solid particles are accelerated by the gas, and  $K_m < 1$  for the case when solid particles are decelerated by the gas.

For a dense cloud of solid particles, when negligible dissipation in wake is encountered,  $K_m = 1$ . For a lean suspension, dissipation in wakes without increase in kinetic energy of mass motion of the gas gives  $K_m \simeq 0$ . Effectiveness  $K_m$  also depends on the concentration of the suspension.

The exact representation of  $K_m$  was idealized using a discontinuous representation as shown in Fig. 2.1, although a smooth transition (dotted line) is expected [90]. It is further noted that the momentum transfer in particulate phase depends not only on the drag coefficient but also on the effectiveness  $K_m$  which in fact depends on the concentration of the suspension. Therefore, the time constant of momentum transfer  $B$  depends on the concentration of the suspension in addition to the dependence of drag coefficient. With this understanding of the continuum approximation, the basic equation of motion for two-phase flow system can be modified using  $K_m$  for the particulate phase. This modification accounts for the fact that slowing down of solid particles does not necessarily give rise to increase in static pressure of the gas.

#### 2.4.4 Equation of Motion

Pai [101] has shown that under continuum conditions, particles in pseudofluid assume stress-strain relationship similar to that of a gas. The body forces in gas-solid particle flow may arise because of gravitational forces, electromagnetic forces etc. The overall momentum equation and the particle phase momentum equation as expressed by Soo [90] are

$$\rho_g \frac{du_{gi}}{dt_g} + K_m \rho_p \frac{du_{pi}}{dt_p} = - \frac{\partial P}{\partial x_i} + \rho_g f_{bgi} + \frac{\partial}{\partial x_j} [\mu_g (\Delta_g)_{ji} + \mu_{g_2} D_g \delta_{ji}] \quad (2.40)$$

and

$$\rho_p \frac{du_{pi}}{dt_p} = \rho_p B(u_{gi} - u_{pi}) + \rho_p f_{bpi} + \frac{\partial}{\partial x_j} [\mu_p (\Delta_p)_{ji} + \mu_{p_2} D_p \delta_{ji}], \quad (2.41)$$

where  $f_{bgi}$  is the  $i$ th component of the body force per unit mass of the fluid material,  $f_{bpi}$  is the  $i$ th component of the external force acting on spherical particle per unit mass of particle material in general fluid field besides the drag force and  $P$  is the total static pressure in the fluid. The terms  $\mu_{g_2}$  and  $\mu_{p_2}$  represent the viscosity of the fluid and particle phases respectively including the bulk viscosity of the respective phases i.e.,

$$\mu_{g_2} = \zeta_g - \frac{2}{3} \mu_g ,$$

$$\mu_{p_2} = \zeta_p - \frac{2}{3} \mu_p ,$$

where  $\zeta_g$  and  $\zeta_p$  are the bulk viscosity of fluid and particle phases respectively. In equation (2.40),

$$\frac{d}{dt}_g = \frac{\partial}{\partial t} + u_{gj} \frac{\partial}{\partial x_j} ,$$

$$\frac{d}{dt}_p = \frac{\partial}{\partial t} + u_{pj} \frac{\partial}{\partial x_j} ,$$

and the deformation tensor  $(\Delta_g)_{ji}$  and dilation  $D_g$  for the fluid phase are

$$(\Delta_g)_{ji} = \frac{\partial u_{gi}}{\partial x_j} + \frac{\partial u_{gj}}{\partial x_i} ,$$

$$D_g = \frac{1}{2} (\Delta_g)_{kk} = \frac{\partial u_{gk}}{\partial x_k} .$$

In equation (2.41), the deformation tensor  $(\Delta_p)_{ji}$  and dilation  $D_p$  for the particle phase are

$$(\Delta_p)_{ji} = \frac{\partial u_{pi}}{\partial x_j} + \frac{\partial u_{pj}}{\partial x_i} ,$$

$$D_p = \frac{1}{2} (\Delta_p)_{kk} = \frac{\partial u_{pk}}{\partial x_k} .$$

Here  $i, j, k = 1, 2, 3$  ; Kronecker delta  $\delta_{ji} = 0$  for  $i \neq j$  and  $\delta_{ji} = 1$  for  $i = j$ .

#### 2.4.5 Energy Equation

The energy equation of a two-phase (gas-solid particle) flow system includes the relationship of exchange of energy between the fluid phase and the particle phase. For particulate flow, that is for both the fluid and the particle phases, the overall energy equation for mixture can be written as [90]

$$\begin{aligned}
 \rho_g \frac{d}{dt} \left( \frac{u_{gi}^2}{2} + c_{pg} T_g \right) + \rho_p \frac{d}{dt} \left( \frac{u_{pi}^2}{2} + c_{pp} T_p \right) &= \frac{\partial P}{\partial t} \\
 + \frac{\partial}{\partial x_j} k_g \frac{\partial T_g}{\partial x_j} + \frac{\partial}{\partial x_j} k_p \frac{\partial T_p}{\partial x_j} + \frac{\partial}{\partial x_j} u_{gj} [\mu_g (\Delta_g)_{ji} \\
 + \mu_{g2} D_g \delta_{ji}] + \frac{\partial}{\partial x_j} u_{pj} [\mu_p (\Delta_p)_{ji} + \mu_{p2} D_p \delta_{ji}] \\
 + \Gamma_g + \Gamma_p, \quad (2.42)
 \end{aligned}$$

where  $c_p$ ,  $T$  and  $k$  are the specific heat, temperature and thermal conductivity. Suffix  $g$  represents the fluid phase while  $p$  represents the particle phase. The term  $\Gamma_g$  includes the heat source and the radiations per unit volume of the mixture and  $\Gamma_p$  includes the heating of particles due to viscous dissipation.

## 2.5 Particle Velocity in the Nozzle

In the present analysis, under the assumptions made in Sec. 2.2, one-dimensional steady state frictionless adiabatic flow through convergent-straight nozzle with dilute concentration of solid particles has been considered. With the introduction of mixture ratio  $\alpha$ , the continuity relation (Sec. 2.4) gives the flow rate of gas phase as

$$\rho_g u_g A_n = (1 - \alpha) \dot{M} = \text{Constant} , \quad (2.43)$$

and the flow rate of particle phase as

$$\rho_p u_p A_n = \alpha \dot{M} = \text{Constant} , \quad (2.44)$$

where  $A_n$  is the cross-sectional area of the flow passage of the nozzle.

For steady state frictionless, adiabatic flow the terms  $\frac{\partial}{\partial x_j} k_g \frac{\partial T_g}{\partial x_j}$ ,  $\frac{\partial}{\partial x_j} k_p \frac{\partial T_p}{\partial x_j}$  and  $\frac{\partial P}{\partial t}$  of equation (2.42) become zero. For inviscid fluid phase, neglecting heat losses (heat transfer due to convection, radiation through wall, heat transfer between particle and wall due to impact and heating of particles due to viscous dissipation) the overall energy equation of the mixture for the gas-solid particle flow through the nozzle reduces to



$$\rho_g u_g \frac{d}{dx} \left( c_{pg} T_g + \frac{u_g^2}{2} \right) + \rho_p u_p \frac{d}{dx} \left( c_{pp} T_p + \frac{u_p^2}{2} \right) = 0 . \quad (2.45)$$

Differentiating with respect to  $x$ , and using equations (2.43) and (2.44), equation (2.45) becomes

$$u_g \frac{du_g}{dx} + c_{pg} \frac{dT_g}{dx} + \left( \frac{\alpha}{1-\alpha} \right) \left[ u_p \frac{du_p}{dx} + c_{pp} \frac{dT_p}{dx} \right] = 0 . \quad (2.46)$$

For steady state, inviscid, non-reactive and uncharged gas-solid particle flow equations (2.40) and (2.41) become

$$\rho_g u_g \frac{du_g}{dx} + K_m \rho_p u_p \frac{du_p}{dx} = - \frac{dP}{dx} \quad (2.47)$$

and

$$u_p \frac{du_p}{dx} = B (u_g - u_p) . \quad (2.48)$$

Equations (2.43) and (2.44) are the continuity equations, equation (2.46) represents the energy equation, equations (2.47) and (2.48) represent the momentum equation, for the gas-solid particle mixture flow through the nozzle.

Rearranging, equation (2.46) yields

$$\frac{dT_g}{dx} = - \left( \frac{u_g}{c_{pg}} \right) \frac{du_g}{dx} - \frac{\alpha}{1-\alpha} \left[ \left( \frac{u_p}{c_{pg}} \right) \frac{du_p}{dx} + \left( \frac{c_{pp}}{c_{pg}} \right) \frac{dT_p}{dx} \right] . \quad (2.49)$$

Substitution for  $\rho_g$  from equation (2.43) into equation (2.32) yields

$$P = \frac{(1-\alpha)}{u_g A_n} \dot{M} R_g T_g . \quad (2.50)$$

Differentiation of equation (2.50) with respect to  $x$  gives

$$\frac{dP}{dx} = (1-\alpha) \dot{M} R_g \left[ \left( \frac{1}{u_g A_n} \right) \frac{dT_g}{dx} - \left( \frac{T_g}{A_n u_g^2} \right) \frac{du_g}{dx} - \left( \frac{T_g}{A_n^2 u_g} \right) \frac{dA_n}{dx} \right] . \quad (2.51)$$

Substitution of equation (2.43) into equation (2.51) and after simplification yields

$$\frac{dP}{dx} = \rho_g R_g \left[ \frac{dT_g}{dx} - \left( \frac{T_g}{u_g} \right) \frac{du_g}{dx} - \left( \frac{T_g}{A_n} \right) \frac{dA_n}{dx} \right] . \quad (2.52)$$

Using equations (2.43) and (2.44), equation (2.47) can be written as

$$\frac{dP}{dx} = - \rho_g u_g \left[ \frac{du_g}{dx} + K_m \left( \frac{\alpha}{1-\alpha} \right) \frac{du_p}{dx} \right] . \quad (2.53)$$

Solution of equations (2.52) and (2.53) gives

$$\frac{dT_g}{dx} = \left( \frac{T_g}{u_g} \right) \frac{du_g}{dx} + \left( \frac{T_g}{A_n} \right) \frac{dA_n}{dx} - \left( \frac{u_g}{R_g} \right) \frac{du_g}{dx} - K_m \left( \frac{\alpha}{1-\alpha} \right) \frac{u_g}{R_g} \frac{du_p}{dx} . \quad (2.54)$$

Elimination of  $\frac{dT_g}{dx}$  from equations (2.49) and (2.54) and substituting for  $R_g = \frac{P}{\rho_g T_g}$  gives

$$\frac{du_g}{dx} = \frac{\left[ \left( \frac{\alpha}{1-\alpha} \right) \left\{ \left( \frac{u_g \rho_g T_g K_m}{P} - \frac{u_p}{c_{pg}} \right) \frac{du_p}{dx} - \left( \frac{c_{pp}}{c_{pg}} \right) \frac{dT_p}{dx} \right\} - \left( \frac{T_g}{A_n} \right) \frac{dA_n}{dx} \right]}{\left( \frac{T_g}{u_g} + \frac{u_g}{c_{pg}} - \frac{u_g \rho_g T_g}{P} \right)} \quad (2.55)$$

Rearranging, equation (2.48) gives

$$\frac{du_p}{dx} = B \left( \frac{u_g}{u_p} - 1 \right) . \quad (2.56)$$

### 2.5.1 Equation of Heat Transfer for Flow Over Spherical Particle

Gebhart [102] has given an empirical equation for the Nusselt number  $N_{Nu}$  correlating data for Reynold's number  $N_{Re}$  upto 70,000 and Prandtl number  $N_{Pr}$  upto 400 for the case of

heat convection from the surface of a spherical particle immersed in a fluid stream. This equation is

$$N_{Nu} = 2 + 0.6 N_{Re}^{0.5} N_{Pr}^{1/3} . \quad (2.57)$$

From the definition of the Nusselt number [102] equation (2.57) can be rearranged as

$$h = \frac{k_g N_{Nu}}{d_p} = \frac{(2 + 0.6 N_{Re}^{0.5} N_{Pr}^{1/3}) k_g}{d_p} , \quad (2.58)$$

where  $h$  is the coefficient of heat transfer between the particles and the gas and  $k_g$  is the thermal conductivity of the gas phase.

The heat exchange between particle and gas during time  $dt$  is given by

$$h A_{sp} (T_p - T_g) dt = m_p c_{pp} (-dT_p) , \quad (2.59)$$

where  $dt$  is the time taken by the particle to travel a distance  $ds$  and  $A_{sp}$  is the surface area of the particle. Thus, particle velocity  $u_p$  is

$$\frac{ds}{dt} = u_p . \quad (2.60)$$

Mass  $m_p$  and surface area  $A_{sp}$  of the particle are

$$m_p = \frac{\pi}{6} d_p^3 \bar{\rho}_p \quad (2.61)$$

and

$$A_{sp} = \pi d_p^2 \quad (2.62)$$

Dividing equation (2.59) by  $ds$  and substituting for  $h$ ,  $\frac{ds}{dt}$ ,  $m_p$  and  $A_{sp}$  from equations (2.58), (2.60), (2.61) and (2.62) gives

$$\frac{dT_p}{dx} = \frac{6 k_g}{\bar{\rho}_p d_p^2 c_{pp}} \left( \frac{T_g - T_p}{u_p} \right) (2 + 0.6 N_{Re}^{0.5} N_{Pr}^{1/3}) \quad (2.63)$$

### 2.5.2 Dimensionless Variables

It is more convenient to use the gas-solid particle flow governing equations in dimensionless form. The common method of non-dimensionalizing the nozzle flow governing equations in terms of Mach number is not suitable for gas-solid flows. For a two-phase (gas-solid particle) system this technique may give misleading results because the simple relationship for the velocity of sound in clean gas is no longer valid for a gas-solid suspension. Although the basic equations

may still be non-dimensionalized in terms of the gas phase Mach number, care must be exercised in interpreting the results. It may be mentioned that the Mach number will be incorrect except for very low mixture ratio. To account for general situations of dense as well as dilute suspension the different variables of the flow governing equations are non-dimensionalized below with respect to the inlet flow parameters of the gas phase and the outlet diameter  $d_{no}$  of the nozzle. The dimensionless variables are indicated with superscript \* .

$$\left. \begin{aligned} u_g^* &= \frac{u_g}{u_{g1}}, & u_p^* &= \frac{u_p}{u_{g1}}, & \rho_g^* &= \frac{\rho_g}{\rho_{g1}}, \\ T_g^* &= \frac{T_g}{T_{g1}}, & T_p^* &= \frac{T_p}{T_{g1}}, & \rho_p^* &= \frac{\rho_p}{\rho_{g1}}, \\ P^* &= \frac{P}{P_1}, & A_n^* &= \frac{A_n}{A_{n1}}, & x^* &= \frac{x}{d_{no}}, \end{aligned} \right\} \quad (2.64)$$

where  $A_{n1}$  is the area of nozzle cross-section at the inlet  $u_{g1}$ ,  $\rho_{g1}$ ,  $T_{g1}$ ,  $P_1$  are the velocity, density, temperature and pressure respectively of the gas phase at nozzle inlet.

Substitution for  $\dot{M}$  from equation (2.21) into equation (2.50) gives

$$P = \frac{(1-\alpha) \dot{M}_p R_g T_g}{\alpha u_g A_n} . \quad (2.65)$$

Reducing equation (2.65) to inlet condition gives

$$u_{g1} = \frac{(1-\alpha) \dot{M}_p R_g T_{g1}}{\alpha P_1 A_{n1}} . \quad (2.66)$$

Using equation (2.43) for inlet condition, and substituting for  $\dot{M}$  from equation (2.21), gives

$$\rho_{g1} = \frac{(1 - \alpha) \dot{M}_p}{\alpha u_{g1} A_{n1}} . \quad (2.67)$$

### 2.5.3 Flow Governing Equations in Dimensionless Form for the Gas-Solid Particle Flow Through Nozzle

Using equation (2.43) together with equation (2.64), the gas phase continuity equation in dimensionless form can be expressed as

$$\rho_g^* u_g^* A_n^* = 1 . \quad (2.68)$$

Through equations (2.44) and (2.64) the continuity equation for the particle-phase in dimensionless form can be written as

$$\rho_p^* u_p^* A_n^* = \frac{\alpha}{(1-\alpha)} . \quad (2.69)$$

Similarly, equations (2.32), (2.49) and (2.52) in dimensionless form become

$$P^* = \rho_g^* T_g^* \quad , \quad (2.70)$$

$$\frac{dT_g^*}{dx^*} = - \left( \frac{u_{g1}^2}{c_{pg} T_{g1}} \right) \left[ \left( \frac{\alpha}{1-\alpha} \right) u_p^* \frac{du_p^*}{dx^*} + u_g^* \frac{du_g^*}{dx^*} \right] - \left( \frac{\alpha}{1-\alpha} \right) \frac{c_{pp}}{c_{pg}} \frac{dT_p^*}{dx^*} \quad , \quad (2.71)$$

and

$$\frac{dP^*}{dx^*} = \rho_g^* \left[ \frac{dT_g^*}{dx^*} - \left( \frac{T_g^*}{u_g^*} \right) \frac{du_g^*}{dx^*} - \left( \frac{T_g^*}{A_n^*} \right) \frac{dA_n^*}{dx^*} \right] \quad . \quad (2.72)$$

Substitution of  $\rho_g^*$  from equation (2.68) into equation (2.72) gives

$$\frac{dP^*}{dx^*} = \frac{1}{u_g^* A_n^*} \left[ \frac{dT_g^*}{dx^*} - \left( \frac{T_g^*}{u_g^*} \right) \frac{du_g^*}{dx^*} - \left( \frac{T_g^*}{A_n^*} \right) \frac{dA_n^*}{dx^*} \right] \quad . \quad (2.73)$$

Equation (2.55) rewritten in the dimensionless form and substitution of equation (2.70) yields

$$\frac{du_g^*}{dx^*} = \frac{\left[ \left( \frac{\alpha}{1-\alpha} \right) \left\{ \left( \frac{u_{g1}^2 \rho_{g1}}{P_1} \right) K_m u_g^* - \left( \frac{u_{g1}^2}{c_{pg} T_{g1}} \right) u_p^* \right\} \frac{du_p^*}{dx^*} - \left( \frac{c_{pp}}{c_{pg}} \right) \frac{dT_p^*}{dx^*} \right] - \left( \frac{T_g^*}{A_n^*} \right) \frac{dA_n^*}{dx^*}}{\left[ \frac{T_g^*}{u_g^*} + u_g^* \left( \frac{u_{g1}^2}{c_{pg} T_{g1}} - \frac{u_{g1}^2 \rho_{g1}}{P_1} \right) \right]} \quad (2.74)$$



Dimensionless form of equation (2.48) becomes

$$\frac{du_p^*}{dx^*} = B_1^* \left( \frac{u_g^*}{u_p^*} - 1 \right) \quad (2.75)$$

Here  $B_1^*$  is a dimensionless constant given as

$$B_1^* = \frac{3}{4} \frac{\bar{\mu}_g d_{no}}{d_p^2 \bar{\rho}_p u_{gl}} \cdot N_{Re} (28 N_{Re}^{-0.85} + 0.48) \quad (2.76)$$

Substitution of dimensionless variables from equation (2.64) into equation (2.5) and using equation (2.68), the particle Reynold's number  $N_{Re}$  can be expressed as

$$N_{Re} = \left( \frac{u_{gl} \bar{\rho}_{gl} d_p}{\bar{\mu}_g} \right) \left( 1 - \frac{u_p^*}{u_g^*} \right) \frac{1}{A_n^*} \quad (2.77)$$

The dimensionless forms of the cross-sectional area  $A_n^*$  of the nozzle passage and its derivative  $\frac{dA_n^*}{dx^*}$  for the considered geometry of the nozzle may be expressed as

$$A_n^* = \left( 1 - \frac{2x^* \tan \beta_1}{d_{n1}^*} \right)^2 \quad \text{for } x^* \leq l_1^*,$$

$$A_n^* = \left[ \left( 1 - \frac{d_{n2}^*}{d_{n1}^*} \right) \frac{\tan \beta_2}{\tan \beta_1} + \left( \frac{d_{n2}^*}{d_{n1}^*} \right) - \frac{2x^* \tan \beta_2}{d_{n1}^*} \right]^2$$

$$\text{for } l_1^* < x^* \leq l_2^*,$$

$$A_n^* = \left(\frac{1}{d_{n1}^*}\right)^2 \quad \text{for } x^* > l_2^* , \quad (2.78)$$

$$\frac{dA_n^*}{dx^*} = -\frac{4\tan\beta_1}{d_{n1}^*} \left(1 - \frac{2x^*\tan\beta_1}{d_{n1}^*}\right) \quad \text{for } x^* \leq l_1^* ,$$

$$\frac{dA_n^*}{dx^*} = -\frac{4\tan\beta_2}{d_{n1}^*} \left[ \left(1 - \frac{d_{n2}^*}{d_{n1}^*}\right) \frac{\tan\beta_2}{\tan\beta_1} + \left(\frac{d_{n2}^*}{d_{n1}^*}\right) - \frac{2x^*\tan\beta_2}{d_{n1}^*} \right]$$

$$\text{for } l_1^* < x^* \leq l_2^* ,$$

$$\frac{dA_n^*}{dx^*} = 0 \quad \text{for } x^* > l_2^* , \quad (2.79)$$

where

$$l_1^* = \frac{(d_{n1}^* - d_{n2}^*)}{2\tan\beta_1} , \quad (2.80)$$

$$l_2^* = \frac{d_{n1}^*}{2\tan\beta_1} + \frac{(\tan\beta_1 - \tan\beta_2)}{\tan\beta_1 \tan\beta_2} \left(\frac{d_{n2}^*}{2}\right) - \frac{1}{2\tan\beta_2} , \quad (2.81)$$

$$d_{n1}^* = \frac{d_{n1}}{d_{no}} , \quad (2.82)$$

$$d_{n2}^* = \frac{d_{n2}}{d_{no}} \quad (2.83)$$

as derived in Appendix I. Here  $d_{n1}$  is the inlet diameter,  $d_{n2}$  is the diameter at the end of first convergent region,

$d_{n1}^*$  is the dimensionless inlet diameter and  $d_{n2}^*$  is the dimensionless diameter at the end of first convergent region of the nozzle. The terms  $l_1^*$  and  $l_2^*$  represent the dimensionless distances at the ends of first and second convergent regions measured from the nozzle inlet. The terms  $\beta_1$  and  $\beta_2$  are the semi-entrance angles of the first and second convergent regions of the nozzle.

Equation (2.63) rewritten in dimensionless form becomes

$$\frac{dT_p^*}{dx^*} = \frac{6 k_g d_{no}}{\bar{p}_p d_p^2 c_{pp} u_{gl}} \cdot \left( \frac{T_g^* - T_p^*}{u_p^*} \right) (2 + 0.6 N_{Re}^{0.5} N_{Pr}^{1/3}). \quad (2.84)$$

## 2.6 Particle Velocity in the Jet

The gas-solid particle mixture after expansion through the nozzle appears in the form of a jet at the nozzle exit. Because of the inertia effect, the solid particles do not attain the same velocity as that of the gas-phase at the nozzle exit. Thus, there exist a large slip velocity. It is possible to investigate the two-phase (gas-solid particle) jet flow in a manner analogous to the single-phase gaseous jet because of the large volume fraction of the gas-phase even when the initial concentration of the

solid particles is large. For a mixture ratio  $\alpha = 0.4$ , the volume ratio of air and solid particles is of the order of  $10^3$ . As the jet moves away from the nozzle, the volume ratio increases further due to the entrainment of surrounding air.

Because of the friction developed on its periphery, the emerging jet carries with it some of the surrounding fluid which was originally at rest. This friction also causes the jet to spread outwards in the downstream direction and a jet boundary occurs between the two streams which move at different speeds in the same general direction. Such a surface of discontinuity in the velocity of flow is unstable and gives rise to a zone of turbulent mixing downstream of the point where the two streams first meet. The width of this mixing region increases in the downstream direction. This turbulence also causes mixing of the emerging jet with the surrounding fluid. Particles of the fluid from the surroundings are carried by the jet so that mass flow increases in the downstream direction. Concurrently the jet spreads out and its velocity decreases, but the total momentum remains constant.

The theoretical as well as experimental investigations for single phase jet [103,104] have revealed that the velocity profile at any section of the jet is of universal

nature. Because of the mixing of the surrounding fluid the jet velocity decreases. Thus, there are three distinct regions in a single-phase free jet; (i) potential core, (ii) mixing zone, and (iii) main region, as shown in Fig.2.2. The potential core of the free jet is the region which extends from the nozzle exit to a position where the centre line velocity is about 98 percent of the velocity at the nozzle exit. Beyond this point the free jet centre line velocity decay is noticeable and the velocity decreases as the inverse of the distance. The theoretical velocity distribution of a turbulent round jet has been worked out by Tollmien [See Reference (104)] on the basis of Prandtl's mixing length theory [105]. Görtler has also obtained the velocity profile of jet using Prandtl's theory of free turbulence [See Reference (104)]. No analytical expression appears to be available for jet velocity in which the mixing layer and the main region are smoothly joined to each other. The literature survey reveals that most of the work is available on single-phase jet, but not much work has been done on the gas-solid particle jet.

In the present work our interest is to obtain the centre line velocity of the solid particles in gas-solid particle jet. If centre line velocity of the carrier phase (air) is known, then by using particle-phase momentum equation, the centre line velocity of the solid particles can

be estimated. For this purpose an empirical equation proposed for evaluating fluid velocity at the centre line of a single-phase air jet has been used. This velocity is then modified to take into account the effect of admixture particles. In view of these a few additional assumptions have been made along with those indicated in Sec. 2.2.

The concentration of admixture in the potential core remains constant while in the mixing zone and in the main region of the jet it varies due to entrainment of the surrounding fluid. The fluid phase velocity decays in the downstream of the jet due to transfer of momentum to the solid particles of the jet and due to the entrainment effect. The decrease in the fluid phase velocity due to transfer of momentum has been assumed to occur only in the potential core where the solid particle concentration is high. In the main region the concentration of solid particles is low, the decrease in fluid phase velocity has, therefore, been assumed to be mainly due to the entrainment effect. The concentration and the velocity profiles are assumed to be universal in nature.

Albertson et al. [106] have given an empirical expression for the centre line velocity of axially symmetric, round air jet. Albertson's equations in a slightly modified form are

$$\frac{u_{gm}}{u_{go}} = 1 \quad \text{for } x \leq x_c \quad (2.85)$$

and

$$\frac{u_{gm}}{u_{go}} = \frac{x_c}{x} \quad \text{for } x \geq x_c, \quad (2.86)$$

where  $x$  is the distance from the nozzle tip,  $u_{gm}$  is the centre line velocity of air in the jet,  $x_c$  is a constant equal to the length of the potential core ( $x_c$  has dimension of length) and  $u_{go}$  is the velocity of air at the nozzle exit. When applied to gas-solid jet, the centre line velocity of the gas does not remain constant in the potential core ( $x \leq x_c$ ) but decreases due to momentum transfer to the solid particles, i.e.,  $(u_{gm})_{x=0} \neq (u_{gm})_{x=x_c}$ . To take this effect into account, equation (2.86) has been modified by introducing another variable  $u_{gc}$  in place of  $u_{go}$ . Here  $u_{gc}$  represents the centre line velocity of the gas-phase at the end of potential core in a gas-solid particle (two-phase) jet, i.e.,  $(u_{gm})_{x=x_c} = u_{gc}$ . The velocity  $u_{gc}$  can be obtained by solving the total momentum equation of gas-solid particle mixture jet. Thus, equation (2.86) can be rewritten for the case of gas-solid particle mixture jet as

$$\frac{u_{gm}}{u_{gc}} = \frac{x_c}{x} \quad \text{for } x \geq x_c. \quad (2.87)$$

### 2.6.1 Potential Core Length

Due to entrainment of the surrounding fluid, mixture density in the mixing zone and the main region of the jet changes considerably. Therefore, rather than using the term mixture ratio it is convenient to use the term concentration or mixture density. The concentration  $\phi$  is defined as the ratio of mass flow rate of solid particle to the mass flow rate of fluid phase at any arbitrary section of the jet. Thus, the concentration  $\phi_0$  at the nozzle exit is given by

$$\phi_0 = \frac{\dot{M}_p}{\dot{M}_g} = \frac{\alpha}{(1 - \alpha)} , \quad (2.88)$$

where  $\alpha$  is the mixture ratio as defined earlier.

To obtain the length of potential core in gas-solid particle mixture jet an approach similar to that used in single phase jet flow may be considered. From the theory of turbulent mixing proposed by Prandtl [105] it has been established that the thickness  $b$  of the turbulent mixing zone of submerged jet increases in proportion to the distance  $x$  from the mixing origin. The slope of the inner edge of the boundary layer of submerged plane jet with variable density is [104]

$$\frac{y_1}{b_1} = A_0 - 2 A_1 + A_2 , \quad (2.89)$$



where  $b_1$  is the thickness of the mixing zone and  $y_1$  is the ordinate of the inner edge of the boundary layer at the end of the potential core. The quantities  $A_0$ ,  $A_1$  and  $A_2$  are expressed as

$$\left. \begin{aligned} A_0 &= \int_0^1 \frac{\rho_m}{\rho_{m0}} d\eta, \\ A_1 &= \int_0^1 \frac{\rho_m}{\rho_{m0}} g d\eta, \\ A_2 &= \int_0^1 \frac{\rho_m}{\rho_{m0}} g^2 d\eta, \end{aligned} \right\} \quad (2.90)$$

where

$$g = (1 - \eta^{1.5})^2.$$

Here  $\eta = \frac{\phi}{\phi_0}$ , is the concentration profile. The term  $\frac{\rho_m}{\rho_{m0}}$  is the ratio of the densities of the mixture at any arbitrary point in the boundary layer and in the core of constant concentration (potential core). This term  $\frac{\rho_m}{\rho_{m0}}$  can also be expressed as

$$\frac{\rho_m}{\rho_{m0}} = \frac{(1 + \phi)}{(1 + \phi_0)}. \quad (2.91)$$

Since  $\eta = \frac{\phi}{\phi_0}$ , therefore,

$$\begin{aligned}
 A_0 &= \frac{(1 + 0.5 \phi_0)}{(1 + \phi_0)} , \\
 A_1 &= \frac{(0.45 + 0.129 \phi_0)}{(1 + \phi_0)} , \\
 \text{and} \\
 A_2 &= \frac{(0.316 + 0.067 \phi_0)}{(1 + \phi_0)} .
 \end{aligned}
 \quad \left. \vphantom{\begin{aligned} A_0 \\ A_1 \\ A_2 \end{aligned}} \right\} \quad (2.92)$$

For round jet

$$y_1 = \frac{d_{no}}{2} . \quad (2.93)$$

Substituting for  $A_0$ ,  $A_1$  and  $A_2$  from equation (2.92) and for  $y_1$  from equation (2.93), equation (2.89) gives

$$b_1 = \frac{d_{no} (1 + \phi_0)}{2(0.416 + 0.309 \phi_0)} . \quad (2.94)$$

It has also been shown semi-empirically [104, 106] that

$$\frac{b_1}{x_c} = c_5 \frac{(1 + 0.5 \phi_0)}{(1 + \phi_0)} , \quad (2.95)$$

where  $c_5$  is an experimental constant which varies between 0.2 to 0.3. The smaller values of  $c_5$  are characteristic for co-flowing while the higher values are for counter flowing jets.

Substitution of equation (2.94) in equation (2.95) and taking  $c_5 = 0.27$  as obtained by Albertson et al. [106], the potential core length  $x_c$  of a gas-solid particle mixture submerged jet is

$$x_c = \frac{1.85 d_{no} (1 + \phi_o)^2}{(1+0.5 \phi_o) (0.416+0.309 \phi_o)} \quad (2.96)$$

Substitution of  $\phi_o = \frac{c}{(1-\alpha)}$  in equation (2.96) gives

$$x_c = \frac{1.85 d_{no}}{(1-0.5 \alpha) (0.416-0.107 \alpha)} \quad (2.97)$$

## 2.6.2 Flow Governing Equations of Gas-Solid

### Particle Free Jet

In the jet region of inviscid gas-phase, neglecting body force, pressure gradient and taking  $K_m = 1$  for  $u_p < u_g$  as discussed earlier, the conservation of momentum equation (2.40) for one-dimensional steady state flow gives

$$\rho_p u_p \frac{du_p}{dx} + \rho_g u_g \frac{du_g}{dx} = 0 \quad (2.98)$$

Consider an imaginary stream tube of infinitesimal cross-sectional area  $\Delta A_c$  in the centre of potential core throughout its length. Assuming the concentration of

admixture in this stream tube to be constant, the mass flow rate of gas and solid particles through this tube are

$$\dot{M}_p = \rho_p u_p \Delta A_c \quad (2.99)$$

and

$$\dot{M}_g = \rho_g u_g \Delta A_c \quad (2.100)$$

The concentration  $\phi$  in the centre of the potential core is

$$\phi = \frac{\dot{M}_p}{\dot{M}_g} = \frac{\rho_p u_p}{\rho_g u_g} = \phi_0 \quad (2.101)$$

Using equations (2.88) and (2.101), equation (2.98) for the centre of potential core becomes

$$\frac{du_{gm}}{dx} = - \frac{\alpha}{(1-\alpha)} \frac{du_{pm}}{dx} \quad \text{for } x \leq x_c, \quad (2.102)$$

where  $u_{pm}$  is the centre line velocity of particles in the jet.

For one-dimensional steady state inviscid flow of gas-solid particle mixture jet in the centre of potential core, equation (2.41) gives

$$\frac{du_{pm}}{dx} = B^{jet} \left( \frac{u_{gm}}{u_{pm}} - 1 \right) , \quad (2.103)$$

where  $B^{jet}$  is the time constant for momentum transfer in jet region. Substituting for  $\frac{du_{pm}}{dx}$  from equation (2.103) into equation (2.102) gives

$$\frac{du_{gm}}{dx} = - \frac{\alpha B^{jet}}{(1-\alpha)} \left( \frac{u_{gm}}{u_{pm}} - 1 \right) . \quad (2.104)$$

The time constant  $B^{jet}$  for momentum transfer in the jet region can be obtained using equations (2.7) and (2.10) as

$$B^{jet} = \frac{3}{4} \frac{\bar{\mu}_g}{d_p^2 \bar{\rho}_p} [28 (N_{Re}^{jet})^{-0.85} + 0.48] N_{Re}^{jet} . \quad (2.105)$$

Here particle Reynold's number  $N_{Re}^{jet}$  in jet region can be obtained by equation (2.5) in which  $\bar{\rho}_g$  is replaced by  $\bar{\rho}_{go}$  which represents the material density of air at nozzle exit conditions i.e. at atmospheric conditions. Thus,

$$N_{Re}^{jet} = \frac{\bar{\rho}_{go} d_p (u_{gm} - u_{pm})}{\bar{\mu}_g} . \quad (2.106)$$

Substitution of equation (2.97) into equation (2.87) gives the following equation for the centre line velocity of gas phase in the main region of the jet :

$$u_{gm} = \left[ \frac{1.85 d_{nc}}{(1-0.5 \alpha) (0.416-0.107 \alpha)} \right] \frac{u_{gc}}{x} \quad (2.107)$$

for  $x \geq x_c$ .

### 2.6.3 Flow Governing Equations in Dimensionless Form for Gas-Solid Particle Free Jet

Equations (2.103) and (2.104) are the flow governing equations for the potential core region of the jet i.e. for  $x \leq x_c$ , while equations (2.103) and (2.107) are the flow governing equations for the main region of the jet i.e. for  $x \geq x_c$ . Equation (2.97) gives the length of potential core. For simplicity these equations will also be represented in dimensionless form using dimensionless variables as given in equation (2.64).

Equation (2.103) rewritten in dimensionless form becomes

$$\frac{du_{pm}^*}{dx^*} = B_2^* \left( \frac{u_{gm}^*}{u_{pm}^*} - 1 \right), \quad (2.108)$$

where  $x^*$  is the dimensionless distance from the nozzle exit,  $B_2^*$  is a dimensionless constant,  $u_{gm}^*$  and  $u_{pm}^*$  are the centre line velocity in dimensionless form for gas and particle phases respectively in the gas-solid particle mixture free jet. The dimensionless constant  $B_2^*$  can be expressed as

$$B_2^* = \frac{B_{jet} d_{no}}{u_{gl}} = \frac{3}{4} \frac{\bar{\mu}_g d_{no}}{d_p^2 \bar{\rho}_p u_{gl}} N_{Re}^{jet} [28(N_{Re}^{jet})^{-0.85+0.48}] \quad (2.109)$$

Similarly, equation (2.103) rewritten in dimensionless form becomes

$$\frac{du_{gm}^*}{dx^*} = - \frac{\alpha B_2^*}{(1-\alpha)} \left( \frac{u_{gm}^*}{u_{pm}^*} - 1 \right) \text{ for } x^* \leq x_c^*, \quad (2.110)$$

where  $x_c^*$  is the potential core length in dimensionless form.

The potential core length in dimensionless form can be expressed as

$$x_c^* = \frac{x_c}{d_{no}} = \frac{1.85}{(1-0.5\alpha)(0.416-0.107\alpha)}. \quad (2.111)$$

Equation (2.107) rewritten in dimensionless form becomes

$$u_{gm}^* = \left[ \frac{1.85}{(1-0.5\alpha)(0.416-0.107\alpha)} \right] \frac{u_{gc}^*}{x^*} \quad \text{for } x^* \geq x_c^*, \quad (2.112)$$

where  $u_{gc}^*$  is the dimensionless centre line velocity of the gas phase at the end of potential core i.e. at  $x^* = x_c^*$ .

The particle Reynold's number for jet centre line in terms of dimensionless variables is

$$N_{Re}^{jet} = \frac{u_{gl} \bar{\rho}_{go} d_p}{\bar{\mu}_g} (u_{gm}^* - u_{pm}^*) . \quad (2.113)$$

## 2.7 Numerical Solution Technique

Equations (2.68), (2.69), (2.71), (2.73), (2.74), (2.75) and (2.84) are flow governing equations in dimensionless form which describe the gas-solid particle mixture flow through a convergent-straight nozzle. Equations (2.108), (2.110) and (2.112) are the dimensionless flow governing equations for the gas-solid particle mixture free jet. These systems of nonlinear differential and algebraic equations can be solved numerically to obtain the particle velocity in the nozzle as well as the jet region.

The gas phase velocity  $u_{gl}$  and density  $\rho_{gl}$  at the nozzle inlet can be obtained from equations (2.66) and (2.67), respectively. At the nozzle inlet the particle phase velocity  $u_{pl}$  has been taken to be  $c_s$  times the carrier-phase velocity  $u_{gl}$ . This factor  $c_s$  may be called particle velocity ratio and defined as the ratio of particle-phase velocity to the carrier-phase velocity at the nozzle inlet.



In abrasive jet machining the solid particles are fed from rest (zero velocity) into the mixing chamber where it is mixed with the carrier gas. The mixture of gas and solid particles are carried through a tube or pipe to the nozzle. In doing so the solid particles also get accelerated by the carrier gas and attain some velocity at the nozzle inlet. The magnitude of the velocity attained depends on the distance travelled by the solid particles in reaching the nozzle inlet and the velocity of the fluid in the conveying tube. Hence the velocity ratio  $c_s$  will be a function of the length of the conveying tube and the carrier fluid velocity in the conveying tube.

The numerical solution for evaluating the particle velocity can be carried out in two stages. In the first stage, the velocity of particle phase and gas phase is computed in the nozzle region. With the information at the nozzle exit (from the first stage of solution), the second stage of the solution gives the velocity in the jet region.

The variables  $u_g^*$ ,  $u_p^*$ ,  $T_g^*$ ,  $T_p^*$ ,  $P^*$ ,  $\rho_g^*$  and  $A_n^*$  at the nozzle inlet are known and the increments  $\Delta u_p^*$ ,  $\Delta T_p^*$ ,  $\Delta u_g^*$ ,  $\Delta T_g^*$  and  $\Delta P^*$  can be calculated using equations (2.75), (2.84), (2.74), (2.71) and (2.72), respectively for the first interval of  $\Delta x^*$  using Runge-Kutta formula for first order simultaneous differential equations. For each incremental step, the values of  $B_1^*$ ,  $N_{Re}$ ,  $A_n^*$  and  $\frac{dA_n^*}{dx^*}$  are computed from equations (2.76) to

(2.79). The increments in the succeeding intervals can be calculated exactly in the same manner except that the end of the previous interval is taken as the starting point for the next interval. In this manner, the particle phase and the gas phase velocities at the nozzle exit can be obtained.

In the second stage of the solution, equations (2.108) and (2.110) can be computed using Runge-Kutta formula for first order simultaneous differential equations to get the particle phase and gas phase velocities upto the end of potential core i.e.,  $x^* = x_c^*$ . From this the gas phase velocity  $u_{gc}^*$  at  $x^* = x_c^*$  is obtained. Using the computed value of  $u_{gc}^*$ , the gas phase velocity at sections  $x^* > x_c^*$  in the main region of the jet can be calculated from equations (2.112). Knowing the gas phase velocity in the main region of the jet, the particle phase velocity for  $x^* > x_c^*$  can be obtained by solving equation (2.108) applying Runge-Kutta formula for first order differential equation.

## CHAPTER 3

### THEORETICAL ANALYSIS OF MATERIAL REMOVAL RATE

#### 3.1 Introduction

Material removal in Abrasive Jet Machining occurs due to erosion caused by the impact of high velocity stream of abrasive particles onto the workpiece. The erosion in such situations is a complex phenomenon and is not fully understood. Adequate data for governing parameters are not available. Some of these governing parameters are interdependent and are often difficult to control. Intuitively, one might expect a large number of variables to enter the general description. Material properties (e.g. toughness, hardness, stiffness etc.), prior state of target surface (e.g. flaw density, level of surface stresses etc.), indentation parameters (e.g. indenter geometry, velocity of impact or rate of indentation etc.) are some of the factors which need to be considered. The complexities due to many interdependent variables seem to defy simplification for an experimentalist seeking to carefully separate variables and for a theorist attempting to accurately model the erosion phenomenon. In spite of these difficulties, in the present work, an attempt has been made to develop a theoretical model of erosion of brittle materials. Using the

developed erosion model an estimate of material removal rate during Abrasive Jet Machining of glass has been made.

### 3.2 General Feature of Elastic-Plastic Indentation

#### Fracture

Although a brittle material does not show plastic deformation, indentation fracture studies of brittle materials [48-51, 62,63] have shown that plastic deformation does occur even in very brittle materials like ceramics and glasses. Oh et al. [49] have shown that rather than fully elastic crack formation the elastic-plastic indentation occurs in brittle materials when the diameter of indenter is below a critical value  $d_{pc}$  (for soda lime glass  $400 \mu m > d_{pc} > 18 \mu m$ ). Thus, under solid particle impacts the mode of fracture and deformation depend not only on the velocity and properties of the impacting particles relative to those of the target but also on the size of the impacting particles.

Indentation studies [48,51,62,65] have shown that different sets of crack system are formed on the loading as well as unloading part of the indentation cycle. The sequence of events during indentation with a small spherical ball indenter for one complete indentation cycle are shown schematically in Fig. 3.1. The contact of the sphere with the surface is initially elastic (Fig. 3.1 a) and is accurately described by the Hertzian stress field. On increasing

the load, the stresses increase in proportion to the mean indentation pressure. Eventually the maximum shear stress exceeds the yield stress of the material and permanent deformation occurs (dark zone in Fig. 3.1 b).

During the loading cycle, surface ring cracks occasionally form around the area of contact. On continued loading, these ring cracks sometimes develop into cone cracks but generally a zone of plastically deformed material develops around the indenter and a median crack develops within the target beneath the area of contact (Fig. 3.1c). This median crack also grows on continued loading.

On unloading, the median crack begins to close-up owing to the compressive forces of the elastically deformed material around the indentation site (Fig. 3.1 d). However, on the surface, the elastic stresses are reversed and at about half the maximum load a system of radial cracks forms around the indentation site (Fig. 3.1 e). Most of the radial cracks are initiated from the edge of the area of contact and a few are extension of the subsurface median cracks. The system of radial cracks continue to propagate on unloading. The presence of Hertzian cone crack, if any, does not appear to influence the shape or extent of these radial cracks. As unloading proceeds the walls of the median cracks move closer but fracture debris and residual tension

once more prevent total closure. Indeed, the residual stresses may actually drive any partially formed median crack to full development. Just prior to complete unloading the residual stresses (subsurface tension component) become sufficient to initiate and propagate a completely new system of sideways spreading saucer-like lateral cracks (Fig. 3.1f). These lateral cracks continue their spread when the indenter load is finally removed, and may actually intersect the free surface to produce a chip [107]. These cracks form the basis of material removal during impact erosion of brittle materials.

### 3.3 Plastic Deformation Threshold

Erosion depends very much on the impacting particle velocity. If a small spherical particle ( $d_p \leq d_{pc}$ ) impinges onto a surface of brittle material above a certain velocity, elastic-plastic deformation occurs and radial and lateral cracks system are formed. Thus, there exists a velocity threshold to cause plastic deformation and formation of cracks system.

As soon as the spherical particle touches the surface of a flat body, stress concentrations are setup as a result of elastic deformation. Hertzian stress analysis indicates that the maximum stress concentration occurs in the centre

of the contact area at a depth of about half the radius of the projection of the contact area on the surface. As long as this maximum stress does not reach the yield strength of the target material only elastic deformation occurs and the collision is said to be perfectly elastic. On increasing the load when the maximum stress in the centre of the contact area reaches the yield strength of the target material, the target starts deforming plastically. The impact velocity at which the plastic deformation takes place can be related to the impact parameters using elastic collision formula of Hertz [108].

If the colliding bodies are spheres with one of the spheres having radius and mass infinitely large compared with that of the other, the equation expresses the collision of a sphere with a flat body. In such a situation, Hertz equation gives the maximum contact force  $(F_e)_{\max}$  during elastic collision as (Appendix-II)

$$(F_e)_{\max} = \left( \frac{20\pi}{3} \bar{\rho}_p \right)^{\frac{3}{5}} d_p^2 \left[ \frac{1}{192 \left( \frac{1-\nu_t^2}{E_t} + \frac{1-\nu_p^2}{E_p} \right)} \right]^{\frac{2}{5}} u_{\text{pim}}^{\frac{6}{5}}, \quad (3.1)$$

where  $u_{\text{pim}}$  is the velocity,  $\bar{\rho}_p$  is the material density and  $d_p$  is the diameter of impacting particle. Here  $E$  and  $\nu$

are modulus of elasticity and Poisson's ratio respectively. Suffix t represents the target material while p represents the particle material.

Hertz has further shown that the radius  $a_e$  of the projection of the contact area on the body surface is

$$a_e = \left[ \frac{3}{8} (F_e)_{\max} d_p \left( \frac{1-\nu_t^2}{E_t} + \frac{1-\nu_p^2}{E_p} \right) \right]^{1/3}. \quad (3.2)$$

The average surface pressure  $q_{av}$  can be expressed as

$$q_{av} = \frac{(F_e)_{\max}}{\pi a_e^2}. \quad (3.3)$$

Substituting equations (3.1) and (3.2) in equation (3.3) gives

$$q_{av} = \frac{2}{3} \left[ \frac{40 \bar{\rho}_p}{\left\{ \pi \left( \frac{1-\nu_t^2}{E_t} + \frac{1-\nu_p^2}{E_p} \right) \right\}^4} \right]^{1/5} u_{pim}^{2/5}. \quad (3.4)$$

Davies [109] has shown that the shear stress under a spherical indenter has a maximum value of  $0.47 q_{av}$  at approximately  $0.5 a_e$  below the surface of contact. At the onset of plastic deformation this shear stress must reach



the value of shear stress  $\sigma_{st}$  in simple tension at yielding. Thus,

$$\sigma_{st} = 0.47 q_{av} \quad (3.5)$$

Using Mises criterion, Davies has further shown that the plastic deformation sets in if  $\sigma_{st} \approx 0.5 Y_t$ , which gives

$$q_{av} = 1.06 Y_t, \quad (3.6)$$

where  $Y_t$  is the yield stress of the target material in simple tension.

Substituting the value of  $q_{av}$  from equation (3.6) into equation (3.4) and setting  $u_{pim}$  equal to  $u_{pc}$  gives

$$u_{pc} = 4.97 Y_t^{\frac{5}{2}} \left(\frac{1}{\rho_p}\right)^{\frac{1}{2}} \left[\frac{1-\nu_t^2}{E_t} + \frac{1-\nu_p^2}{E_p}\right]^2 \quad (3.7)$$

Here  $u_{pc}$  is the threshold velocity at which plastic deformation in the target material is initiated when it is impacted by a spherical particle. The yield stress  $Y_t$  can be related to the Vicker's hardness number  $H_t$ . In particular Marsh [110] has suggested that for glass the ratio of Vicker's hardness number to yield stress is approximately 1.5 rather than 3 as found conventionally for metals [111]. Substituting  $Y_t = \frac{H_t}{1.5}$ , for glass target, equation (3.7) gives

$$u_{pc} = 1.8 H_t^{5/2} \left( \frac{1}{\bar{p}_p} \right)^{1/2} \left[ \frac{1 - \nu_t^2}{E_t} + \frac{1 - \nu_p^2}{E_p} \right]^2 . \quad (3.8)$$

### 3.4 Quasi-static Approach to Dynamic Impact

Radial and lateral cracks formed during dynamic impacts [112] exhibit some similarity to that observed during quasi-static indentation [48,50,51,62]. These cracks are attributed to the development of an elastic-plastic stress field similar to that of a spherical cavity under internal pressure [50] with cracks propagating on planes normal to the maximum principal tensile stress (in the same manner as the Hertzian cracks are formed during the elastic indentation). The lateral cracks usually initiate and develop during the unloading half cycle, and are motivated by the residual elastic-plastic stress field. Further, the lateral cracks are sub-surface cracks and run parallel to the free surface below the impact site. The lateral cracking is more difficult to analyse because it is subsurface and primarily dependent upon the proximity of the free surface. Due to these complexities in the elastic-plastic residual stress analysis, the propagation of the lateral cracks has not yet been fully explained, [50,51]. Under impact conditions the stress-fracture inter-relations in the plastic response regime are expected to

be even more complex than for the quasi-static indentation. Further, the shock waves, plastic and elastic waves and their interactions with rapidly moving cracks during impact, complicates the analysis. Because of these complexities the quasi-static indentation approach has been used to predict the erosion loss under impact situations in the present work. This approach is similar to that used by Evans and Wilshaw [50]. It is assumed that lateral cracks grow in a quasi-static manner as a result of residual stresses produced by the impact event. The elastic Hertz equations are extended for plastic load also. This approximation has been found to be reasonably valid for prediction of erosion loss at low velocity ( $\leq 160$  m/sec.) impacts [112].

### 3.5 Mechanics of Erosion

During solid particle impact erosion, the material removal may occur due to crushing of target surface under impact and/or due to interaction of lateral cracks. Crushing part of erosion is more dominant for large particle impacts, while the lateral crack interaction is mainly responsible for erosion loss for small particle ( $d_p \leq d_{pc}$ ) impacts. Under such situations when impacting particles are small ( $d_p \leq d_{pc}$ ) the erosion volume can be obtained by knowing the depth and size of the lateral crack.

### 3.5.1 Lateral Crack Depth

Consider an elastic-plastic collision where the colliding particle is spherical in shape and deforms only elastically, while the target surface deforms both elastically and plastically. For elastic-plastic impact, using Hertz analysis Bitter [16] has shown that the depth of elastic penetration  $z_e$  (Fig. 3.2) is related to the maximum surface pressure  $q_{\max}$  occurring in the centre of the contact area and is given by

$$z_e = \frac{\pi^2}{8} q_{\max}^2 d_p \left[ \frac{(1-\nu_t^2)}{E_t} + \frac{(1-\nu_p^2)}{E_p} \right]^2 \quad (3.9)$$

According to Hertz the average surface pressure  $q_{av} \approx \frac{2}{3} q_{\max}$ . The largest specific load that can be exerted upon a body without causing plastic deformation is called the elastic load limit ( $\sigma_{yt}$ ). Therefore the highest average surface pressure that can be reached during a perfectly elastic impact is  $\frac{2}{3} \sigma_{yt}$ . Thus, the elastic load limit can be expressed in terms of average surface pressure as

$$\sigma_{yt} = 1.5 q_{av} \quad (3.10)$$

Substituting for  $q_{av}$  from equation (3.6), equation (3.10) gives

$$\sigma_{yt} = 1.59 Y_t . \quad (3.11)$$

It is assumed that the target material undergoes plastic deformation at constant yield stress without strain hardening. After elastic load limit is reached, plastic deformation sets in at the centre of contact area. On further penetration of the particle into the workpiece, the area which is loaded to the stress value  $\sigma_{yt}$  increases. The total depth  $z_t$  during elastic-plastic impact will, therefore, be

$$z_t = z_e + z_p , \quad (3.12)$$

where  $z_p$  is the depth of concavity due to plastic deformation.

At the end of loading cycle during impact, the edge of the concavity (edge of the plastically deformed area) is just loaded to a pressure equal to  $\sigma_{yt}$ . Outside the plastically deformed contact zone the sphere also touches the target surface, but the specific load decreases from  $\sigma_{yt}$  at the edge of the concavity to zero at the edge of

the total contact area and the deformation is purely elastic (Fig. 3.2).

Let the projection of the total contact area normal to the target surface has a radius  $a_t$ . In practice  $z_e$  and  $z_p$  are small compared to the particle size  $d_p$ . Therefore, the total contact area may be approximated by

$$\pi a_t^2 \simeq \pi d_p (z_e + z_p) \quad . \quad (3.13)$$

Similarly if the radius of the projection of the plastically deformed area is  $a_p$ , then

$$\pi a_p^2 \simeq \pi d_p z_p \quad . \quad (3.14)$$

The elastically loaded area can be obtained as

$$\pi a_t^2 - \pi a_p^2 \simeq \pi d_p z_e \quad . \quad (3.15)$$

Equation (3.15) shows that during elastic-plastic impacts the size of the contact area subjected to elastic deformation only is independent of the size of the indentation formed. Further, this is equal to the Hertzian contact area in a perfectly elastic impact in which  $q_{\max}$  just equals  $\sigma_{yt}$ . If we assume the average indentation

pressure  $q_{av}$  in this area to be equal again to  $\frac{2}{3} \sigma_{yt}$ , equation (3.4) can be used to calculate the elastic impact velocity  $u_{pe}$  and thereby the elastic part of the energy  $X_e$  absorbed in this region. The elastic impact velocity can now be expressed as

$$u_{pe} = \frac{\pi^2}{2\sqrt{10}} \sigma_{yt}^{5/2} \left( \frac{1}{\bar{\rho}_p} \right)^{1/2} \left[ \frac{(1 - \nu_t^2)}{E_t} + \frac{(1 - \nu_p^2)}{E_p} \right]^2 . \quad (3.16)$$

Substitution of equation (3.11) into equation (3.16) gives

$$u_{pe} = u_{pc} . \quad (3.17)$$

Thus, the impact energy spent in elastic deformation  $X_e$  is

$$X_e = \frac{1}{2} m_p u_{pc}^2 , \quad (3.18)$$

where mass of impacting particle  $m_p = \frac{\pi}{6} \bar{\rho}_p d_p^3$ .

The elastic reaction forces are set up at the end of the impact cycle as a result of this elastic impact energy. The elastic reaction forces then press the particle out of the body (target) giving the particle an amount of kinetic energy equal to the stored elastic deformation

energy. From the energy balance of collision cycle, Bitter [16] has been able to show that the energy absorbed by the target during plastic deformation  $X_p$  is

$$X_p \simeq (\sqrt{X_{im}} - \sqrt{X_e})^2, \quad (3.19)$$

where  $X_{im}$  is the impact energy of the colliding particle.

Formation of plastic indentation requires an amount of energy equal to the plastic deformation work in penetrating the particle to a depth  $(z_p)_{max}$  during indentation cycle. This gives

$$X_p = \int_0^{(z_p)_{max}} \pi a_p^2 \sigma_{yt} dz \simeq \frac{1}{2} \pi d_p (z_p)_{max}^2 \sigma_{yt}. \quad (3.20)$$

If the particle impacts onto the target surface with a velocity  $u_{pim}$ , the impact energy of the colliding particle is

$$X_{im} = \frac{1}{2} m_p u_{pim}^2. \quad (3.21)$$

Substitution of  $X_e$  from equation (3.18),  $X_p$  from equation (3.20) and  $X_{im}$  from equation (3.21) into equation (3.19) gives



$$(z_p)_{\max} = \left(\frac{\bar{p}_p}{6\sigma_{yt}}\right)^{\frac{1}{2}} d_p (u_{pim} - u_{pc}) \quad (3.22)$$

Using equation (3.14), the maximum radius of projection of the plastically deformed area,  $(a_p)_{\max}$  can be expressed as

$$(a_p)_{\max} \simeq \sqrt{d_p (z_p)_{\max}} \quad (3.23)$$

Substituting for  $(z_p)_{\max}$  from equation (3.22) into equation (3.23) gives

$$(a_p)_{\max} \simeq \left(\frac{\bar{p}_p}{6\sigma_{yt}}\right)^{\frac{1}{4}} d_p (u_{pim} - u_{pc})^{\frac{1}{2}} \quad (3.24)$$

Hill's analysis [113] for the expansion of a spherical cavity under internal pressure in an elastic-plastic solid was extended by Johnson [114] to analyse the elastic-plastic indentation. In Johnson's analysis the analogy of expansion of a spherical cavity with internal pressure has been taken for the plastically deformed zone (hydrostatic zone) about the indenter. According to Hill [113] the size of the plastic zone  $C_o$  is expressed as

$$C_o \simeq a_p \left[ \frac{E_t}{3(1-\nu_t)\bar{Y}_t} \right]^{1/3} \quad (3.25)$$

Outside the plastic zone the material is loaded only elastically. Thus, the elastic-plastic boundary occurs at a depth  $C_0$  below the target surface.

Evans et al. [63] and others [50,51,53] have suggested that the lateral cracks initiate at the elastic-plastic boundary. Thus, the lateral crack depth  $z_1$  can be approximated by the size of elastic-plastic boundary which gives

$$z_1 \approx C_0 \approx a_p \left[ \frac{E_t}{3(1-\nu_t) Y_t} \right]^{1/3} . \quad (3.26)$$

From the available data of mechanical properties for different glasses, Table 3.1, the quantity  $\left[ \frac{E_t}{3(1-\nu_t) Y_t} \right]^{1/3}$  has been calculated and found to be constant ( $\approx 2$ ). Thus, the lateral crack depth for glasses and similar brittle materials (ceramics) can be expressed as

$$z_1 \approx 2 a_p . \quad (3.27)$$

For full penetration at the end of impact cycle  $a_p = (a_p)_{\max}$ . Substituting for  $(a_p)_{\max}$  from equation (3.24) into equation (3.27) gives

$$z_1 \approx 2 \left( \frac{\bar{\rho}_p}{6\sigma_{yt}} \right)^{1/4} d_p (u_{pim} - u_{pc})^{1/2} . \quad (3.28)$$

Substituting for  $\sigma_{yt}$  from equation (3.11) into equation (3.28) and taking  $Y_t = \frac{H_t}{1.5}$ , the expression for lateral crack depth into the glass target is

$$z_1 \simeq 1.26 \left( \frac{\bar{\rho}_p}{H_t} \right)^{1/4} d_p (u_{pim} - u_{pc})^{\frac{1}{2}} . \quad (3.29)$$

Equation (3.29) gives the estimate of lateral crack depth in glasses and similar brittle materials (ceramics). This expression is similar to that obtained by Evans et al. [63], with the only difference that the present expression takes into account the velocity threshold effect. Equation (3.29) has been found to be in good agreement with the experimental data for lateral crack depth (Table 3.2).

### 3.5.2 Lateral Crack Length

During unloading part of the indentation cycle irreversibly deformed material within the plastic zone is directly responsible for the formation of a residual elastic stress field which provides the driving force for lateral crack extension. Any numerical or rigorous analytical solution of the stress fields due to plastic indentation is likely to be complicated by non-linear deformation behaviour. The complexity of analysis is further increased because of the dynamic nature of the problem and the effect

of indenter geometry on the material behaviour. In view of these complexities and the current state of knowledge of the indentation stress field, a semi-empirical approach has been adopted to express the lateral crack length  $C_1$  in terms of impact parameters.

Evans and Wilshaw [50] have expressed the normalized lateral crack length in terms of dimensionless functions of different variables influencing the crack extension phenomenon as

$$f_1\left(\frac{C_1}{a_p}\right) = \frac{K}{Y_t \sqrt{a_p}} f_2^{-1}\left(\frac{C_0}{a_p}\right) f_3^{-1}(\nu_t) f_4^{-1}(\gamma), \quad (3.30)$$

where  $f_{1-4}$  are dimensionless functions,  $K$  is stress intensity factor,  $\gamma$  is coefficient of friction at the indenter and target interface and  $\nu_t$  is Poisson's ratio of the target material.

The uniaxial yield stress is related to the hardness of the material by [115]

$$\frac{H_t}{Y_t} = 0.28 + 0.6 \left[ \frac{3}{3 - (1 - 2\nu_t)\left(\frac{Y_t}{E_t}\right)} \right] \ln \left[ \frac{3(E_t/Y_t)}{(4 + \nu_t) - \left(\frac{Y_t}{E_t}\right)(1 - 2\nu_t)(1 + \nu_t)} \right] \quad (3.31)$$

which for small  $\frac{Y_t}{E_t}$  ( $\leq 0.1$ ) reduces to

$$\frac{H_t}{Y_t} = 0.6 \ln\left(\frac{E_t}{Y_t}\right) + 0.28 + 0.6 \ln\left(\frac{3}{4 + \nu_t}\right) \equiv Q. \quad (3.32)$$

Here  $Q$  is a material constant. Substituting for  $Y_t$  from equation (3.32) and setting  $K$  equal to  $K_c$  (the crack propagation condition) equation (3.30) gives

$$f_1\left(\frac{C_1}{a_p}\right) = \frac{K_c Q}{H_t \sqrt{a_p}} \left[ f_2^{-1}\left(\frac{C_0}{a_p}\right) f_3^{-1}(\nu_t) f_4^{-1}(\gamma) \right]. \quad (3.33)$$

Here  $K_c$  is the fracture toughness of the target material which represents the resistance to crack propagation and is a material property. In this equation the terms within the square bracket remain almost constant since the friction coefficient  $\gamma$  for a fixed profile indenter is only marginally influenced by the material properties and may be assumed to be constant, Poisson's ratio  $\nu_t$  being small (0.22 - 0.3) does not exert a dominant influence on the residual stress field, and the term  $\frac{C_0}{a_p}$  is essentially a constant. Evans and Wilshaw [50] have taken functions  $f_2$ ,  $f_3$  and  $f_4$  in equation (3.33) as approximately constants and independent of the material and have expressed the normalized lateral crack

length as a function depending primarily on the quantity  $\frac{K_{IC}}{H_t \sqrt{a_p}}$ . They have obtained a plot of the normalized lateral crack length  $\frac{C_1}{a_p}$  as a function of the normalized fracture toughness  $K_{IC}/H_t \sqrt{a_p}$  for a variety of target materials as shown in Fig. 3.3(b). They have further shown that the lateral fracture is independent of the crack formation load and the surface condition (surface flaws) but dependent on the plastic zone and the residual stress in the vicinity of the elastic-plastic boundary. Once plastic indentation has occurred the peak stress and the stress distribution remains essentially constant (except for the increase due to work hardening), and only spatial extension of the stress field takes place as indentation proceeds. Thus, the applied load (contact force) can influence  $f_1(C_1/a_p)$  value only through the spatial stress field extension. This specifies that the probability of crack propagation increases as the volume of stressed material as determined by the impression diameter, increases or when the critical crack propagation stress decreases. The volume dependence thus provides a critical force condition, and the critical stress requirement provides a microstructure dependence. Using the plot of Figs. 3.3 (a & b) and relating the target hardness  $H_t$  with the contact force  $F_p$  during plastic indentation, for  $\frac{C_1}{a_p} \approx 2$ , Evans and Wilshaw [50] have expressed

the lateral crack length by the following approximate proportionality :

$$c_l \propto \left( \frac{F_p}{K_c} \right)^{3/4} . \quad (3.34)$$

Equation (3.34) can be used to obtain pertinent information about the lateral crack extension if the contact force during plastic indentation is known.

The contact force during plastic indentation does not remain constant but varies with the depth of penetration. No analytical solution appears to be available which relates  $F_p$  with  $z_p$ . Using numerical solution and fitting an empirical relation for the contact force (non-work hardening target material), Evans and Wilshaw [50] have expressed the relationship between  $F_p$  and  $z_p$  as

$$F_p = 2.545 G_t \sqrt{a_p} z_p^{3/2} , \quad (3.35)$$

where  $G_t$  is the shear modulus of the target.

For full penetration during plastic indentation i.e.,  $z_p = (z_p)_{\max}$ , equations (3.22) and (3.35) give the maximum contact force  $(F_p)_{\max}$  as

$$(F_p)_{\max} = 0.664 G_t d_p^2 \left( \frac{\bar{\sigma}_p}{\sigma_{yt}} \right)^{3/4} (u_{pim} - u_{pc})^{3/2} . \quad (3.36)$$

Substituting  $F_p = (F_p)_{\max}$ , equations (3.36), (3.34) and (3.11) give

$$C_1 \propto \left( \frac{G_t}{K_c} \right)^{3/4} d_p^{3/2} \left( \frac{\bar{\sigma}_p}{Y_t} \right)^{9/16} (u_{pim} - u_{pc})^{9/8} . \quad (3.37)$$

Substituting for  $Y_t$  in terms of the target hardness ( $Y_t = \frac{H_t}{1.5}$  for glasses), equation (3.37) can be rewritten as

$$C_1 \propto \left( \frac{G_t}{K_c} \right)^{\frac{3}{4}} d_p^{\frac{3}{2}} \left( \frac{\bar{\sigma}_p}{H_t} \right)^{\frac{9}{16}} (u_{pim} - u_{pc})^{\frac{9}{8}} . \quad (3.38)$$

### 3.6 Material Removal Rate

Material removal during solid particle impact may be assumed to occur due to intersection of lateral cracks from adjacent impacts. The material is removed in the form of micro-size chips. These micro-size chips may be assumed to be cylindrical in shape having radius equal to the lateral crack length  $C_1$  and depth equal to the lateral crack depth  $z_1$  produced under the impact. Thus, the volume of material removed per impact ( $v$ ) may be expressed as

$$v = \pi C_1^2 z_1 . \quad (3.39)$$



Substituting for  $z_1$  and  $C_1$  from equations (3.29) and (3.38) into equation (3.39) gives

$$v \propto \left( \frac{G_t}{K_c} \right)^{\frac{3}{2}} d_p^4 \left( \frac{\rho_p}{H_t} \right)^{\frac{11}{8}} (u_{pim} - u_{pc})^{\frac{11}{4}} . \quad (3.40)$$

Equation (3.40) gives the volume of material removed from the target surface during a single impact.

As mentioned earlier, in AJM high velocity air-abrasive mixture jet issued from a nozzle impinges onto the workpiece surface. Material removal occurs due to erosion caused by multiple particle impacts. Assuming that all particles in the jet during impact have velocity  $u_{pm}$  equal to that at the centre of jet and have negligible particle-particle interaction effect, the cumulative effect of multiple particle impact can be obtained by direct multiplication of the number of impacts with the volume removed by a single impact.

The number of impacts per unit time can be estimated from the number of particles passing per unit time at any section of the air-abrasive mixture jet. Thus, the number of impacts per unit time depends on the mass flow rate of abrasive particles in the jet, material density of the particle and size of the particle. The number of impacts per unit time  $N_p$  can be expressed as

$$N_p = \frac{6 \dot{M}_p}{\pi d_p^3 \bar{\rho}_p} \quad (3.41)$$

Considering multiple particle impact, the volumetric material removal rate  $V_r$  in AJM can be expressed as

$$V_r = N_p v \quad (3.42)$$

Taking  $u_{pim} = u_{pm}$ , equations (3.40), (3.41) and (3.42) give

$$V_r \propto \frac{\dot{M}_p d_p G_t^{\frac{3}{2}} \bar{\rho}_p^{\frac{3}{8}} (u_{pm} - u_{pc})^{\frac{11}{4}}}{K_c^{3/2} H_t^{11/8}} \quad (3.43)$$

Equation (3.43) gives material removal rate for machining of brittle materials such as glass, ceramics etc. in terms of proportionality equation. When applied to real situations of abrasive jet machining process the effective number of impacts onto the workpiece surface per unit time is likely to be less than the number  $N_p$  calculated from equation (3.41) because of the particle-particle interaction effect. The particle-particle interaction effect primarily depends on the stand-off distance. At small stand-off distances due to less flaring and high particle concentration in

the jet the rebounded particles from the workpiece surface collide with the incoming particles of the jet and reduces the effective number of impacts onto the workpiece surface per unit time. Thus, the effective number of impacts will be negligibly small at nearly zero stand-off distance. When the stand-off distance is high the particle-particle interaction effect is low gives large number of effective impacts approaching to the value  $N_p$ . Further, the particle-particle interaction effect will be more at high mixture ratio due to large number of particles per unit volume of the mixture. But for the sake of simplicity the effect of mixture ratio on particle-particle interaction effect has not been considered in the present analysis. Introducing a term  $\lambda$  as a function of stand-off distance to take into account these effects in real situations, equation (3.43) can be rewritten as

$$V_r = \frac{\lambda \dot{M}_p d_p G_t^{\frac{3}{2}} \rho_p^{\frac{3}{8}} (u_{pm} - u_{pc})^{\frac{11}{4}}}{K_c^2 H_t^{\frac{11}{8}}} . \quad (3.44)$$

The term  $\lambda$  can be evaluated from a typical experimental data.

TABLE 3.1

Elastic Constants of Different Glasses [51] and  $\left[ \frac{E_t}{3(1-\nu_t)} \frac{Y_t}{Y_t} \right]^{1/3}$   
Values.

Glasses	Young's Modulus ( $E_t$ ) GPa	Vicker's Hardness ( $H_t$ ) GPa	Poisson's Ratio ( $\nu_t$ )	Yield Stress ( $Y_t$ ) GPa	$\left( \frac{E_t}{3(1-\nu_t)} \frac{Y_t}{Y_t} \right)^{1/3}$
Soda lime	69	5.60	0.25	3.73	2.02
CaAlSi	98	6.80	0.26	4.53	2.13
CaAl	103	8.10	0.30	5.40	2.08

# Lateral Crack Depth

S. No.	Target Material	Impacting Particle Material	Particle Size ( $d_p$ ), $\mu\text{m}$	Velocity of Impact ( $u_{pim}$ ) m/sec	Threshold Velocity* ( $u_{pc}$ ) m/sec	Material Crack Depth* ( $z_1$ ), $\mu\text{m}$	Measured Value of Lateral Crack Depth ( $z_1$ ), $\mu\text{m}$ [After Evans et al. (63)]
1	ZnS	WC	400	130	0.26	303	270
2	ZnS	WC	1000	170	0.26	866	800
3	ZnS	Glass (Quartz)	1000	350	2.10	807	780
4	MgF <sub>2</sub>	SiC	1120	89	4.98	353	300
5	MgF <sub>2</sub>	SiC	1120	137	4.98	442	430
6	Si <sub>3</sub> N <sub>4</sub>	SiC	1120	137	28.24	311	270

\* Theoretical values have been calculated using data for physical properties of target and impacting particle materials given in Reference [63].

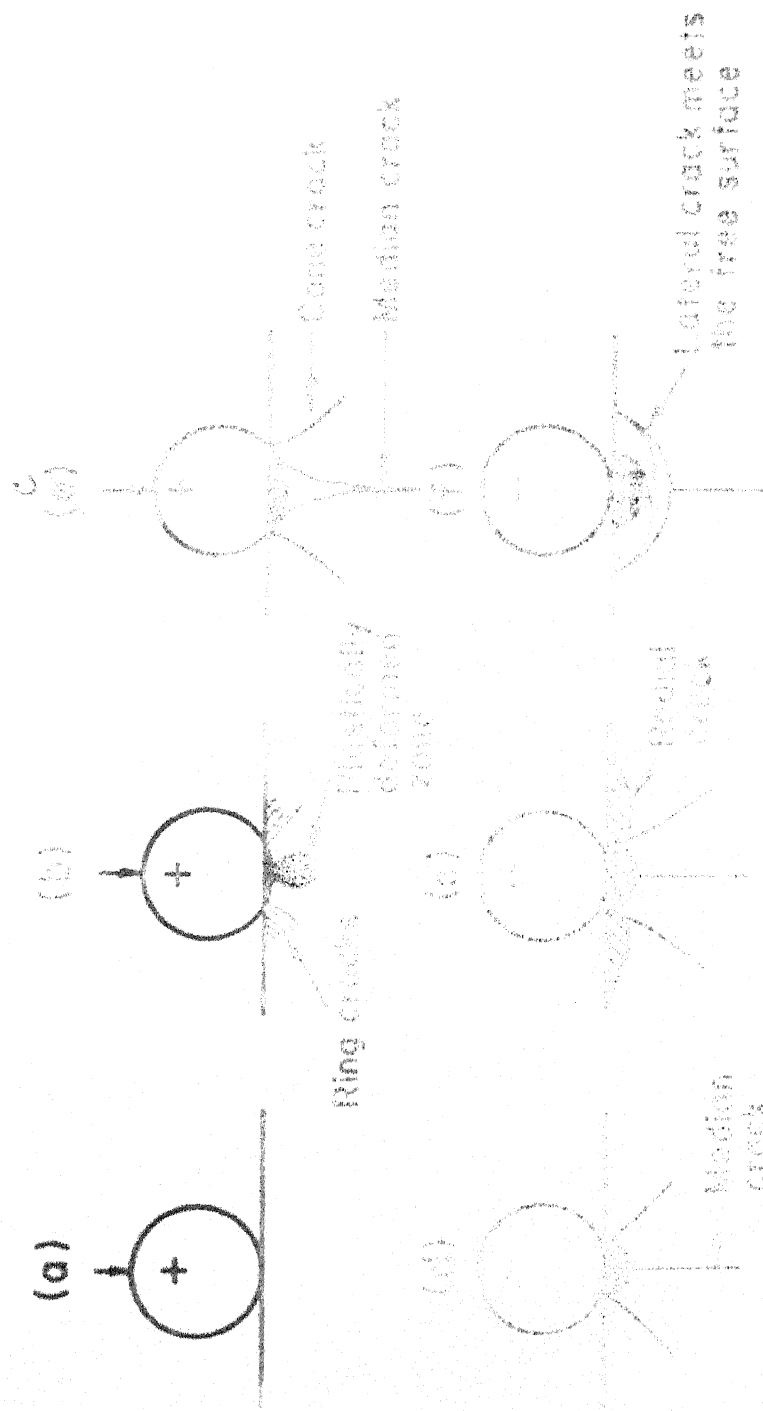


Fig. 6. Schematic diagram of the cracking occurring during a loading-unloading cycle with a small spherical indenter.

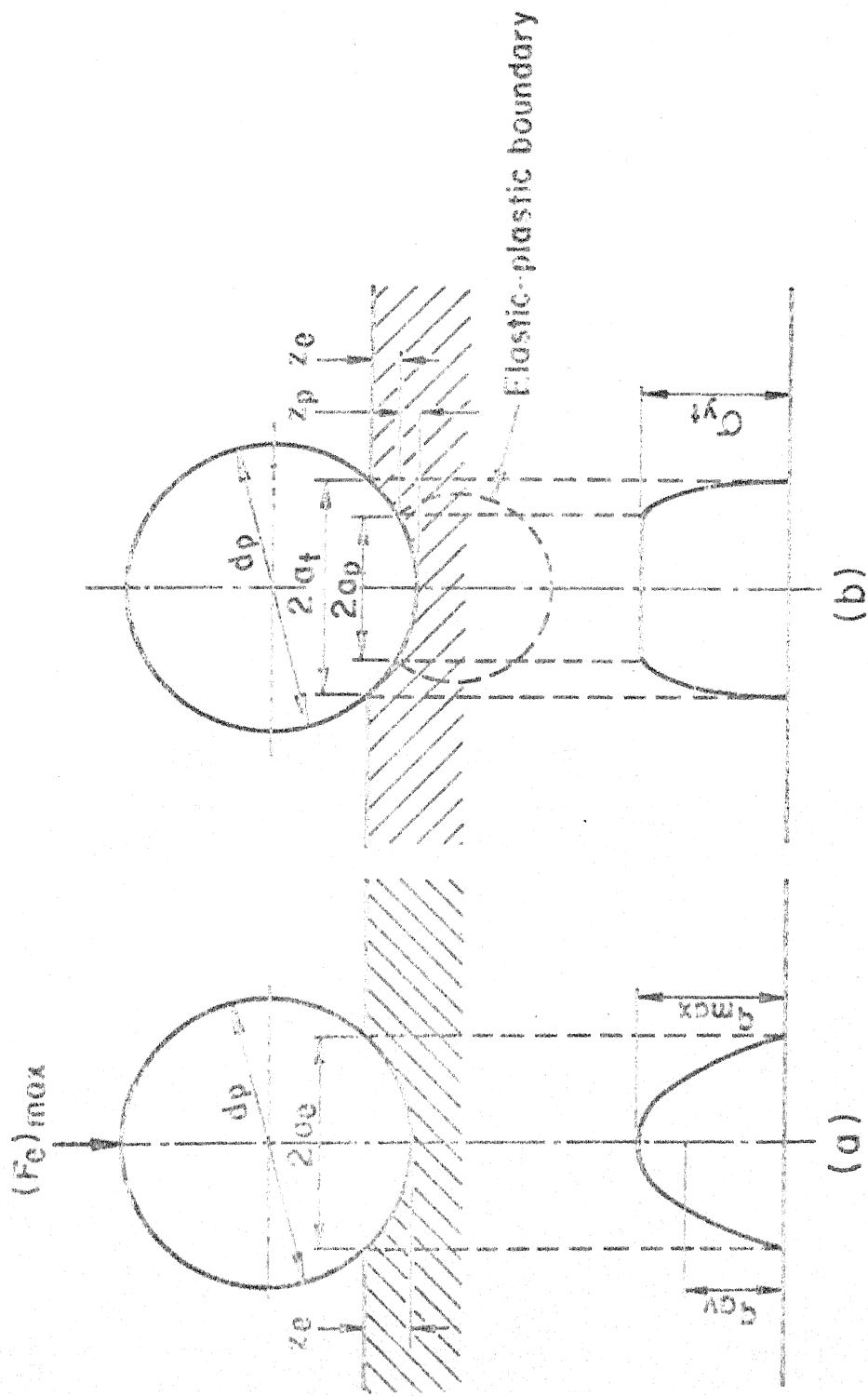


Fig.3.2 Pressure distribution at contact area  
 (a) elastic impact (b) elastic-plastic impact.

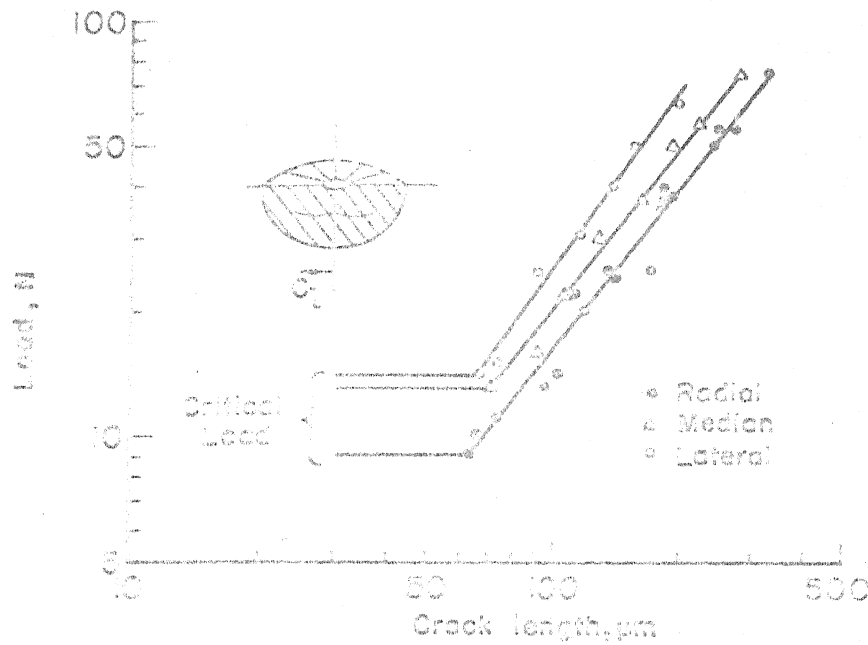


Fig. 3.5(c) Load, crack length data for radial, median and lateral cracks in zinc sulphide, obtained for a spherical indenter, 800 μm dia. [After Evans and Wilshaw (50)].

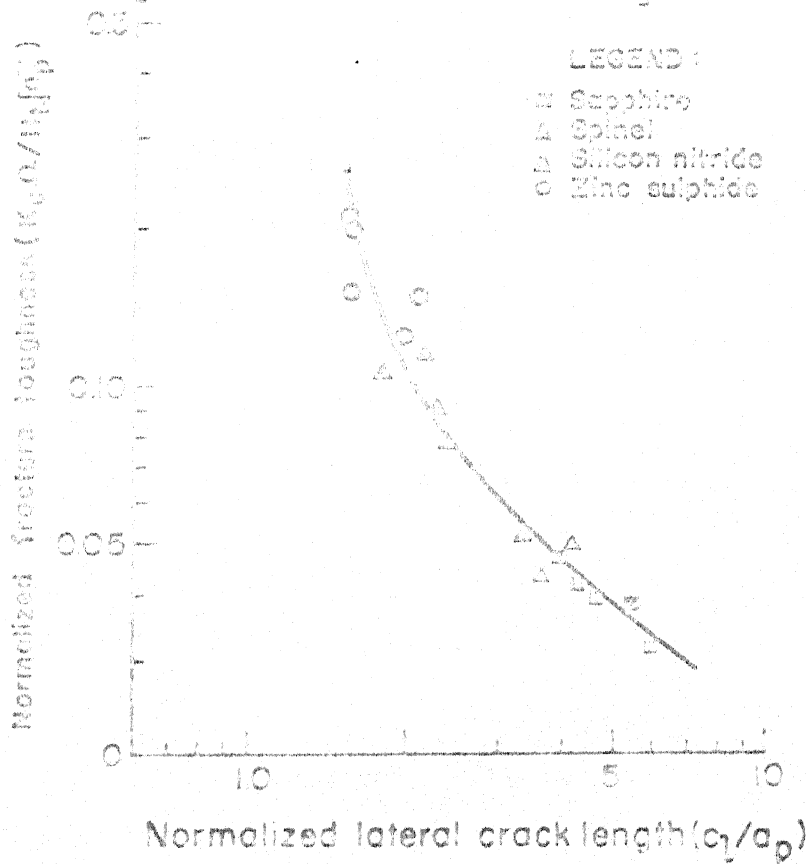


Fig. 3.3(b) The normalized lateral crack length as a function of the normalized fracture toughness [After Evans and Wilshaw (50)].



## CHAPTER 4

### EXPERIMENTS

#### 4.1 Introduction

Experiments have been conducted on an experimental abrasive jet machine specially designed and fabricated for the purpose. The present chapter deals with the design aspects of this abrasive jet machine and the experimental investigations of various input parameters affecting erosion rate and nozzle wear. During the first phase of the experimental study, the effect of various input parameters such as stand-off distance, grain size, mixture ratio, carrier fluid pressure etc. on volumetric erosion rate, penetration rate, diameter of eroded cavity etc. have been studied. In the second phase, experiments have been carried out to investigate the effect of nozzle diameter, nozzle length and entrance angle on nozzle wear. The other parameters which have been considered for the wear study are mixture ratio and abrasive particle size.

#### 4.2 Experimental Set-up

The schematic layout of the abrasive jet machining set-up is shown in Fig. 4.1. Dry air from the compressor (1) through dehumidifier and filter (4) is allowed to enter

the mixing chamber (8) through a pressure regulator (5). The pressure regulator enables regulation of inlet pressure to the system. The flow meter (6) and the pressure gauge mounted on the outlet end of the pressure regulator indicate the flow rate and the pressure of air entering into the mixing chamber. Fine grained abrasive particles stacked in the main abrasive chamber (18) flow down under gravity action into the secondary abrasive chamber (17) through a metering tube (16). The metering tube maintains a constant head of abrasive particles in the secondary abrasive chamber irrespective of the abrasive particle head (stock of abrasive particles) in the main abrasive chamber. Abrasive particles from the secondary abrasive chamber flow through the abrasive metering venturi (15), under the action of a mechanical vibrator (7), into the mixing chamber where it is mixed with the incoming air. The abrasive flow from the secondary abrasive chamber is controlled by adjusting the amplitude and frequency of the mechanical vibrator attached to the secondary abrasive chamber. The amplitude of vibration can be adjusted by adjusting the throw of eccentric driving the slider block of the vibrator unit. The frequency can be varied by varying the rpm of the motor driving the eccentric unit of the mechanical vibrator. The mixing chamber, the secondary abrasive chamber and the main abrasive chamber are maintained at uniform pressure through pressure equalizer

tubes. Hence, the abrasive flow in the system is not influenced by the pressure and flow rate of air and a precisely controlled air-abrasive mixture can be obtained at any desired nozzle pressure. The air-abrasive mixture is then directed through a flexible tube to the nozzle fitted in the nozzle holder. The nozzle holder facilitates easy, accurate and leak proof holding of nozzles. The mixture of air-abrasive particles appears in the form of a stream of air-abrasive jet at the nozzle exit. The nozzle and its holder (14) is mounted on vertical and horizontal slides for accurate location of the nozzle tip from the workpiece. The pressure gauge (9) connected to the nozzle holder reads the mixture pressure at nozzle inlet. The workpiece (11) is mounted on a fixture (12) inside a closed working chamber (10). The working chamber is connected to a vacuum cleaner (13) for removal of abrasive along with the swarf. Photographic views of the set-up are shown in Fig. 4.2(a & b).

#### 4.3 Design Considerations

In AJM, suitably proportioned air-abrasive mixture from the mixing chamber is carried pneumatically to the nozzle through a flexible tube. For pneumatic conveying of solid particles through a pipe a certain minimum velocity

of the carrier fluid is required to keep the particles in suspension [115-118]. This minimum velocity is also known as the minimum transport velocity or the saltation velocity. When velocity of carrier fluid in any part of the transport system falls below the saltation velocity, the solid particles may settle out of the flowing stream and may cause irregular flow of mixture. Thus, the units of AJM through which air-abrasive mixture is flowing must be designed to maintain the saltation velocity for the specified values of mixture ratio, working pressure, type of abrasive particles, size of abrasive particles and the exit diameter of the nozzle.

The saltation velocity for pneumatic conveying of solid particles in horizontal tubes can be estimated by the method proposed by Zenz [115]. In AJM under real situations flow of mixture in conveying tube neither conforms to horizontal conveying nor to vertical conveying, but to a close approximation it may be treated as conveying through inclined tubes. According to Zenz and Othmer [118] there is no marked change in the saltation velocity when the conveying tube is inclined as much as 10 degrees from horizontal. Further, they have shown that for intermediate positions 22 to 45 degrees from the horizontal, the saltation velocity may be taken to be 1.5 to 3 m/sec higher than in the horizontal conveying.

In AJM the mixture ratios used are generally below 0.5, the abrasive particles used are usually in the range of 10 to 50  $\mu\text{m}$  and the carrier fluid pressure used is generally in the range of 196.2 to 588.6  $\text{kN/m}^2$  (gauge) [3-6]. In the present case the set-up has been designed for system inlet pressure of 0.5  $\text{MN/m}^2$  (abs) with the nozzle exit at atmospheric pressure [0.101  $\text{MN/m}^2$  (abs)]. For adiabatic flow through convergent nozzles it has been shown that when the nozzle exit pressure reaches a value equal to or less than 0.528 times the inlet pressure, the nozzle exit velocity becomes sonic (340 m/sec) [119]. In the present set-up convergent-straight nozzles are used with exit pressure of 0.202 times the inlet pressure and hence, the carrier fluid will attain sonic velocity at the nozzle exit. Taking the mixture ratio to be 0.4, the maximum size of  $\text{Al}_2\text{O}_3$  particles to be 50  $\mu\text{m}$ , the minimum nozzle diameter to be 0.7 mm and the carrier fluid velocity at nozzle exit to be 340 m/sec, the saltation velocity  $u_{gs}$  for horizontal conveying is 0.62 m/sec as shown in Appendix-III. The minimum safe velocity of carrier fluid  $u_{gst}$  in the mixture conveying tube can, therefore, be taken as 3.62 m/sec.

As mentioned earlier, the abrasive particles are fed from the secondary abrasive chamber, through the metering venturi which is connected to it, into the mixing chamber under the action of the mechanical vibrator. The mixing

chamber is held in the vertical position and is connected to the secondary abrasive chamber through the metering venturi. High pressure air enters at the top of the mixing chamber and is mixed with abrasive particles entering through the metering venturi which is connected on one side of the mixing chamber. The vertical orientation of mixing chamber facilitates in easy fall of abrasive particles under gravity action in the mixing chamber from the metering venturi. Thus, the flow of air-abrasive mixture in the mixing chamber is in vertically downward direction.

The minimum velocity of carrier fluid for vertical conveying, known as choking velocity ( $u_{gch}$ ), is generally taken to be equal to  $u_{gs}$  for conveying of uniform size particles, and 0.2 to 0.33 times  $u_{gs}$  for conveying of mixed size particles [120]. Thus, for the working conditions stated earlier, the minimum safe velocity of carrier fluid  $u_{gch}$  in the mixing chamber has been taken to be 0.62 m/sec. On the basis of minimum safe velocities of carrier fluid in the mixing chamber and in the mixture conveying tube for a minimum nozzle diameter of 0.7 mm, the maximum diameters of the mixing chamber and the mixture conveying tube come out to be 7.3 mm and 3 mm, respectively as shown in Appendix-IV.

The air compressor capacity is selected on the basis of flow requirement for the maximum nozzle diameter in the working pressure range. Since working pressure range for

carrying out the experiments has been chosen to be 344.863 to 372.453 kN/m<sup>2</sup> (gauge) and maximum nozzle diameter as 1.62 mm, a compressor with working pressure of 400 kN/m<sup>2</sup> (gauge) and discharge capacity of  $0.725 \times 10^{-3}$  m<sup>3</sup>/sec will be sufficient for the purpose.

#### 4.4 Preliminary Experiments

The set-up was designed and fabricated taking into account the design considerations indicated and was initially operated for a few hours to check for leakage at various joints. After ensuring no leakage condition, the set-up was used for experiments.

In the present set-up, various values of abrasive flow rates were obtained by varying the frequency of vibration. The necessary calibration to this effect was carried out. For obtaining the flow rate, the abrasive jet was directed into water for two minutes at the specified frequency of vibration and then the abrasive particles were filtered and dried to obtain the weight. Calibration curves for abrasive flow rate for different particle sizes are shown in Fig. 4.3.

Preliminary experiments have been carried out using Al<sub>2</sub>O<sub>3</sub> abrasive particles of grain sizes ranging from 25 to 48 μm for both volumetric erosion as well as nozzle wear studies. The most suitable range of grain size appeared to

be 30 to 38  $\mu\text{m}$ . Coarse grains caused excessive damage to the mixture conveying tube while fine particles often caused choking. Though a wide range of mixture ratio (0.052 to 0.308) has been used but most of the experiments have been carried out only in the range of 0.052 to 0.268 to avoid excessive damage to the mixture conveying tube and for convenience in setting the motor rpm and the air flow rate. The procedure for calculation of mixture ratio is given in Appendix-V.

All machining tests have been performed on ordinary glass testpieces by directing the air-abrasive jet at 90 degrees to the work surface using tungsten carbide nozzles of circular cross-section having 0.712 mm exit diameter and convergent-straight geometry (Fig. I.1). The machining (cavity drilling) tests have been carried out at different stand-off distances ranging from 2 to 20 mm. Beyond 20 mm stand-off distance, the top diameter of eroded cavity was not clear due to excessive flaring of the abrasive jet. In view of this all tests have been carried out upto a stand-off distance of 20 mm. For ease in measuring the cavity diameter and depth, each test was carried out for 60 seconds. The volume of material eroded, the cavity top diameter and eroded depth at the centre have been evaluated by projecting the eroded cavity on the screen of a measuring projector.



Nozzle wear tests have been performed on high carbon high chromium tool steel nozzles of convergent-straight geometry (Fig. 4.4a). Experiments have been carried out to ascertain the wear rate of nozzle as well as wear profile. For this purpose a set of split nozzles were used. These nozzles were made in two halves and assembled together to get the final profile. The nozzles were disassembled after use and the inside surface was examined under a profile projector to obtain the wear profile. During preliminary experiments, the nozzle profiles were traced after three minutes intervals. Nozzle wear profiles obtained after various operating times are shown in Fig. 4.4 (b-e). It is clear that the profile of the worn out nozzle closely resembles a truncated cone. The wear volume in all subsequent experiments was, therefore, calculated on the basis of the inlet and exit diameters of the flow channel by assuming a straight flare from the entry to the exit side. The wear volume was also obtained by weighing the nozzle before and after the use. The wear volumes thus obtained are plotted in Fig. 4.5. The wear volumes evaluated on the basis of the inlet and exit diameters of the nozzle flow channel are also plotted in this figure. It is clear that both the results closely match.

Nozzle wear profiles shown in Fig. 4.4(b-e) clearly indicate that the exit diameter of the nozzle flow channel becomes almost 1.3 times the initial exit diameter in approximately 20 minutes. Also the assumption that the wear profile resembles a truncated cone does not appear to be valid after 15 minutes of use. All subsequent experiments were, therefore, carried out upto 15 minutes only. Further, the time interval for recording of successive wear profile was also reduced to 2.5 minutes.

#### 4.5 Experimental Conditions

After obtaining satisfactory results in the preliminary experiments, erosion rate and nozzle wear experiments have been carried out under the following experimental conditions :

##### Nozzle

Material : Tungsten carbide and high carbon high chromium tool steel (2.15% C, 12% Cr, 0.35% Mn, 0.2% Si, 0.8% Mo);

Diameter : 0.712, 0.78, 0.8, 0.9, 0.96, 0.97, 1.17  
and 1.62 mm.

### Carrier Fluid

Carrier gas : Dry air ;

Inlet pressure: 344.863 to 372.453 kN/m<sup>2</sup> (gauge);

Nozzle pressure: 98.1 to 294.3 kN/m<sup>2</sup> (gauge).

### Abrasive

Type : Aluminium oxide;

Size : 25, 30, 38 and 48  $\mu\text{m}$ ;

Mixture ratio : 0.052 to 0.308.

### Vibrator characteristics

Amplitude : 1.9 mm;

Frequency : 5 to 8 c/sec.

Work Material : Glass.

## 4.6 Experimental Results

Experiments have been conducted to investigate the effects of various input parameters on volumetric erosion rate, penetration rate, top diameter of eroded cavity etc. and on wear of nozzle of various geometries. Experiments have been carried out over the range of experimental conditions stated earlier. All erosion tests have been carried out at system inlet pressure of 344.863 kN/m<sup>2</sup> (gauge) while nozzle wear tests have been conducted at system inlet pressure

of  $372.453 \text{ kN/m}^2$  (gauge). The effect of stand-off distance, mixture ratio, abrasive particle size, nozzle pressure etc. on volumetric material removal rate, penetration rate, top diameter of eroded cavity are shown in Figures 4.6 to 4.14 while wear results obtained with nozzles of various sizes are plotted in Figures 4.15 to 4.23.

#### 4.6.1 Erosion

The effects of stand-off distance on volumetric material removal rate and penetration rate are shown in Fig. 4.6. The profiles of the machined cavity at several stand-off distances are also indicated. Figure shows that both material removal rate and penetration rate first increase with increase in stand-off distance and then decrease giving an optimum value. The maxima of the penetration rate and the volumetric material removal rate do not occur at the same stand-off distance for the specified machining condition. Figure further shows that the maximum penetration rate occurs at smaller stand-off distance than the value where maximum material removal rate is obtained. Photographs of the machined cavity at different stand-off distances are shown in Fig. 4.7.

Volumetric material removal rate not only depends on stand-off distance but also depends on the mixture ratio. Fig. 4.8 shows the variation of volumetric material removal

rate with stand-off distance for different mixture ratios. It shows that the optimum stand-off distance at which material removal rate is maximum does not change much with variation in mixture ratio.

The variation in penetration rate with stand-off distance for different mixture ratios (Fig. 4.9) indicates that the penetration rate increases with increase in mixture ratio. The stand-off distance corresponding to the maximum penetration rate also increases with increase in mixture ratio.

The top diameter of the eroded cavity also varies with stand-off distance and mixture ratio as indicated in Fig. 4.10. It is clear that the top diameter of the eroded cavity increases with increase in mixture ratio and stand-off distance but tends to saturate beyond a certain stand-off distance. For low mixture ratio the saturation tends to occur at smaller stand-off distance than for high mixture ratio.

The erosion rate is very much dependent on mixture ratio and particle size. To have a comparative effect of abrasive particle size on volumetric erosion rate, the volume erosion factor  $\epsilon_v$  was employed. This is defined as,

$$\epsilon_v = \frac{\text{Volumetric material removal rate (mm}^3/\text{min)}}{\text{Weight of abrasive particle impacted per unit time (g/min)}} \quad (4.1)$$

Fig. 4.11 shows the variation in this erosion factor  $\epsilon_v$  with stand-off distance for different grain sizes. It shows that the volume erosion factor increases with increase in stand-off distance and then falls with further increase giving an optimum value. Further, this optimum stand-off distance does not appear to vary when grain size is varied. The coarse grains, however, give higher values of erosion factor  $\epsilon_v$ .

The variation in optimum material removal rate with mixture ratio for different grain sizes (Fig. 4.12) indicates a linear increase in material removal rate upto a certain value of mixture ratio and then tends to fall. Again coarser grains give higher value of volumetric material removal rate while finer particles have larger linearity range.

Fig. 4.13 indicates the effects of grain size on penetration rate. It is clear that coarse particles give higher penetration rate. The stand-off distance where maximum penetration rate is achieved, however, shows only marginal effect of grain size.

The effect of nozzle pressure on volumetric material removal rate is shown in Fig. 4.14. The rate of increase of material removal rate appears to decrease with increasing nozzle pressure and has a tendency to saturate beyond a certain value of nozzle pressure. Further, the material removal rate curves for different mixture ratios appear to intersect the nozzle pressure axis at around 55 kN/m<sup>2</sup>(gauge).

#### 4.6.2 Nozzle Wear

Nozzle wear profiles for split nozzles of specified geometry (Fig. 4.4) show that the wear in the convergent region of the nozzle is negligibly small compared to the straight region of the nozzle flow channel. The diameters of nozzle flow channel were measured along the length and diametral wear rates were evaluated. The diametral wear rate  $W_d$  can now be defined as,

$$W_d = \frac{\text{final diameter of nozzle flow channel (mm)} - \text{previous diameter of nozzle flow channel (mm)}}{\text{time (sec)}} .$$

(4.2)

Variation of the diametral wear rate at different nozzle sections of straight region of the nozzle flow channel for different operating times are shown in Fig. 4.15. Figure shows that the diametral wear rate decreases with the increase

in operating time. It is further shown that the wear rate increases from the inlet towards the exit giving a maximum at the exit.

The nozzle wear when expressed in terms of wear volume is thus a function of length and diameter of the nozzle. These parameters influence not only the wear volume but also the wear rate since they affect the flow pattern of the particles inside the nozzle. In order to study the effect of the nozzle parameters on the wear rate, nozzle wear has been plotted in terms of the dimensionless wear index  $W^*$  which is defined as,

$$W^* = \frac{\text{final volume of nozzle flow channel (mm}^3\text{)} - \text{initial volume of nozzle flow channel (mm}^3\text{)}}{\text{initial volume of nozzle flow channel (mm}^3\text{)}} \quad (4.3)$$

The wear index is plotted as a function of operating time for nozzles of various lengths in Fig. 4.16. The shape of the curve is similar for various nozzle lengths and indicates that the wear index initially increases linearly and then saturates at a specific value of operating time. As expected the wear index increases with increasing nozzle length (Fig. 4.17).



The variation of wear index with operating time for various nozzle diameters is shown in Fig. 4.18. The wear index for a specific operating time decreases appreciably when the nozzle diameter is increased (Fig. 4.19).

Fig. 4.20 shows the variation of the wear index with operating time for various nozzle entrance angles. The initial wear rate (slope of the wear index curve) is again high but tends to saturate rapidly. The wear rate increases with decreasing nozzle entrance angle.

Fig. 4.21 shows the variation of the wear index with operating time for various mixture ratios. The wear index initially increases linearly with operating time but saturates after a specific operating time. The wear index increases linearly with increasing mixture ratio but the slope of the curve also increases with increase in operating time (Fig. 4.22).

The effect of grain size on wear index is shown in Fig. 4.23. Tests with particles of grain sizes 30 and 38  $\mu\text{m}$  indicate that increased wear index is obtained with coarse grains.



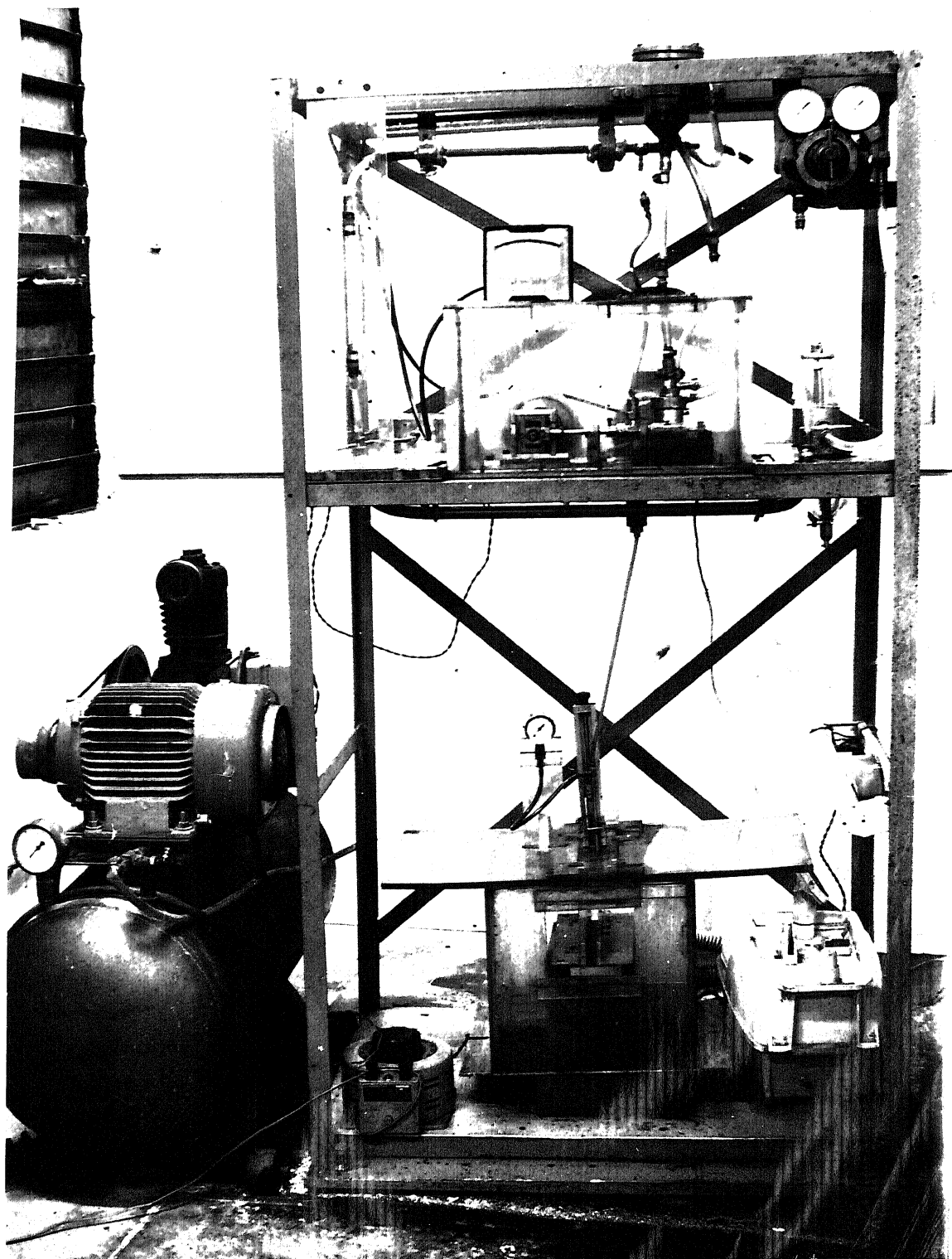


Fig. 4.2 (a) Experimental set-up of abrasive jet machining.

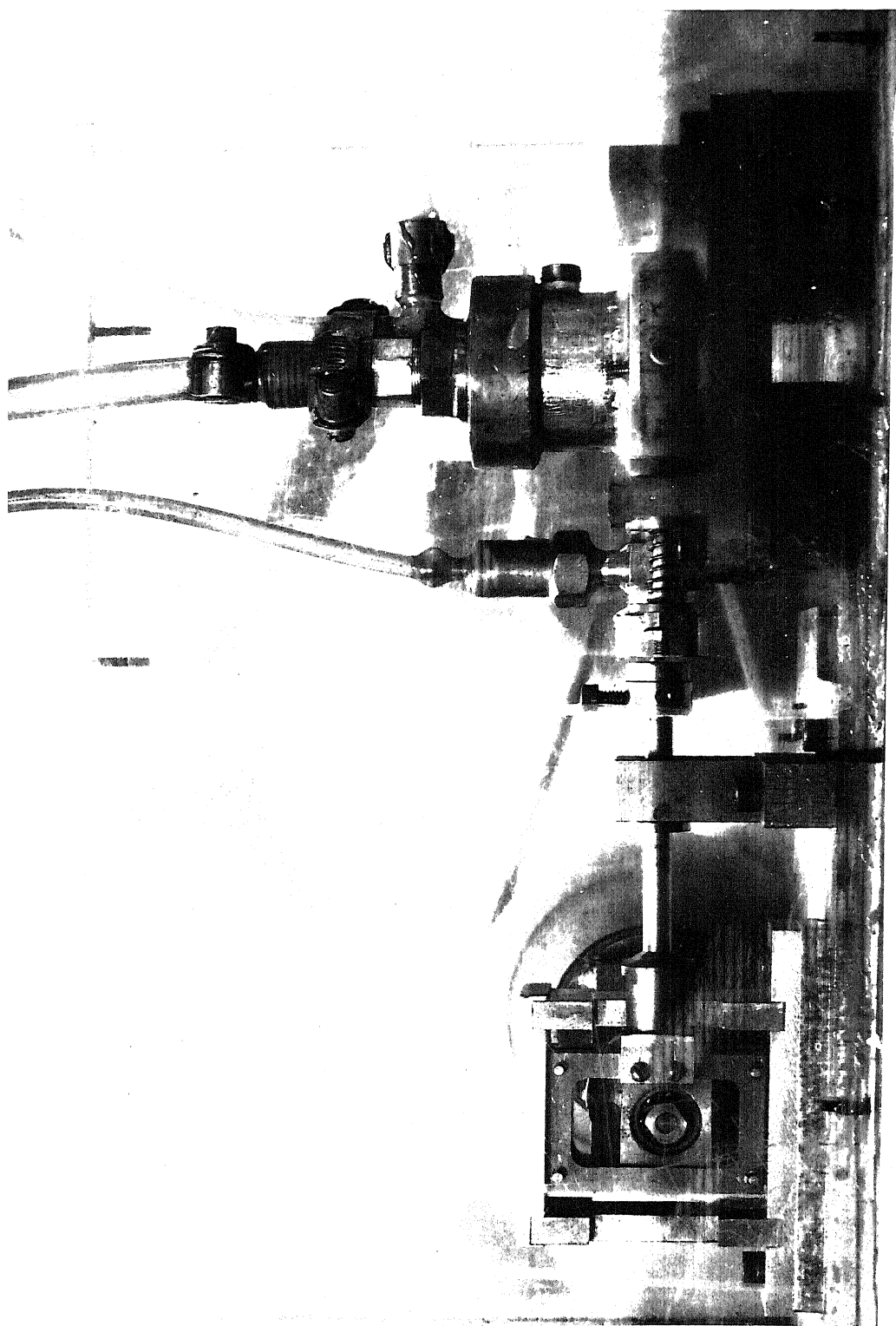


Fig. 4.2 (a) Photograph of mixing chamber, secondary chamber and vibrator unit .

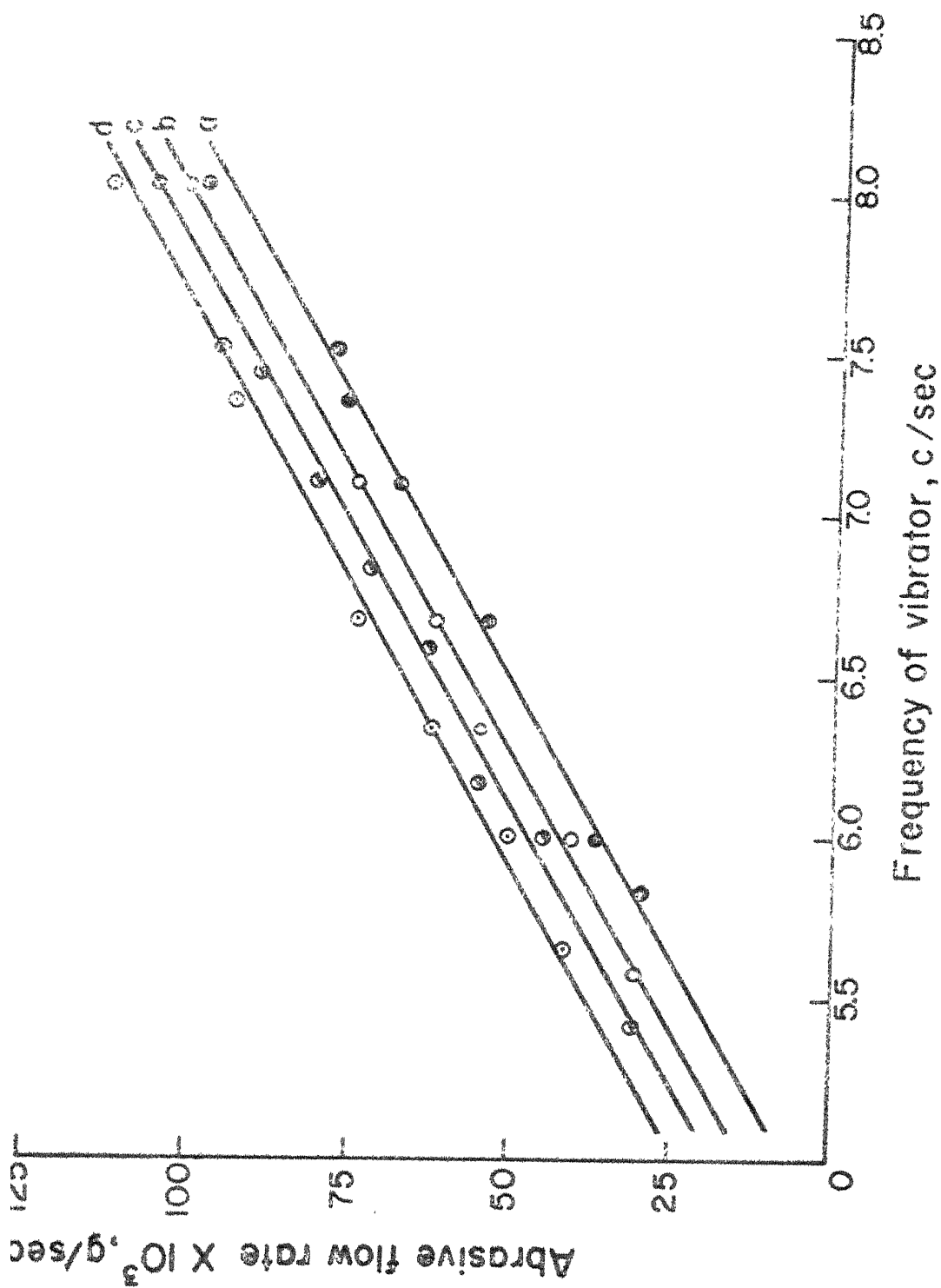


Fig.4.3 Calibration curves of abrasive flow rate for different particle sizes (a) 25  $\mu\text{m}$ , (b) 30  $\mu\text{m}$ , (c) 38  $\mu\text{m}$  and (d) 48  $\mu\text{m}$ .

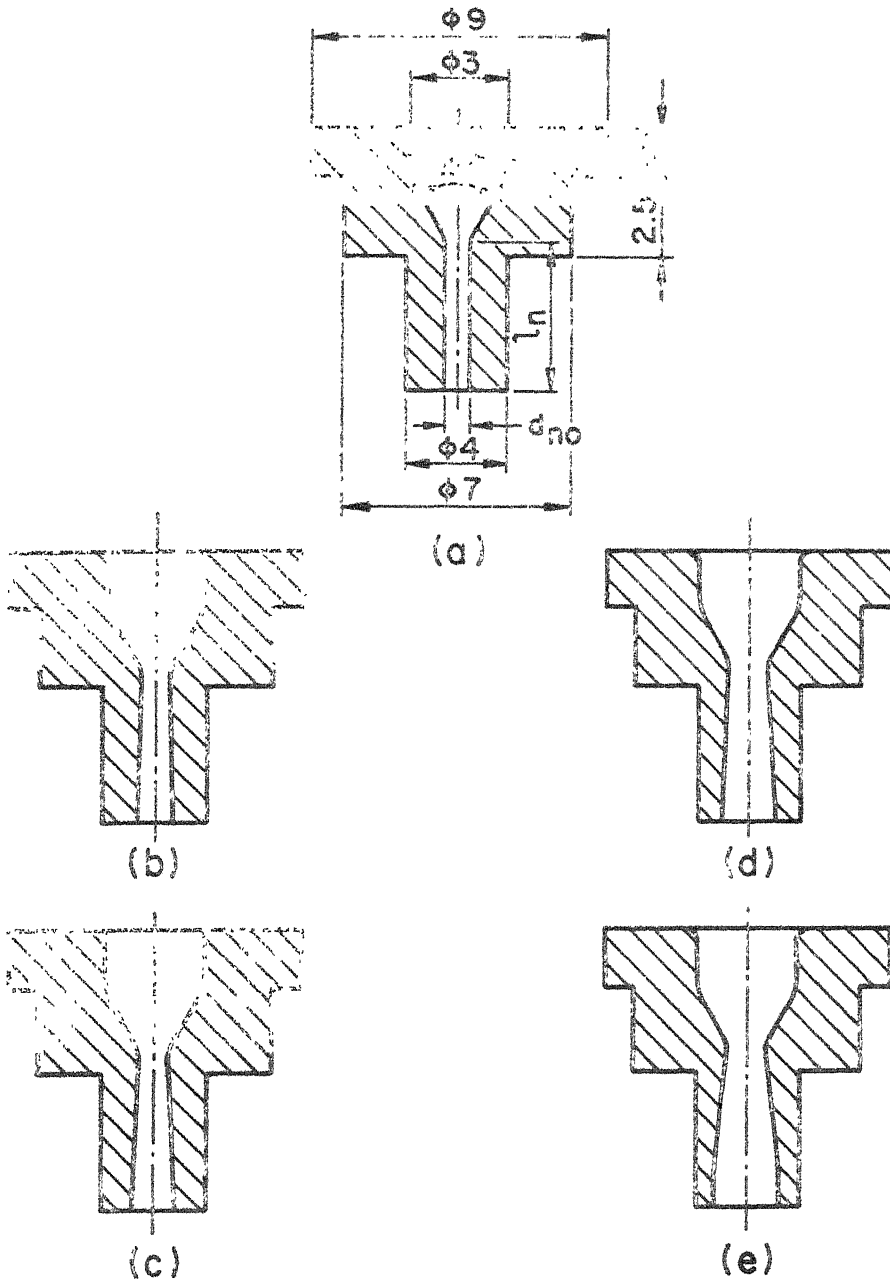


Fig.4.4 Nozzle wear profiles (a) initial profile, (b) after 5 min, (c) after 10 min, (d) after 15 min and (e) after 20 min. Hardness : 50 HRc ;  $d_{no} : 0.78 \text{ mm}$  ;  $l_n : 4.5 \text{ mm}$  ;  $\beta : 30^\circ$  ;  $d_p : 38 \mu\text{m}$  ;  $\alpha : 0.201$ .

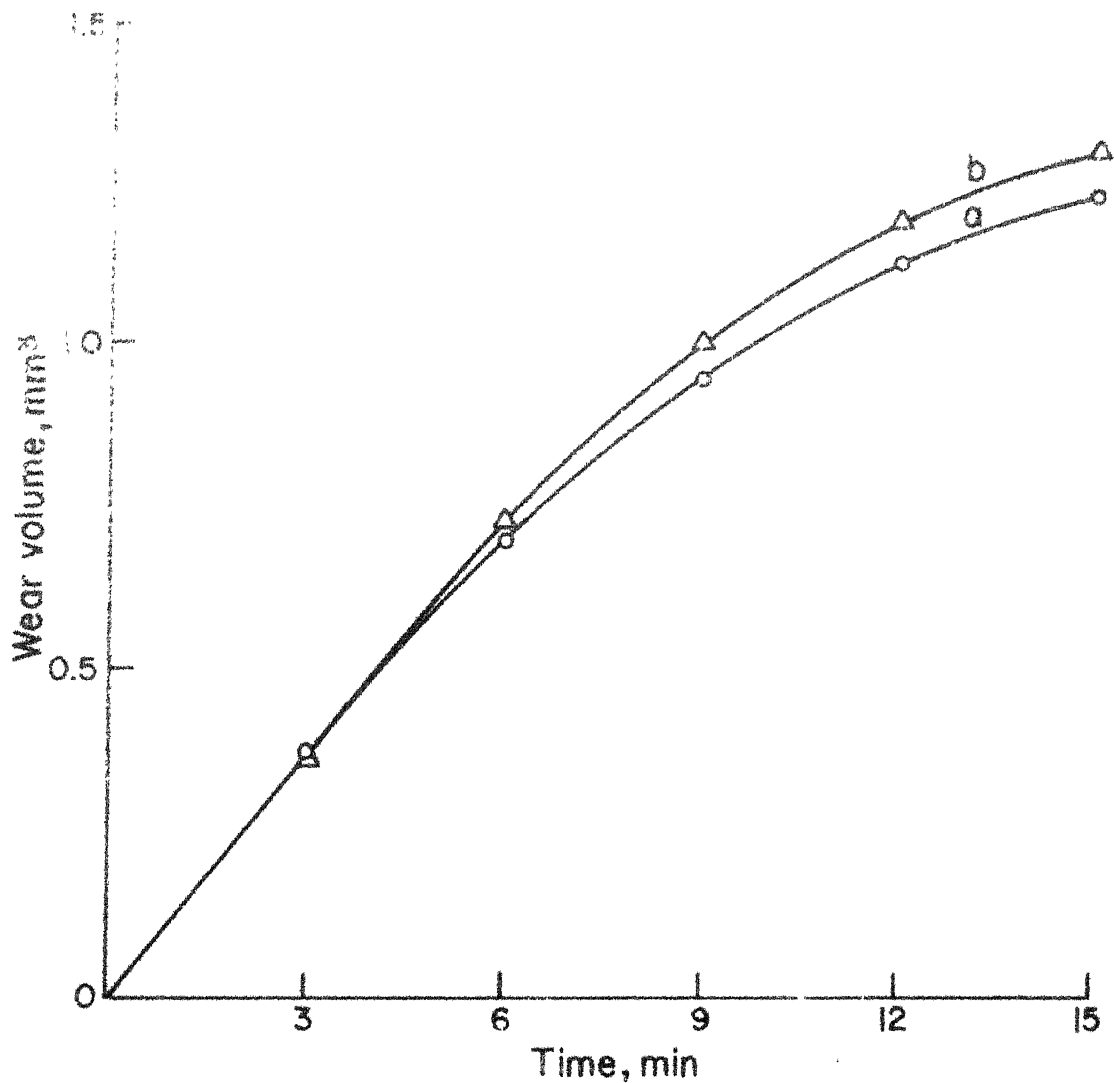


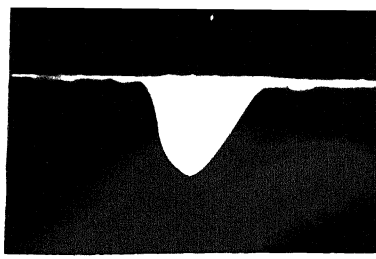
Fig. 4.5 Variation of nozzle wear volume with operating time  
 (a) wear volume from inlet and exit diameters and  
 (b) wear volume from difference of weight.  
 Hardness: 10HRc;  $d_{n0}$ : 0.78 mm;  $l_n$ : 6.35 mm;  $\beta$ :  $30^\circ$ ;  
 $d_p$ : 30  $\mu$ m;  $\alpha$ : 0.154.



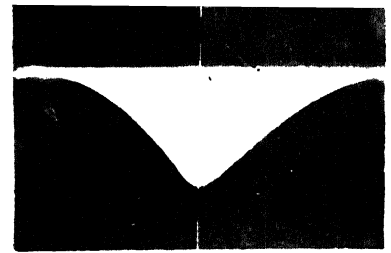
The following table shows the results of the experiment. The first column shows the time in minutes, the second column shows the distance in mm, and the third column shows the velocity in mm/min. The data points are labeled with numbers 1 through 10.

Time (min)	Distance (mm)	Velocity (mm/min)
1.5	2.5	1.67
3.5	4.5	1.29
5.5	6.5	1.11
7.5	8.5	1.13
9.5	10.0	1.05

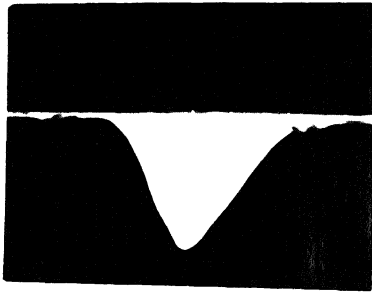




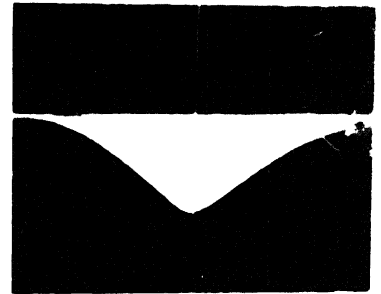
(a)



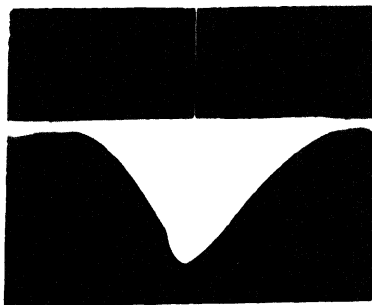
(d)



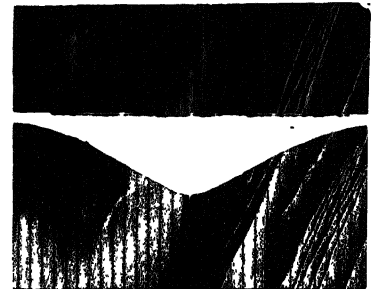
(b)



(e)



(c)



(f)

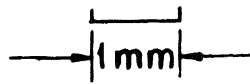


Fig.4.7 Machined cavity profile at different stand-off distances (a) 2mm, (b) 6mm, (c) 10mm, (d) 14 mm, (e) 16 mm and (f) 20 mm.  $d_p : 30 \mu\text{m}$  ;  $\alpha : 0.148$  ; nozzle pressure :  $147.15 \text{ kN/m}^2$  (gauge) ; cutting time : 60 sec.

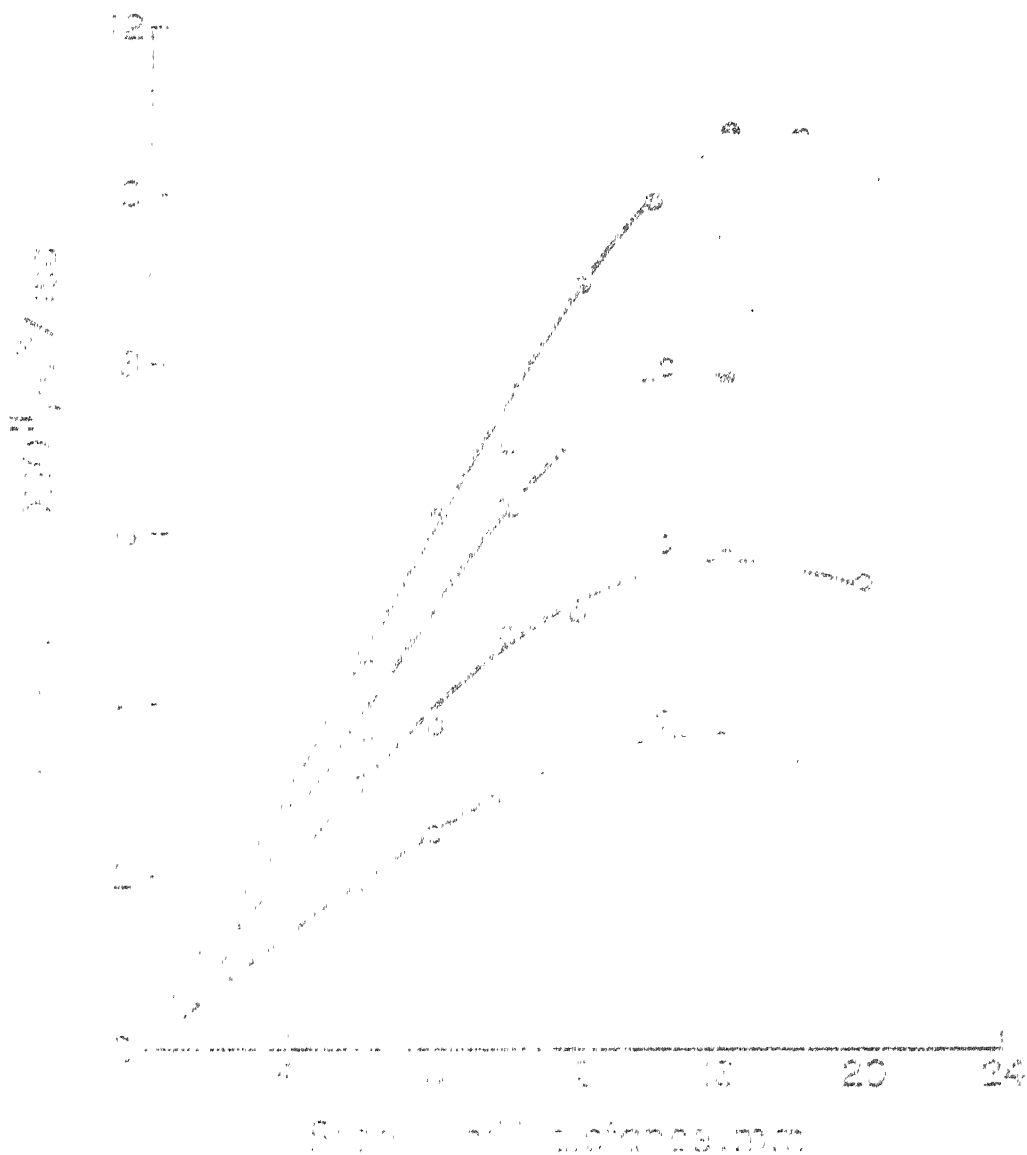


Fig. 1. Relationship of material removal rate with stand-off distance for different  $r/h$  ratios (a) 0.095, (b) 0.145 (c) 0.195 and (d) 0.260;  $d_p = 30 \mu\text{m}$ ;  $\text{stand-off distance} = 0.47 \text{ mm}$  (gauge).



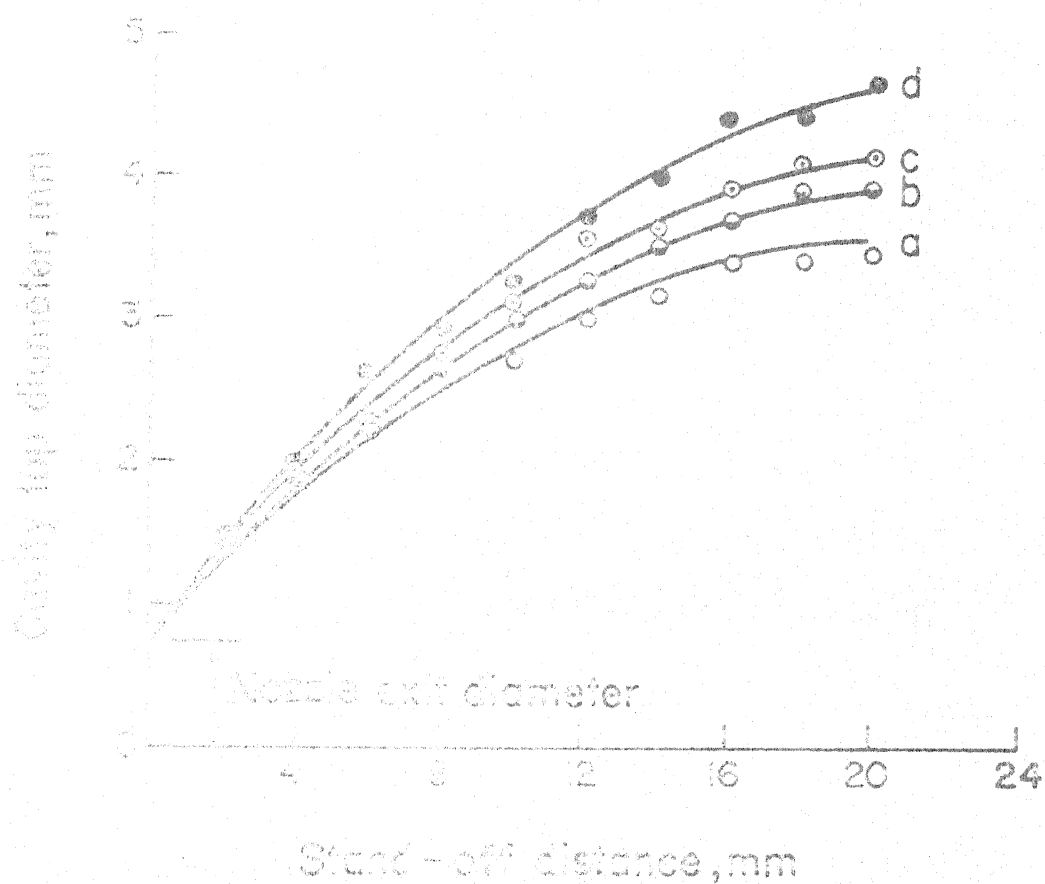


Fig. 4.10 Variation of top diameter of the machined cavity with stand-off distance for different mixture ratios (a) 0.095, (b) 0.148, (c) 0.201 and (d) 0.268.  $d_p = 30 \mu\text{m}$ ; nozzle pressure:  $147.15 \text{ kN/m}^2$  (gauge).

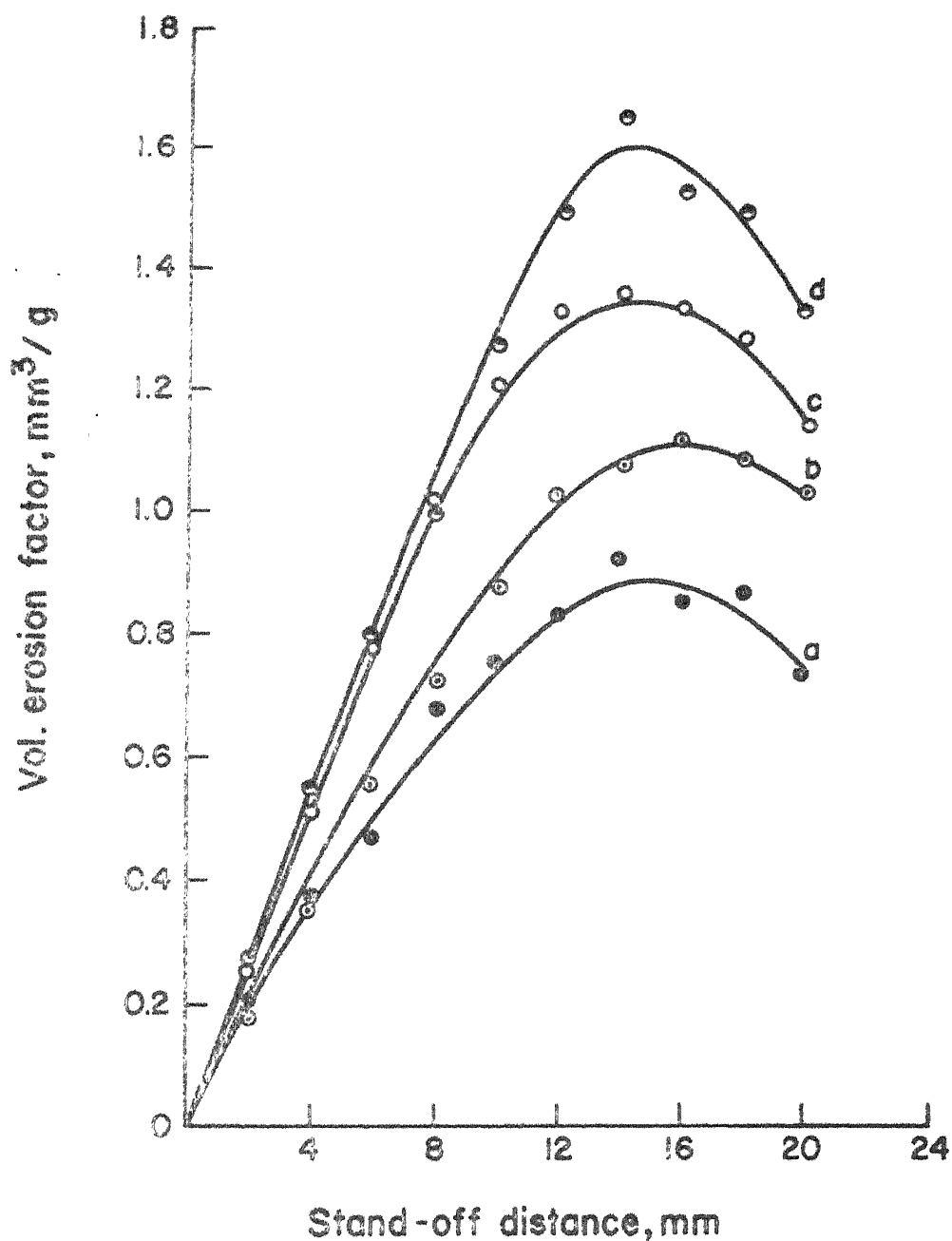


Fig. 4.11 Variation of volume erosion factor with stand-off distance for different particle sizes (a) 25  $\mu\text{m}$ , (b) 30  $\mu\text{m}$ , (c) 38  $\mu\text{m}$  and (d) 48  $\mu\text{m}$ . Nozzle pressure: 147.15 kN/m<sup>2</sup> (gauge).

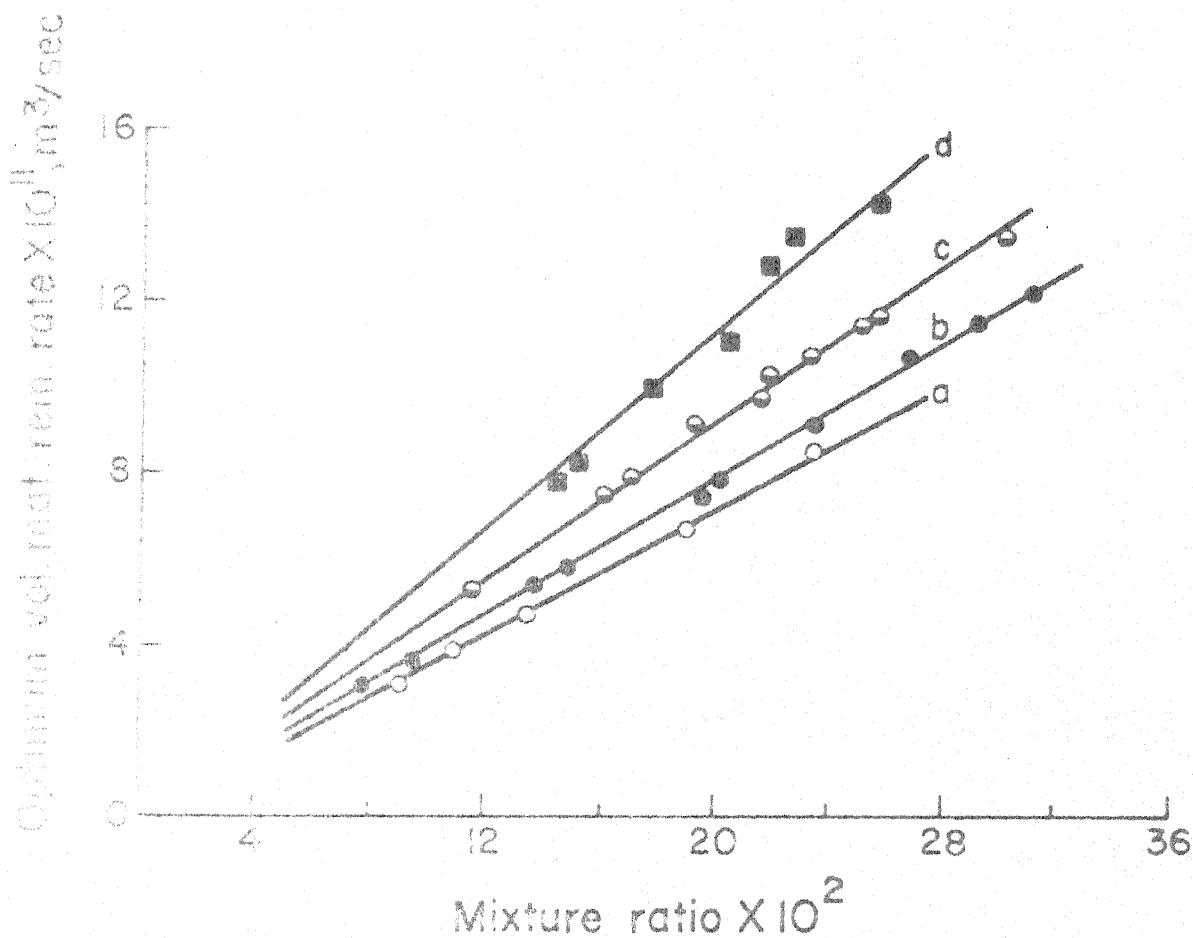


Fig. 4.12. Variation of optimum material removal rate with mixture ratio for different particle sizes (a) 25  $\mu\text{m}$ , (b) 30  $\mu\text{m}$ , (c) 38  $\mu\text{m}$  and (d) 48  $\mu\text{m}$ . Nozzle pressure: 147.15  $\text{kN/m}^2$  (gauge), stand-off distance: 16 mm.

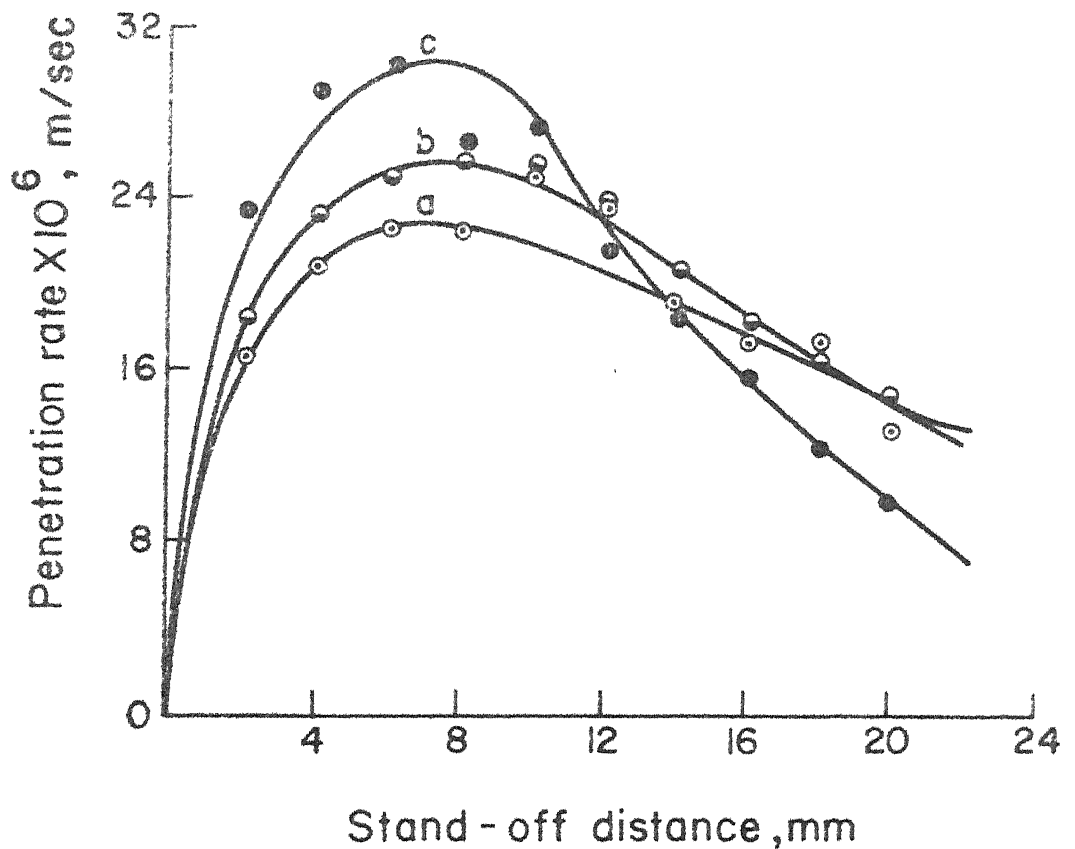


Fig. 4.13 Variation of penetration rate with stand-off distance for different particle sizes (a) 25  $\mu\text{m}$ , (b) 30  $\mu\text{m}$  and (c) 48  $\mu\text{m}$ .  $\alpha$ : 0.148; nozzle pressure: 147.15 kN/m<sup>2</sup>(gauge).

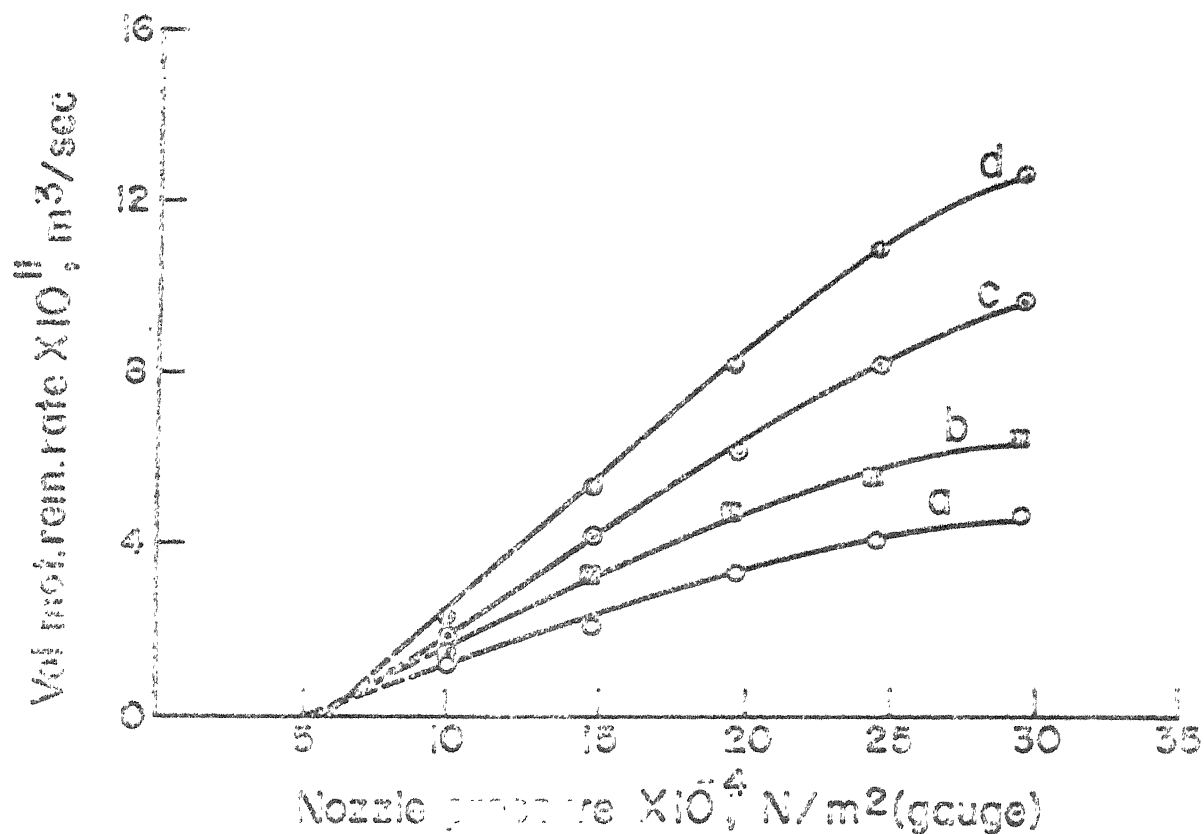


Fig. 4.14 Variation of material removal rate with nozzle pressure for different mixture ratios (a) 0.052, (b) 0.088, (c) 0.109 and (d) 0.143.  $d_p$ : 30  $\mu$ m; stand-off distance: 16 mm.



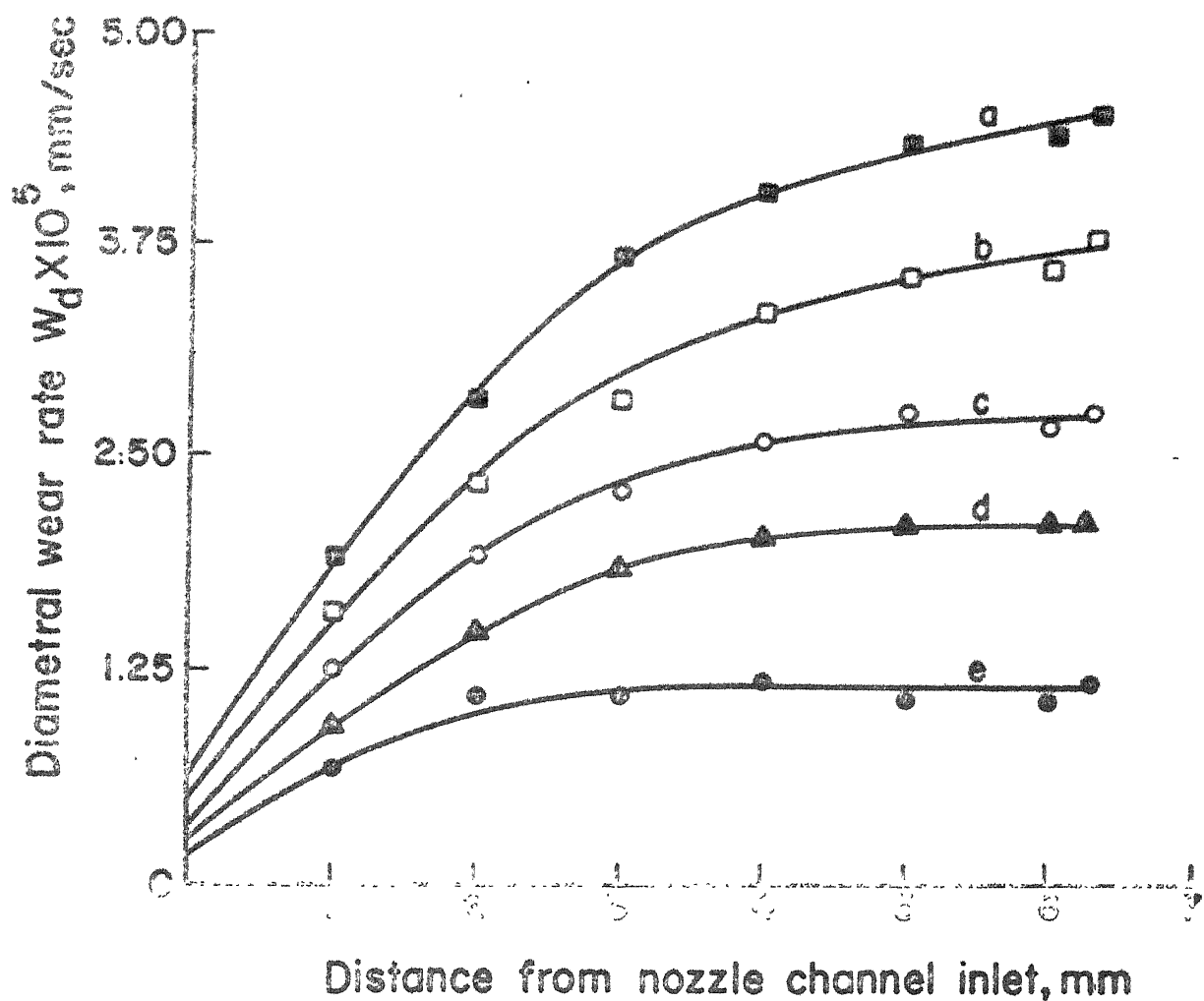


Fig.4.15. Variation of diametral wear rate with nozzle length for different operating times (a) 6 min, (b) 9 min, (c) 12 min, (d) 15 min and (e) 18 min. Hardness: 10 HRC;  $d_{no}$ : 0.78 mm;  $l_n$ : 6.3 mm;  $\beta$ :  $30^\circ$ ;  $d_p$ : 30  $\mu$ m;  $\alpha$ : 0.154.

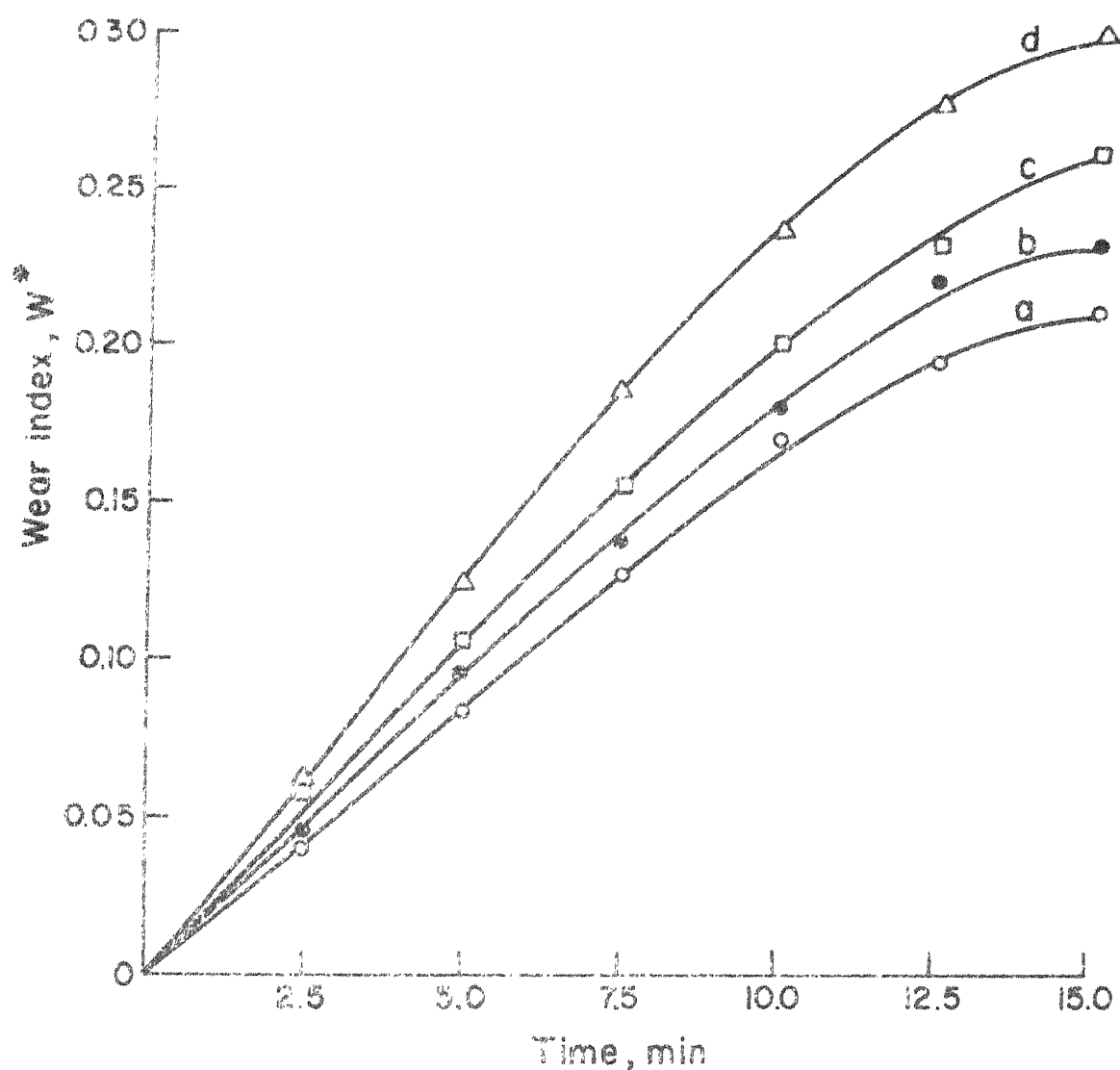


Fig. 4.16 Variation of the wear index with the operating time for different nozzle length to exit diameter ratios (a) 8.41, (b) 10.47, (c) 12.88 and (d) 16.68. Hardness 50 HRc;  $d_{no}$ : 0.97 mm;  $\beta$ :  $30^\circ$ ;  $d_p$ :  $38 \mu\text{m}$ ;  $\alpha = 0.201$ .

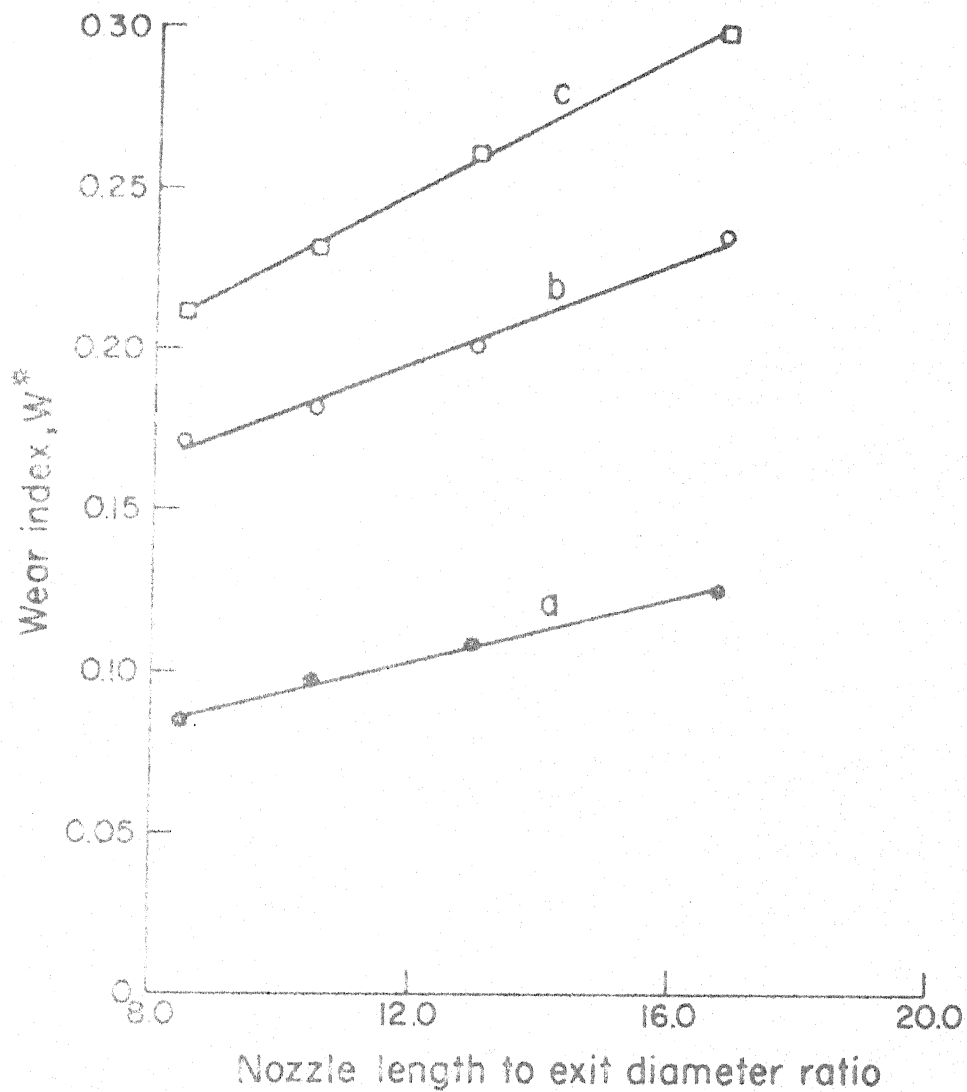


Fig. 4.17 Variation of the wear index with the nozzle length to exit diameter ratio for different operating times (a) 5 min, (b) 10 min and (c) 15 min. Hardness: 50 HRc;  $d_{no}$ : 0.97 mm;  $\beta$ :  $30^\circ$ ;  $d_p$ : 38  $\mu$ m;  $\alpha$ : 0.201.

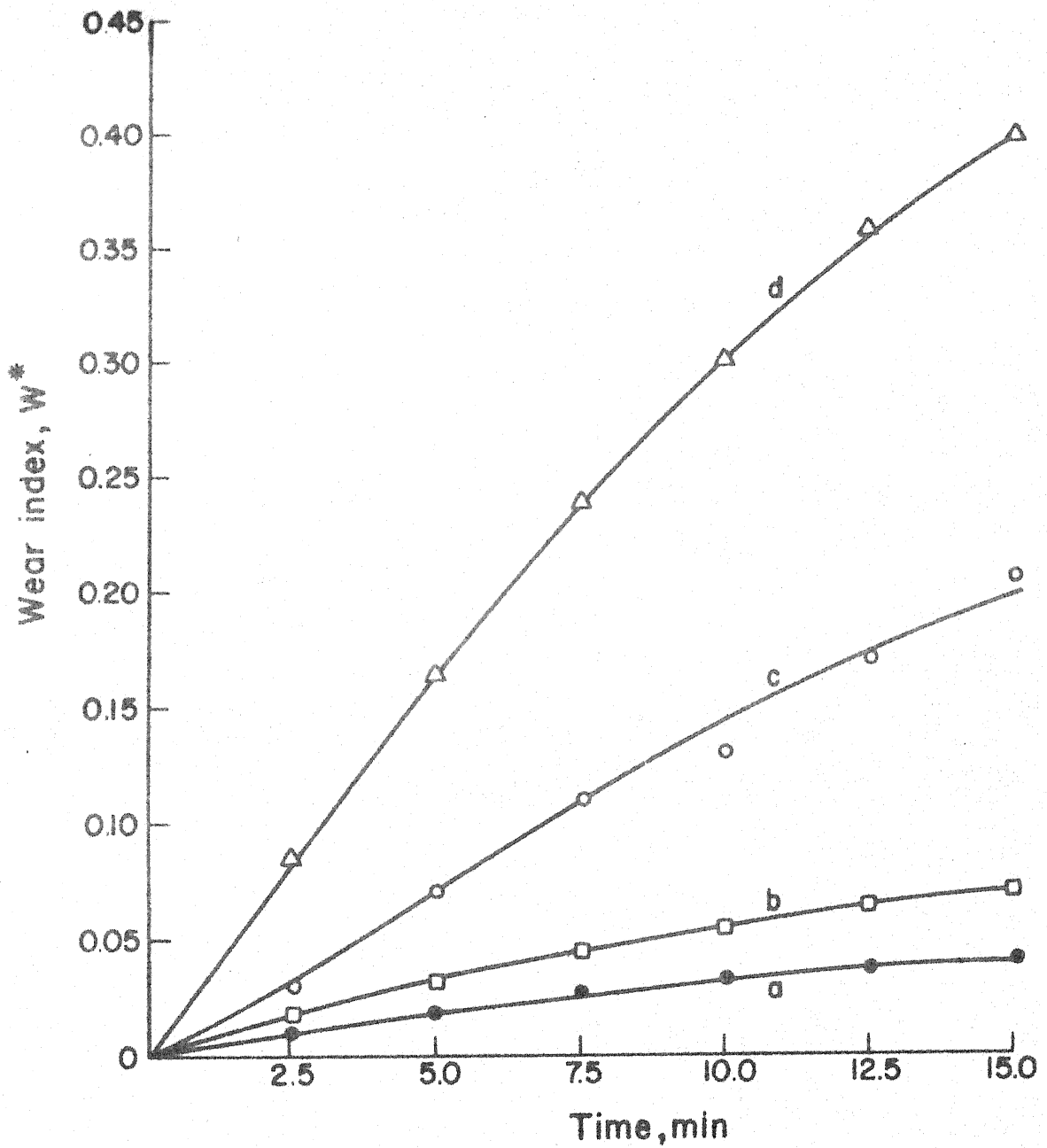


Fig. 4.18 Variation of the wear index with the operating time for different nozzle exit diameters (a) 1.62 mm, (b) 1.17 mm, (c) 0.9 mm and (d) 0.8 mm. Hardness: 50 HRC;  $l_n$ : 12 mm;  $\beta$ :  $30^\circ$ ;  $d_p$ : 38  $\mu$ m;  $\alpha$ : 0.201.

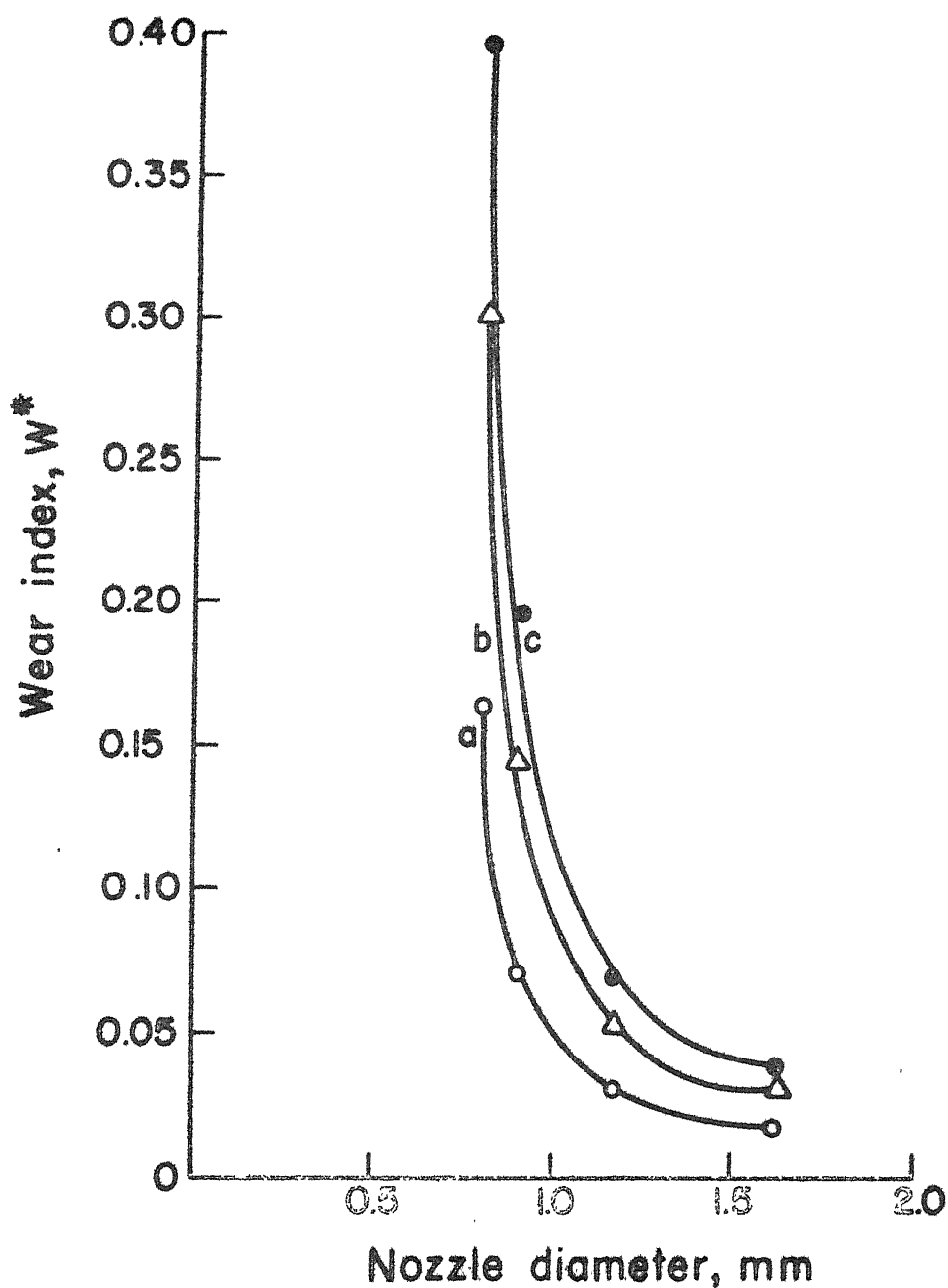


Fig.4.19 Variation of the wear index with the nozzle diameter for different operating times (a) 5 min, (b) 10 min and (c) 15 min. Hardness : 50 HRc ;  $l_n$  : 12 mm ;  $\beta$  :  $30^\circ$  ;  $d_p$  :  $38 \mu\text{m}$  ;  $\alpha$  : 0.20 l .

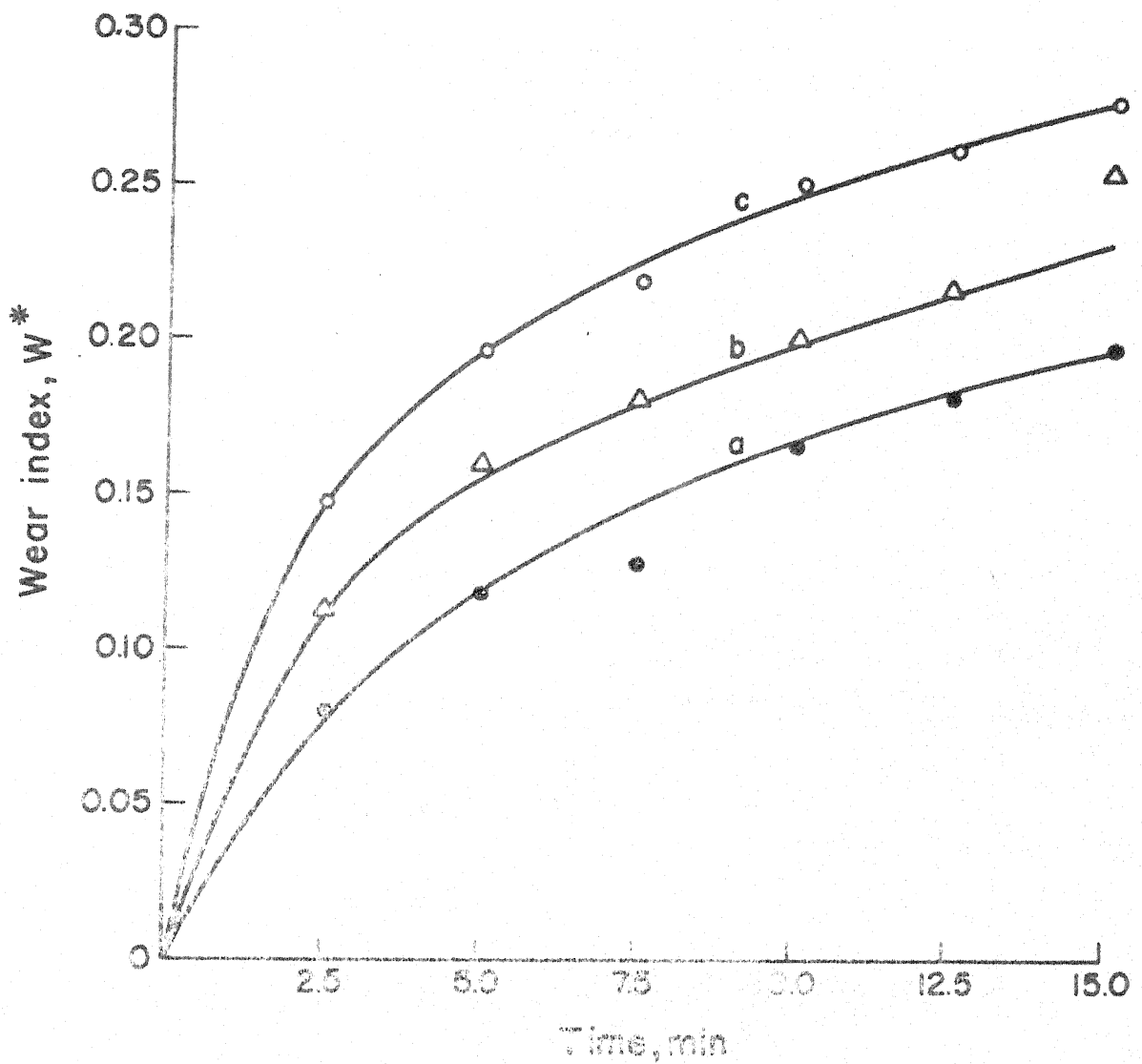


Fig. 4.20 Variation of the wear index with the operating time for different entrance angles (a)  $20^\circ$ , (b)  $90^\circ$  and (c)  $60^\circ$ . Hardness : 50 HRC ;  $d_{p0}$  : 0.96 mm ;  $l_1$  : 5.28 mm ;  $d_p$  : 36  $\mu$ m ;  $\alpha$  : 0.20.

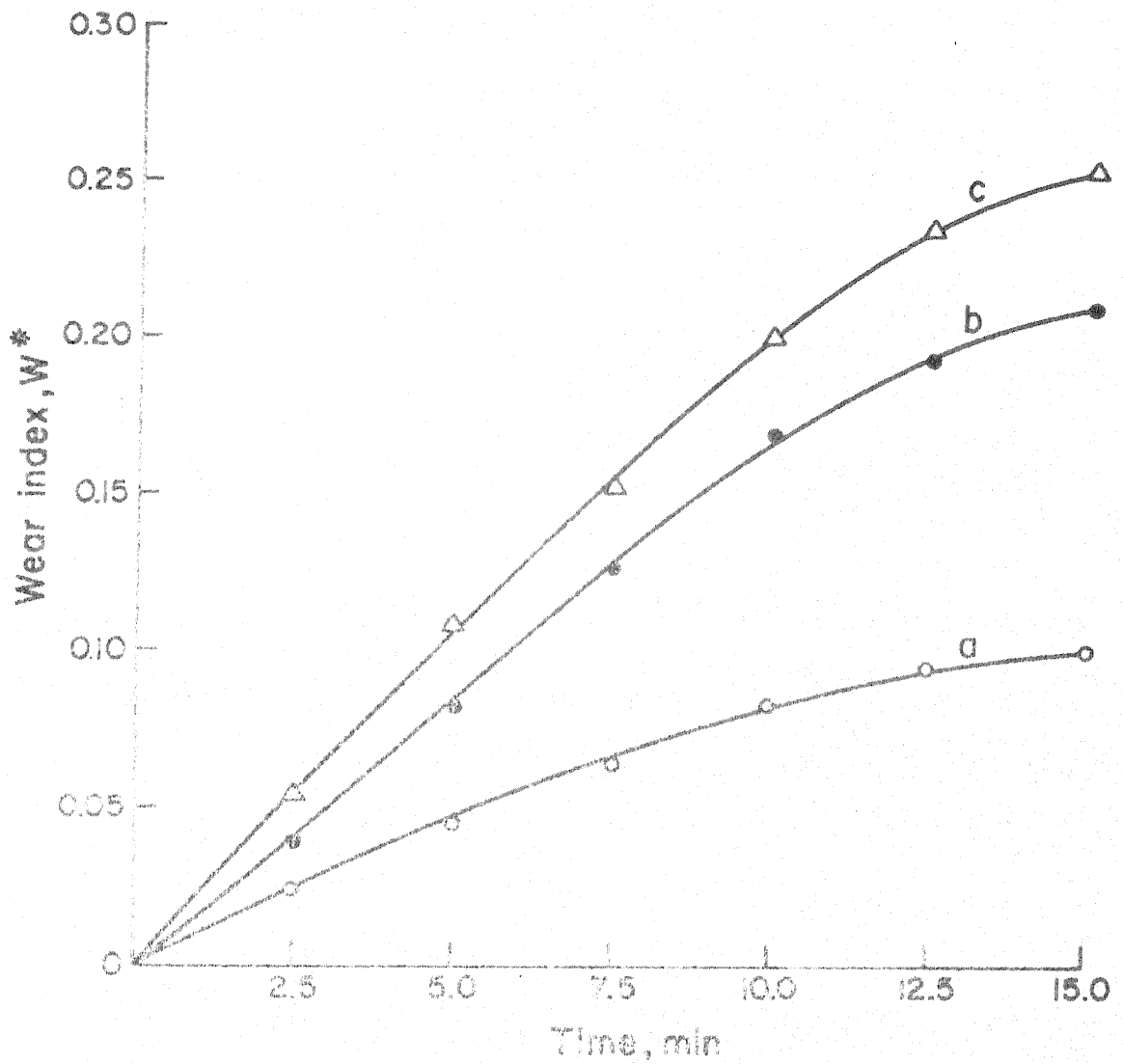


Fig.4.21 Variation of the wear index with the operating time for different mixture ratios (a) 0.096, (b) 0.088, (c) 0.201 and (d) 0.249. Hardness: 50 HRc;  $d_{n0}$ : 0.97 mm;  $l_n$ : 8.16 mm;  $\phi$ :  $30^\circ$ ;  $d_p$ : 38  $\mu$ m.

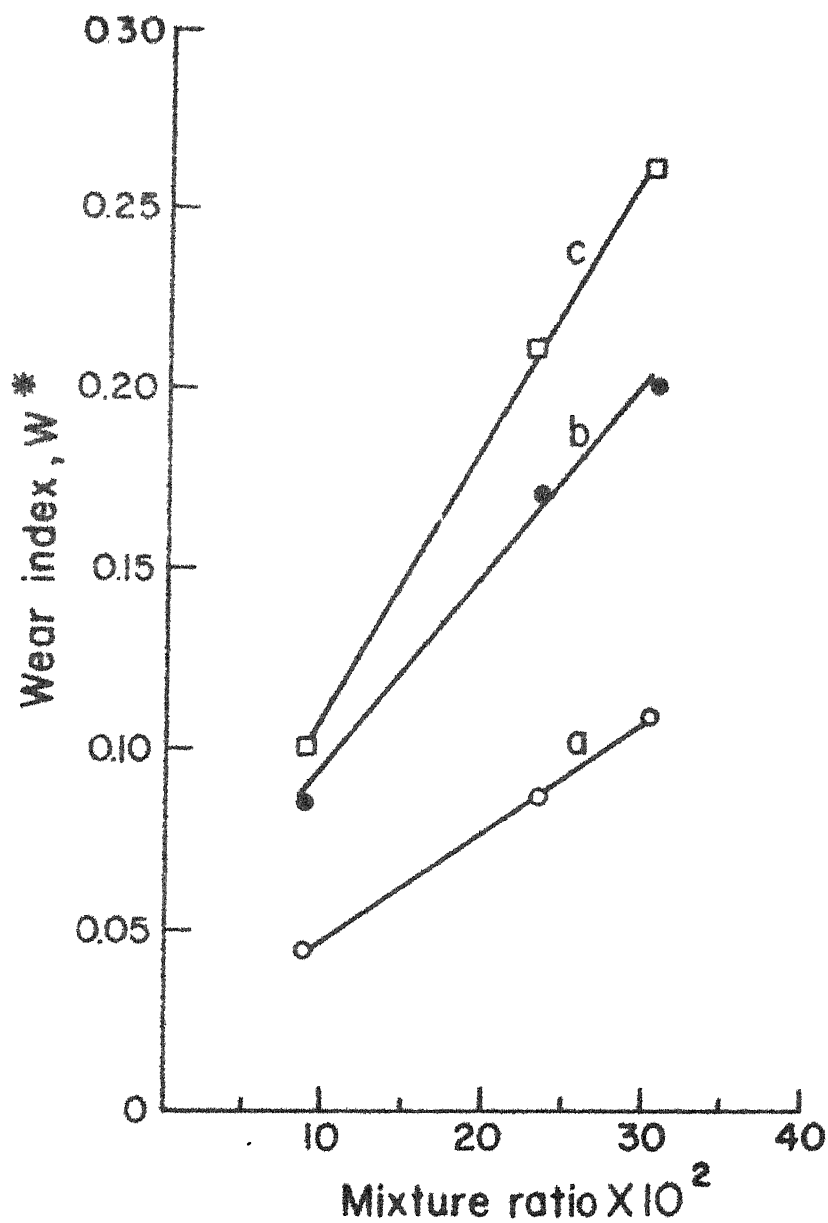


Fig.4.22 Variation of the wear index with the mixture ratio for different operating times (a) 5 min, (b) 10 min and (c) 15 min. Hardness: 50 HRc;  $d_{n0}$ : 0.97 mm;  $l_n$ : 8.16 mm;  $\beta$ :  $30^\circ$ ;  $d_p$ : 38  $\mu$ m.



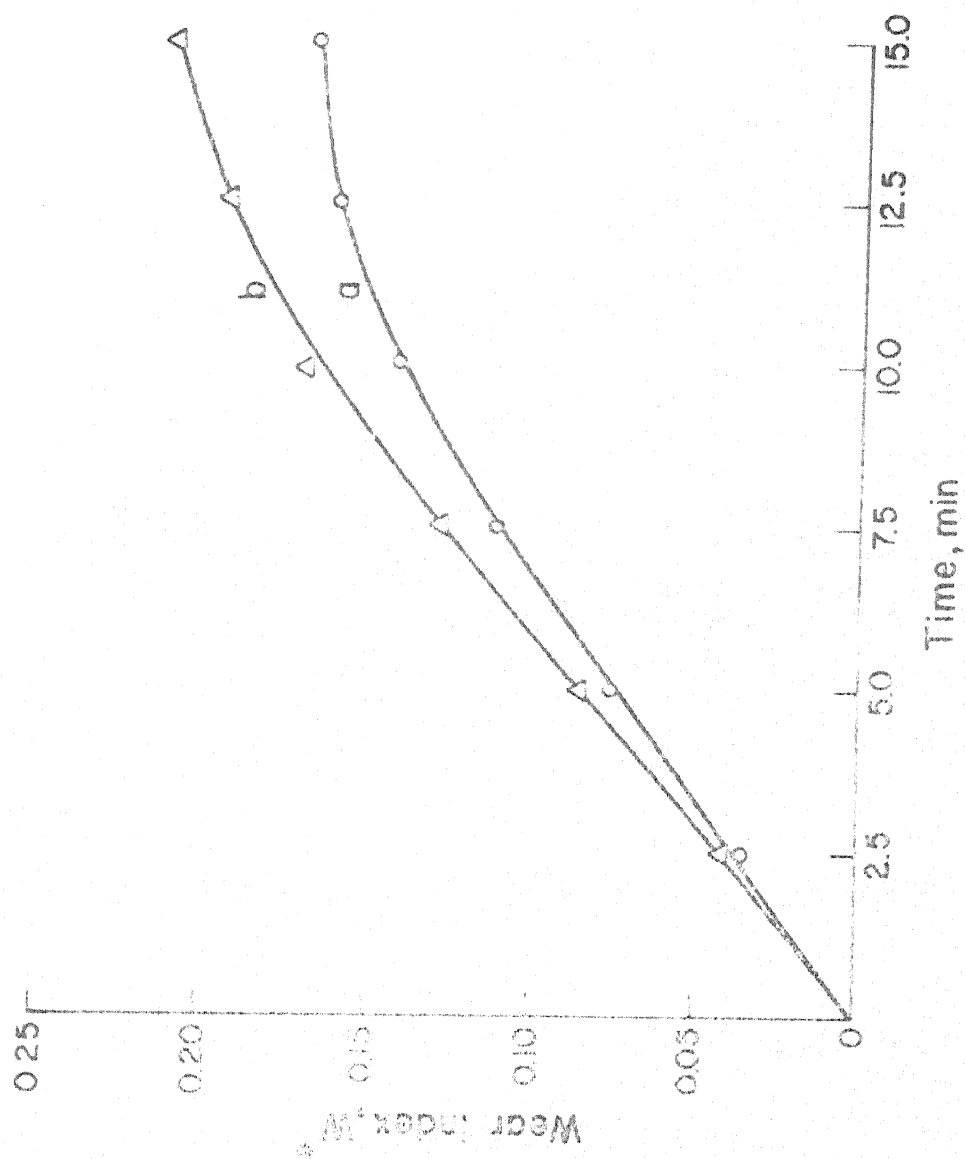


Fig. 4.23 Variation of the wear index with the operating time for different particle sizes (a) 30  $\mu\text{m}$  and (b) 38  $\mu\text{m}$ . Hardness: 50 HRC;  $d_{\text{no}}$ : 0.97 mm;  $l_n$ : 8.16 mm;  $\beta$ : 30°;  $\alpha$ : 0.201.

## CHAPTER 5

### DISCUSSION

#### 5.1 Erosion

As mentioned earlier, material removal in AJM occurs due to erosive action of abrasive particles impacting at high velocity onto the work surface. The mechanics of material removal in such situations is quite complex and difficult to analyse because of many unknown and interdependent parameters. From one-dimensional steady state two-phase flow analysis presented in Chapter 2 the velocity of impacting particle can be estimated. Considering quasi-static indentation under elastic-plastic response of target material and using semi-empirical fracture mechanics relationships a theoretical model of erosion rate for brittle materials such as glass, ceramics etc. has been developed in Chapter 3.

Equation (3.40) shows that beside material parameters, the erosion rate in brittle materials under solid particle impact is a strong function of the velocity of impacting particle. In most of the earlier investigations [25,46,50, 63, 75 ], the emphasis was put on the velocity exponent controlling the erosion rate in brittle materials. In the

present theory, the velocity exponent of 2.75 has been obtained. Earlier Weiderhorn and Hockey [75] and Sheldon and Finnie [46] experimentally obtained the velocity exponent values as 2.5 and 3, respectively for erosion of glass. Other brittle erosion theories [25, 63] give the velocity exponent in the range of 2.4 to 3.2. These theories, however, do not account for the effect of particle velocity threshold below which no erosion takes place. The present analysis includes this effect.

Equation (3.44) gives the estimate of volumetric material removal rate in AJM. It contains the term  $u_{pc}$  which is essentially a material dependent parameter and can be evaluated from equation (3.8). To obtain the particle velocity at the jet centre line  $u_{pm}$  at a specified stand-off distance, flow governing equations of gas-particle mixture flow in nozzle [equations (2.68), (2.69), (2.71), (2.73), (2.74), (2.75) and (2.84)] and in the jet region [equations (2.108), (2.110) and (2.112)] can be solved numerically taking particle velocity ratio  $c_s$  to be 0.935 at the nozzle inlet as obtained in Appendix-VI. Following the solution technique given in Chapter 2 the particle velocity at the jet centre line for various stand-off distances in a free air-abrasive jet has been computed for the nozzle geometry shown in Fig. I.1 and for the input parameters listed in Appendix-VII.

Evaluation of volumetric material removal rate from equation (3.44) requires the knowledge of  $\lambda$ . For the purpose of theoretical analysis,  $\lambda$  was assumed to be a function of dimensionless stand-off distance  $x_d^*$ . Values of  $\lambda$  evaluated from the experimental data (Fig. 5.1) indicate that  $\lambda$  can be expressed as

$$\lambda = x_d^* (c_6 + c_7 x_d^*) \quad , \quad (5.1)$$

where  $c_6$  and  $c_7$  are constants. Here dimensionless stand-off distance  $x_d^*$  is given by

$$x_d^* = \frac{x_d}{d_{no}} \quad , \quad (5.2)$$

where  $x_d$  is the stand-off distance and  $d_{no}$  is the nozzle exit diameter. Constants  $c_6$  and  $c_7$  evaluated from the experimental data, Table 5.1, indicate that for the range of mixture ratio used the variations in their values are small. For the range of mixture ratio considered the average values of  $c_6$  and  $c_7$  may be taken as  $8.53 \times 10^{-3}$  and  $-1.72 \times 10^{-4}$ .

Using the proposed erosion model the variation of theoretical material removal rate with stand-off distance has been plotted in Fig. 5.2. For qualitative comparison

the experimental data are also plotted which show satisfactory agreement between the theory and experiments. Experimental as well as theoretical results (Figs. 4.8 and 5.2) show that the material removal rate first increases with increase in stand-off distance and then decreases giving an optimum value. This pattern of curve is essentially due to the combination of inertia effects in suspended particles and particle-particle interaction effect. The carrier fluid attains a maximum velocity at the nozzle exit but abrasive particles being heavier tend to lag behind and attain the maximum velocity some distance away from the nozzle exit. On exit from the nozzle the jet flares up due to entrainment of the surrounding stagnant fluid and the carrier fluid velocity decreases. At some stage in the jet region the carrier fluid velocity and the velocity of abrasive particles attain the same value i.e., the velocity of slip reduces to zero. Beyond this the jet flares significantly and the particle velocity decreases and eventually reaches a value ( $u_{pim} \leq u_{pc}$ ) when no erosion can take place. At this stage the abrasive particles and work material will essentially have elastic impact. Equation (3.44) indicates that the erosion rate is a function of impingement velocity. Hence, the volume of material removed will increase as impingement velocity of abrasive particle

increases. With the flaring of the jet, although the particle velocity decreases, the effective number of impact per unit time increases due to decreased particle-particle interaction effect and the impingement takes place over a larger area. The combined effect of these parameters i.e. impingement velocity, particle-particle interaction effect and impingement area will give an optimum value of stand-off distance for maximum material removal rate.

Figs. 4.8 and 5.2 further reveal that the maximum material removal rate at various values of mixture ratio appears to occur at around the same value of stand-off distance. Thus, the mixture ratio does not seem to have any effect on the value of stand-off distance corresponding to the maximum material removal rate. Although the velocity of abrasive particle decreases with increase in mixture ratio at a specified stand-off distance, but the number of particles impacting the work surface increases, giving increased erosion rate. Further, in the range of mixture ratios used it appears that the combined effect of particle-particle interaction and the velocity of abrasive particle do not change significantly since the maximum material removal rate at various values of mixture ratio are at almost the same stand-off distance.

The volume/weight of the eroded material is of importance in operations such as polishing, deburring etc., while in micro-drilling and cutting operations it is the erosion depth (depth of penetration) which is more relevant. The variation of penetration rate with stand-off distance is shown in Figs. 4.6 and 4.9. It is clear that the penetration rate also attains an optimum value but the corresponding stand-off distance is much smaller than the value where maximum material removal rate is obtained. The penetration rate essentially depends on the impingement velocity and the particle-particle interaction effect, whereas material removal rate is also influenced by the area of impingement. The entrainment of the surrounding fluid results in flaring of the jet which causes further non-uniform velocity distribution of the solid particles across the jet section (Fig. 2.2). The particles at the centre will have higher velocity than those at the periphery of the jet. Due to this non-uniform velocity distribution of the solid particles in the jet the maximum value of the average velocity of particles occurs at a smaller stand-off distance than that where the centre line velocity of the particle in the jet attains the maximum. The combined effect of particle-particle interaction and the maximum

value of the average velocity of the solid particles gives the optimum penetration rate. Fig. 4.6 indicates that the maximum penetration rate is attained at a stand-off distance of 7.2 mm which corresponds to approximately 10 times the nozzle exit diameter. Thus, this point will correspond to the point where the combined effect of maximum average velocity and effective number of impacts per unit time (inverse of particle-particle interaction effect) attain the maximum. Beyond this point the particle-particle interaction effect further decreases causing increased number of impacts per unit time but the decrease in average particle velocity is more, resulting in decreased penetration rate.

Fig. 4.9 shows that at low mixture ratio (0.095) the maximum penetration occurs at approximately 7.5 times the nozzle exit diameter, but when the mixture ratio is increased to 0.268 the maximum penetration occurs at approximately 14.5 times the nozzle exit diameter. This is because of the delayed acceleration of abrasive particles when the mixture ratio is high. Flow analysis of gas-solid particle mixture jet (Sec. 2.7.2 and 2.7.3) reveals that the distance at which the particle in the jet attains the maximum velocity depends on the length of the potential core ( $x_c$ ) of the jet. Equation (2.97)



shows that the potential core length in gas-solid particle mixture jet depends on the mixture ratio, higher mixture ratio gives larger potential core length. Thus, the distance at which the average value of particle velocity in the jet attains the maximum will depend on the potential core length and thereby on the mixture ratio. The penetration rate depends on the average value of the particle velocity at any section of the air-abrasive jet and therefore at higher values of mixture ratio maximum penetration rate will occur at larger stand-off distance. The increase in penetration rate with increasing mixture ratio is due to the increase in number of particles taking part in erosion in a specified time.

The top diameter of eroded cavity increases with increase in mixture ratio as well as stand-off distance as shown in Fig. 4.10. This effect is due to the flaring of the jet which increases with increase in stand-off distance as well as with increase in mixture ratio.

Fig. 4.11 indicates that coarse particles give higher values of volume erosion factor than fine particles. Equation (3.44) indicates that for a specified mass flow rate of abrasive particles the volumetric material removal rate is proportional to the impacting particle diameter and thus coarse particles will give higher volume erosion

factor. For a specified mixture ratio the number of particles per unit volume of mixture will be less for the coarse particle resulting in decreased particle-particle interaction compared to fine particle. Coarse particle although attains low velocity but due to decreased particle-particle interaction effect it gives more number of impacts onto the work surface in a specified time giving higher material removal rate. The velocity achieved by fine particles is higher but increased particle-particle interaction effect results in lower volume erosion factor. It appears from Fig. 4.11 that in the size range of particles used, the combined effect of particle size and number of impacts onto the work surface in a specified time results in increased volume erosion factor with coarse grains. The net effect of particle-particle interaction, velocity and the diameter of particle also appears to be such that the optimum stand-off distance for maximum value of volume erosion factor remains more or less unaffected.

Fig. 4.12 shows that the optimum material removal rate increases almost linearly with increase in mixture ratio. The higher the mixture ratio, the greater will be the number of particles per unit volume of the mixture. Thus, the number of particles impacting<sup>n</sup> the work surface

---

increases with increase in mixture ratio. The proportionality relationship in Fig. 4.12 will, however, exist as long as the particles remain in suspension with the carrier fluid and the particle-particle interaction effect is small. Thus, for low mixture ratio values the material removal rate can be taken to be directly proportional to the mixture ratio. At higher values of mixture ratio, the curve will have a drooping characteristic. This is because at higher mixture ratios the quantity of the carrier fluid will not be sufficient to impart the required momentum and energy to the abrasive particle and the particle may tend to settle. Also, at higher mixture ratios the particle-particle interaction effect increases and the particle velocity decreases since less energy is available from the carrier fluid. These factors will cause decreased material removal rate at higher mixture ratios. For the same mixture ratio coarse grains give higher material removal rates than fine grains because of larger impacting particles and decreased particle-particle interaction effect. Also the proportionality limit of mixture ratio for fine particles is more than that for the coarse particles due to the inertia effects. For any specified mixture ratio, the coarse particles being heavier have larger velocity slip resulting in lower particle velocity. Thus, the limiting value of mixture ratio upto which the material removal rate is proportional is lower for coarse particle.

Fig. 4.13 shows the variation of penetration rate with stand-off distance for different particle sizes. The coarse particles being heavier accelerate slower and hence, the penetration rate attains a maximum at a larger value of stand-off distance. Further, the coarse particles have small particle-particle interaction effect thus have more number of impacts on the workpiece surface in a given time. The depth of erosion per particle impact is proportional to the lateral crack depth produced under the impact which in turn is proportional to the impacting particle diameter [equation (3.29)]. Thus, coarse particles will give higher penetration rate.

The effect of nozzle pressure on volumetric material removal rate under specified machining conditions is shown in Fig. 4.14. It can be seen that as pressure increases the rate of material removal increases but it tends to saturate beyond a certain value. In convergent-straight nozzles the maximum velocity attainable at nozzle exit is sonic velocity [119]. Thus, increasing the pressure above a critical value would not increase the jet velocity beyond the sonic velocity and the material removal rate will tend to saturate. The critical pressure limit, however, depends on the mixture ratio, high mixture ratio requiring higher pressure to reach the sonic velocity [90]. Increased mixture

increases the number of particles exposed to acceleration by the carrier fluid resulting in increased particle drag. Also increased number of particles imposes a proportionally higher frictional drop on air flow through nozzle. These effects will cause the pressure required for achieving a given velocity at the nozzle exit to increase with increasing mixture ratio as seen in Fig. 4.14. In order to achieve erosion, a minimum impact velocity ( $u_{pc}$ ) is required. This threshold velocity ( $u_{pc}$ ) will vary with the properties of the impacting particle and the workpiece material [equation (3.8)]. Fig. 4.14 indicates that the threshold velocity is achieved when nozzle pressure is around 55 kN/m<sup>2</sup> (gauge).

## 5.2 Nozzle Wear

Ductile erosion studies [12-18] have revealed that the erosion rate is a function of the velocity and the angle of impingement of the impacting particles [equation (1.3)]. Experiments using split nozzles have revealed that most of the wear occurs in the straight passage at the nozzle exit. The wear is negligibly small in the convergent region of the nozzle. Further, the wear rate increases from the entry to the exit of the straight region of the nozzle as shown in Fig. 4.4. Theoretical estimate of solid particle velocity inside the nozzle of convergent-straight geometry as

shown in Fig. 4.4(a), is obtained using the procedure given in Chapter 2 for the input conditions listed in Appendix-VII and is plotted in Fig. 5.3 as a function of nozzle length to exit diameter ratio. Fig. 5.3 shows that the increase in the velocity of solid particle is negligibly small in the convergent region of the nozzle whereas faster increase in velocity is seen in the straight region of the nozzle. Further, the solid particle velocity increases with increase in length to exit diameter ratio of the nozzle. This is because of the inertia effect of the suspended particles. Since the carrier fluid is lighter it accelerates faster and attains its maximum velocity at the end of convergent region of the nozzle, whereas heavier solid particles tend to lag behind the fluid and continue to accelerate even in the straight region of the nozzle. In the initial part of the straight region the solid particle accelerates faster because of large velocity of slip, whereas in later part the acceleration rate decreases and attains a steady state value. As the wear volume depends strongly on the velocity, it increases as the particle moves in the straight region of the nozzle. Figs. 4.16 and 4.17 provide further evidence that the wear rate is higher for longer nozzle lengths.

The particle velocity within the nozzle is also a function of the nozzle diameter. The variation of theoretical velocity of particle with the length of nozzle for various nozzle diameters is shown in Fig. 5.4. For a specified inlet diameter and entrance angle of the convergent part, the length of the convergent region of the nozzle will be greater for smaller exit diameters. For particulate flow the solid particles accelerate because of the exchange of momentum and energy due to interaction with the carrier fluid. Because of the effects of inertia a finite length is required to accelerate the solid particles. Thus, the particle velocity will be greater for smaller exit diameters and vice-versa. The nozzle diameter increases during use, resulting in a decreased particle velocity which in turn causes a decrease in the wear rate. This is clearly shown in Figs. 4.16 and 4.18 where the curves show a decrease in the wear rate (slope of the wear index curve) with time. The wear index is initially almost linear and then saturates. This is because the velocity of the particle decreases as nozzle diameter increases due to erosion and hence the wear rate decreases from its initial high value. The effect of nozzle diameter on wear index is shown in Fig. 4.19. Since the particle velocity is greater for smaller exit diameter (Fig. 5.4), the resulting wear rate is high.

Fig. 4.20 shows the effect of nozzle entrance angle on the wear index. The wear increases with decreasing entrance angle because the effective length of the convergent region of the nozzle increases resulting in increased particle velocity. Thus the wear rate must increase with decreasing entrance angle.

The mixture ratio is another important parameter affecting erosion in gas-solid flow. Fig. 4.22 shows that the wear rate increases when the mixture ratio is increased. This is obvious from the fact that the number of particle impacting on the nozzle surface will increase with increasing mixture ratio and hence the erosion rate will increase. The erosion rate, however, is unlikely to increase continuously since the carrier fluid at higher mixture ratios, may not be able to impart sufficient momentum to accelerate the solid particles. Thus, acceleration of solid particles beyond a specific mixture ratio will be low, resulting in a low particle velocity and a decreased wear rate.

The effect of grain size on nozzle wear has also been investigated by comparing the results obtained using abrasive particles of 30 and 38  $\mu\text{m}$ . The erosion of the material is a function not only of the impingement velocity but also of the size of the impinging particles because the volume of the cavity eroded by a single particle is a function of the



contact diameter between the impacting particle and the target surface [24]. The contact diameter, in turn, is a function of the particle diameter, the properties of the particle and the target materials and the impingement velocity [108]. A larger particle will remove more material than a smaller particle at the same impact velocity. The inertia of a large particle is however greater and hence the velocity attained will be lower. The number of particles impinging on the surface at a given mixture ratio also depends on the particle size. Thus, smaller particles will undergo more impacts but, since the contact diameter is small, they will erode a smaller volume. Larger grains, in contrast, will undergo fewer impacts but, because of their larger contact diameter, will erode a larger volume. The effect of particle size on erosion rate is therefore a combined function of particle velocity, particle size and the number of impacting particles. In the range of particle size used, larger particles appear to give higher erosion rate.

TABLE 5.1Values of the Experimental Constants  $c_6$  and  $c_7$ 

Mixture ratio	$c_6$	$c_7$
0.095	$8.26 \times 10^{-3}$	$- 1.81 \times 10^{-4}$
0.148	$8.63 \times 10^{-3}$	$- 1.80 \times 10^{-4}$
0.201	$9.16 \times 10^{-3}$	$- 1.93 \times 10^{-4}$
0.268	$8.07 \times 10^{-3}$	$- 1.34 \times 10^{-4}$

Average values :

$$c_6 = 8.53 \times 10^{-3}$$

$$c_7 = -1.72 \times 10^{-4}$$

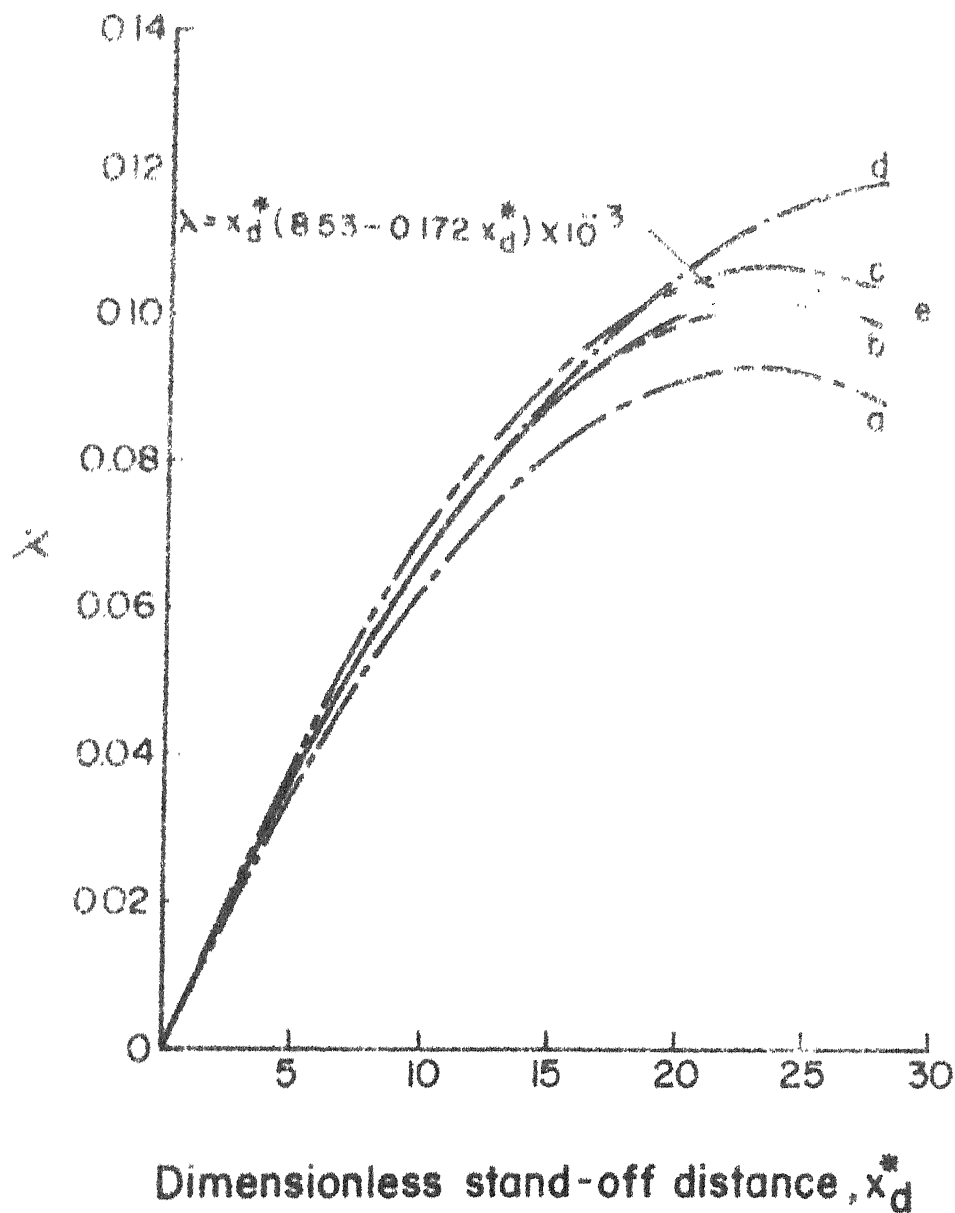
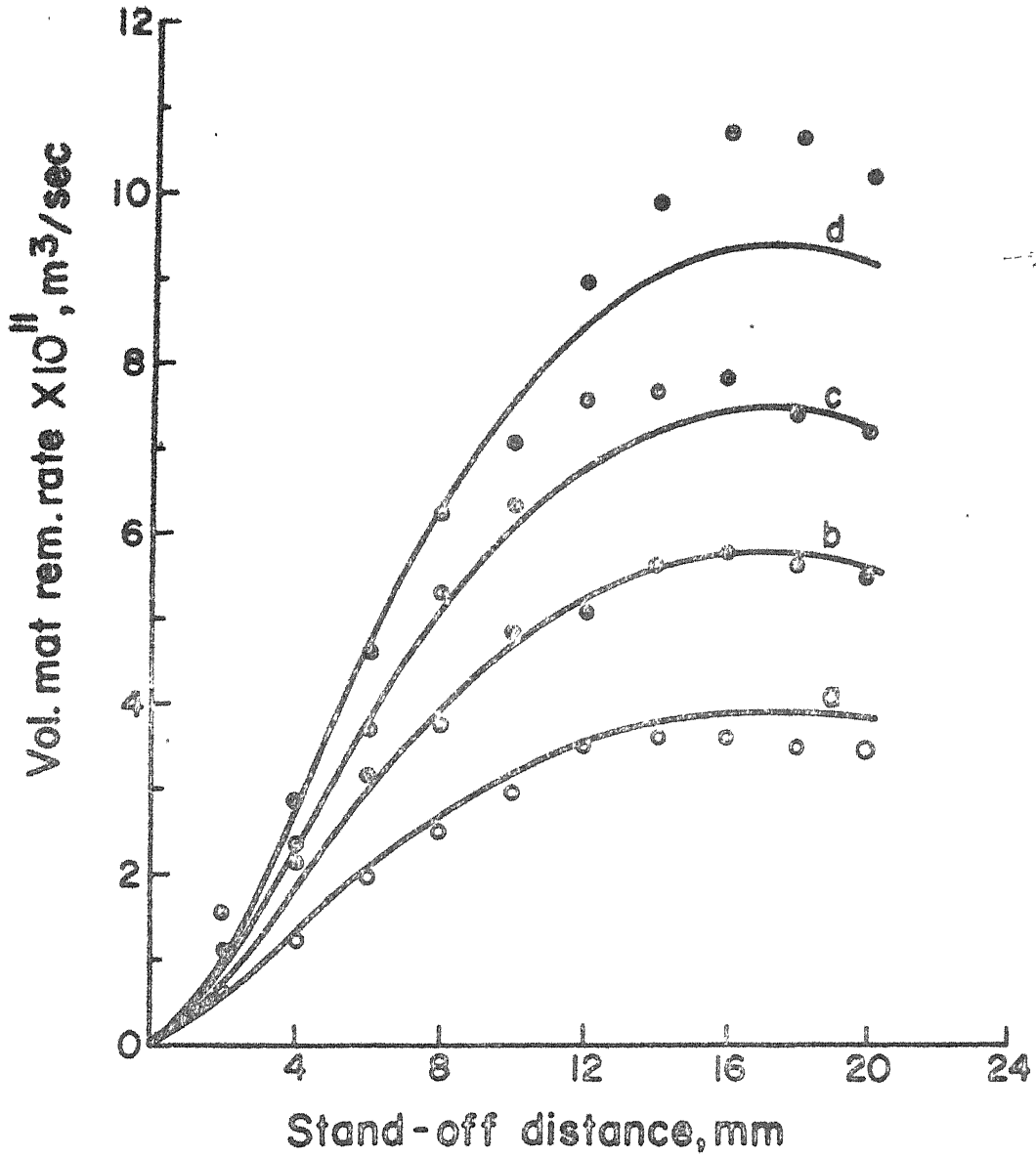


Fig. 5.1 Variation of  $\lambda$  with dimensionless stand-off distance for different mixture ratios (a) 0.095, (b) 0.148, (c) 0.201, (d) 0.268 and (e) mean curve.  $d_p$ : 30  $\mu\text{m}$ ; nozzle pressure: 147.15  $\text{kN/m}^2$  (gauge).



**Fig.5.2** Variation of theoretical as well as experimental volumetric material removal rate with stand-off distance for different mixture ratios (a) 0.095, (b) 0.148, (c) 0.201 and (d) 0.268.  $d_p$ :  $30\mu\text{m}$ ; nozzle pressure:  $147.15 \text{ kN/m}^2(\text{gauge})$ .

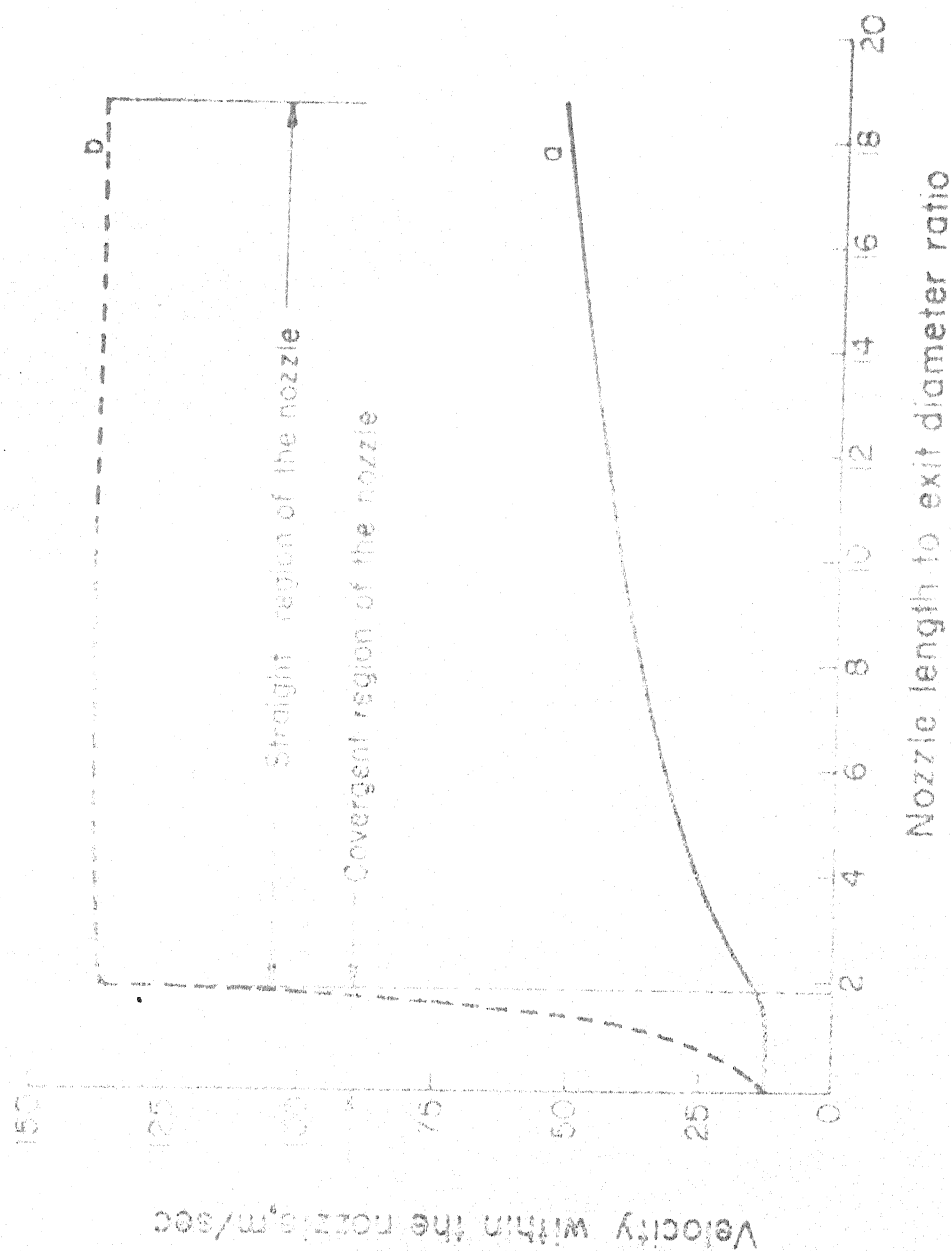


Fig. 5.3 Theoretical estimate of (a) abrasive particle velocity and (b) carrier fluid velocity at different sections of the nozzle.  $d_{no} = 0.97$  mm;  $l_n = 16.18$  mm;  $\beta = 30^\circ$ ;  $d_p = 38$   $\mu$ m;  $\alpha = 0.201$ .

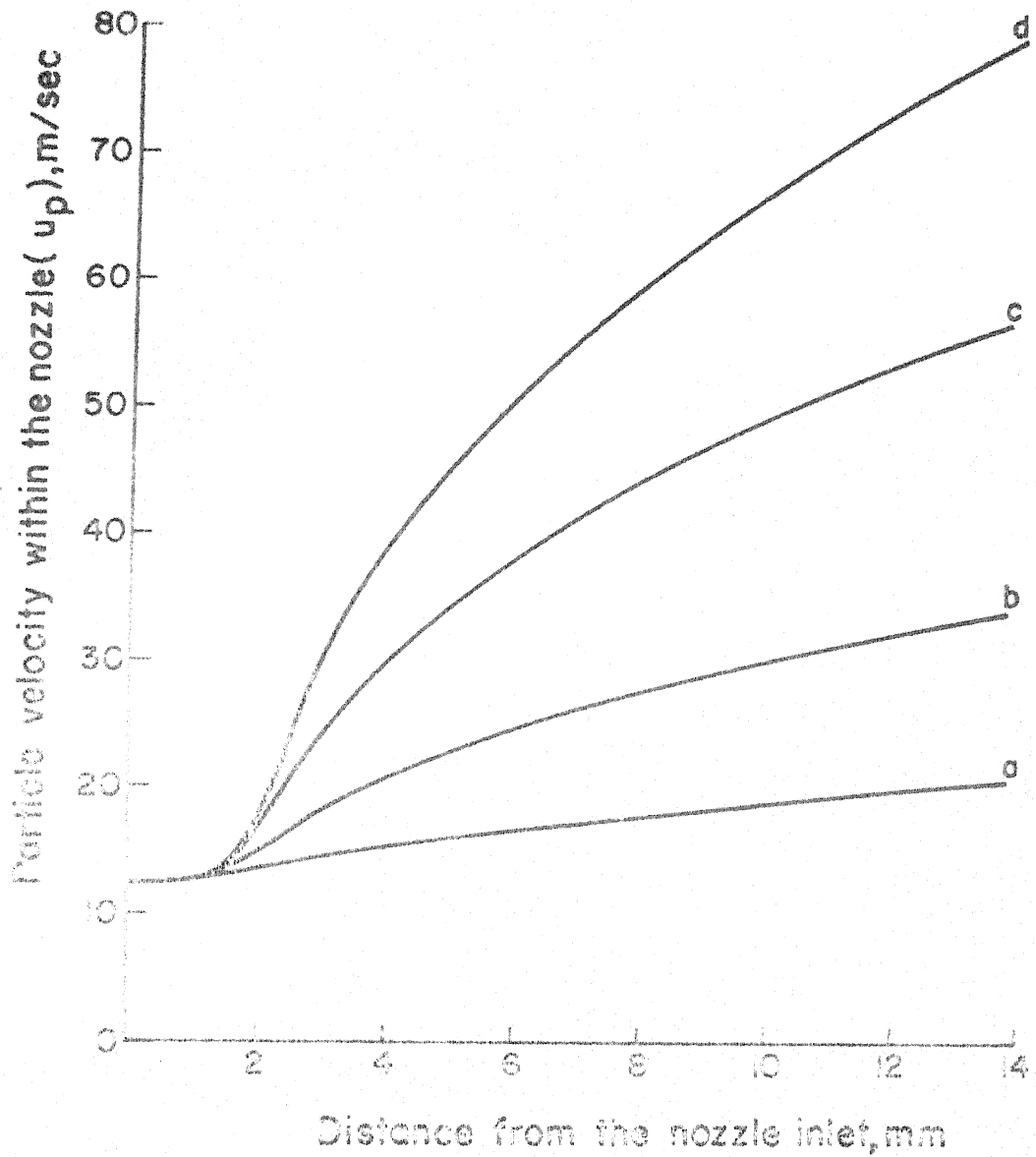


Fig. 5.4 Theoretical estimate of abrasive particle velocity at different sections of the nozzle for various exit diameters (a) 1.62 mm, (b) 1.17 mm, (c) 0.9 mm and (d) 0.8 mm.  $l_n$ : 12 mm;  $\beta$ :  $30^\circ$ ;  $d_p$ :  $38 \mu\text{m}$ ;  $\alpha$ : 0.201.

## CHAPTER 6

### CONCLUSIONS AND SCOPE FOR FURTHER RESEARCH

#### 6.1 Conclusions

Abrasive jet machining can be used for polishing, deburring and other finishing operations where the rate of material removal is important and for operations such as micro-drilling and cutting where the erosion depth is more relevant. The theoretical analysis for brittle erosion predicts that erosion rate depends on density, size and velocity of impacting particles as well as hardness, fracture toughness and shear modulus of the workpiece material. The velocity of impacting particles, however, is the main parameter governing the erosion rate. The value of velocity exponent in the erosion equation is 2.75 for typical glass and ceramic materials. There also exists a threshold velocity below which no erosion occurs and its value depends on workpiece hardness, density of impacting particle and elastic constants of workpiece and particle materials. Further, the theoretical analysis of two-phase flow through nozzle as well as jet reveals that the velocity of solid particle in air-abrasive jet depends on particle size, density of particle material, mixture ratio

and carrier gas pressure. Solid particles being heavier in inertia continue to accelerate even after the nozzle exit and attain the maximum velocity at some distance away from the nozzle exit. The analysis therefore indicates that the erosion rate depends on stand-off distance, mixture ratio, particle size and carrier gas pressure.

The experimental study of effects of these parameters on volumetric material removal rate as well as penetration rate have been successfully carried out on the experimental abrasive jet machine specially designed and fabricated for the purpose. Results indicate that both material removal rate and penetration rate first increase with increase in stand-off distance and then decrease giving optimum values. Theoretical curves also indicate this and there appears qualitative agreement between the two. Maximum values of material removal rate and penetration rate are, however, obtained at different values of stand-off distance. Increase in mixture ratio causes increase in material removal rate as well as penetration rate. In the range of mixture ratios used during the experiments, the material removal rate appears to vary linearly with mixture ratio. This linearity limit appears to vary with grain size. The maximum value of material removal rate appears to occur at the same value of stand-off distance, while the maximum penetration rate



occurs at different values of stand-off distance when mixture ratio is varied. The size of abrasive particle affects the value of stand-off distance for maximum penetration rate, but does not seem to affect the value of stand-off distance for maximum material removal rate. It appears from the result that operations such as deburring and polishing should be carried out at larger stand-off distances, whereas smaller stand-off distances should be used for cutting, micro-drilling etc.

Experiments performed using split convergent-straight nozzles clearly indicate that nozzle wear increases almost linearly from entry to exit. The profile of the straight flow passage after wear closely approximates a truncated cone. The wear volume could therefore be estimated with reasonable accuracy from measurements of the entrance and exit diameters of the straight passage of the nozzle. Wear in the convergent portion appears to be negligibly small. Experiments clearly indicate that nozzle wear increases with increasing nozzle length and decreasing nozzle diameter. Similarly, nozzle wear increases when the entrance angle of the nozzle is decreased. Nozzle wear rate also increases with increase in particle size and mixture ratio.

## 6.2 Scope for Further Research

The mechanics of material removal in AJM and the wear characteristics of the nozzle used in the process are not fully understood and the present work can be extended for the case of axially symmetric three dimensional analysis of two-phase flow. The axi-symmetric impinging jet analysis can be carried out to account for particle-particle interaction and velocity, and effective number of impacts can be obtained at different stand-off distances for realistic estimate of material removal rate as well as penetration rate.

The work can be extended to study the tapering effect due to flaring of the jet, an inherent characteristic of the process. This effect can perhaps be minimized by using co-axial twin jet of air and air-abrasive mixture. The investigation can be carried out theoretically as well as experimentally to minimize jet flaring.

Practically nothing appears to be known about nozzle design. The nozzle used imparts high velocity to the abrasive particles and thus the nozzle geometry has significant influence on the performance characteristic of the process. The work can be extended to investigate the effects of nozzle parameters on process performance and nozzle life.

## BIBLIOGRAPHY

- [1] Merchant, M.E., 'Recent Progress in Metal Removal Research at Cincinnati', Int. J. Machine Tool Des. Res., Vol. 1, 1961, p. 79.
- [2] Lavoie, F.J., 'Abrasive Jet Machining', Machine Des., Vol. 45, 1973, p. 135.
- [3] Ingulli, C.N., 'Abrasive Jet Machining', Tool and Manuf. Engrs., Vol. 59, 1967, p. 28.
- [4] Bhattacharyya, A., 'New Technology', The Institution of Engineers (India), 1977.
- [5] Sarkar, P.K. and Pandey, P.C., 'Some Investigations on Abrasive Jet Machining', J. Inst. of Engrs. (India), Vol. 56, Part ME-5, 1976, p. 284.
- [6] Neema, M.L. and Pandey, P.C., 'Erosion of Glass When Acted Upon by an Abrasive Jet', Proc. Int. Conf. On Wear of Materials, Held at St. Louis, April 1977, p.387.
- [7] Wolak, J., Worm, P., Patterson, I. and Bodoia, J., 'Parameters Affecting the Velocity of Particles in an Abrasive Jet', Trans. ASME, J. Eng. Mat. and Tech., Vol. 99, 1977, p. 147.
- [8] Wellinger, K. and Uetz, H., 'Gleit-Spül-und Strahlverschleiss-Prüfung', Wear, Vol. 1, 1957-58, p. 225.
- [9] Finnie, I., 'Erosion of Surface by Solid Particles', Wear, Vol. 3, 1960, p. 87.
- [10] Finnie, I., Wolak, J. and Kabil, Y.H., 'Erosion of Metals by Solid Particles', J. Mater., Vol. 2, 1967, p. 682.
- [11] Sheldon, G.L., and Finnie, I., 'On the Ductile Behaviour of Nominally Brittle Materials During Erosive Cutting', Trans. ASME, J. Eng. for Ind., B88, 1966, p. 387.
- [12] Fisher, M.A. and Davis, F.E., 'Study on Fly-Ash Erosion', Mech. Eng., Vol. 71, 1949, p. 481.

- [13] Stoker, R.L., 'Erosion Due to Dust Particles in a Gas Stream'', Ind. and Eng. Chem., Vol. 41, 1949, p. 1196.
- [14] Finnie, I., 'The Mechanism of Erosion of Ductile Metals'', ASME, Proc. 3rd U.S. Nat. Congress of Applied Mechanics, 1958, p. 527.
- [15] Finnie, I. and McFadden, D.H., 'On the Velocity Dependence of the Erosion of Ductile Metals by Solid Particles at Low Angles of Incidence'', Wear, Vol.48, 1978, p. 181.
- [16] Bitter, J.G.A., 'A Study of Erosion Phenomena Part-I'', Wear, Vol. 6, 1963, p. 5.
- [17] Bitter, J.G.A., 'A Study of Erosion Phenomena Part-II'', Wear, Vol. 6, 1963, p. 169.
- [18] Neilson, J.H. and Gilchrist, A., 'Erosion by a Stream of Solid Particles'', Wear, Vol. 11, 1968, p. 111.
- [19] Tilly, G.P., 'A Two-Stage Mechanism of Ductile Erosion'', Wear, Vol. 23, 1973, p. 87.
- [20] Tilly, G.P., 'Erosion Caused by Airborne Particles'', Wear, Vol. 14, 1969, p. 63.
- [21] Goodwin, J.E., Sage, W. and Tilly, G.P., 'A Study of Erosion by Solid Particles'', Proc. Inst. Mech. Engrs., Vol. 184, 1969, p. 279.
- [22] Tilly, G.P. and Sage, W., 'The Interaction of Particle and Material Behaviour in Erosion Processes'', Wear, Vol. 16, 1970, p. 447.
- [23] Shewmon, P.G., 'Particle Size Threshold in Erosion of Metals'', Wear, Vol. 68, 1981, p. 253.
- [24] Sheldon, G.L. and Kanhere, A., 'An Investigation of Impingement Erosion Using Single Particles'', Wear, Vol. 21, 1972, p. 195.
- [25] Ruff, A.W. and Wiederhorn, S.M., 'Erosion by Solid Particle Impact'', Treatise On Materials Science and Technology, Academic Press, Vol. 16, 1979, p. 69.

- [26] Hutchings, I.M. and Winter, R.E., 'Particle Erosion of Ductile Metals : A Mechanism of Material Removal', Wear, Vol. 27, 1974, p. 121.
- [27] Hutchings, I.M. and Winter, R.E., 'The Erosion of Ductile Metals by Spherical Particles', J. Phys. D. Appl. Phys., Vol. 8, 1975, p. 8.
- [28] Winter, R.E. and Hutchings, I.M., 'Solid Particle Erosion Studies Using Single Angular Particles', Wear, Vol. 29, 1974, p. 181.
- [29] Hutchings, I.M., 'Deformation of Metal Surfaces by the Oblique Impact of Square Plates', Int. J. Mech. Sci., Vol. 19, 1977, p. 45.
- [30] Hutchings, I.M., 'Erosion of Metals by Solid Particles - A Study Using High-Speed Photography', 12th Int. Congr. On High Speed Photogr., Held at Toronto, Ont., August 1976, SPIE Semin. Proc., Vol. 97, 1977, p. 358.
- [31] Brown, S.K. and Jun, E.J., 'The Effect of Particle Shape and Size on Erosion of Aluminium Alloy 1100 at 90 Degrees Impact Angle', Wear, Vol. 88, 1983, p. 181.
- [32] Ives, L.K. and Ruff, A.W., 'Transmission and Scanning Electron Microscopy Studies of Deformation at Erosion Impact Sites', Wear, Vol. 46, 1978, p. 149.
- [33] Eui-Jin Jun, B.B. and Edington, J.W., 'Mechanism of Solid Particle Erosive Wear for 90 Degrees Impact on Copper and Iron', Wear, Vol. 74, 1981-82, p. 143.
- [34] Turbe, E.B.I., Greenfield, I.G. and Chau, T.W., 'The Wear Mechanism Obtained in Copper by Repetitive Impacts', Wear, Vol. 74, 1981-82, p. 123.
- [35] Follansbee, P.S., Sinclair, G.B. and Williams, J.C., 'Modelling of Low Velocity Particulate Erosion in Ductile Materials by Spherical Particles', Wear, Vol. 74, 1981, p. 107.
- [36] Sundararajan, G., 'An Analysis of the Localization of Deformation and Weight Loss During Single Particle Normal Impact', Wear, Vol. 84, 1983, p. 217.
- [37] Sundararajan, G. and Shewmon, P.G., 'A New Model for the Erosion of Metals at Normal Incidence', Wear, Vol. 84, 1983, p. 237.

- [38] Levy, A.V., 'The Solid Particle Erosion Behaviour of Steel as a Function of Microstructure', Wear, Vol.68, 1981, p. 269.
- [39] Foley, T. and Levy, A., 'The Erosion of Heat Treated Steels', Wear, Vol. 91, 1983, p. 45.
- [40] Young, J.P. and Ruff, A.W., 'Particle Erosion Measurements On Metals', Trans. ASME, J. Eng. Mat. and Tech., Vol. 99, 1977, p. 121.
- [41] Ives, L.K., 'Erosion of 310 Stainless Steel at 975°C in Combustion Gas Atmospheres', Trans. ASME, J. Eng. Mat and Tech , Vol. 99, 1977, p. 126.
- [42] Yee, K.H., Shayler, P.J. and Collings, N., 'Erosion of Metals by Fly-ash Particles', Wear, Vol.91, 1983, p.161.
- [43] Engel, P.A., 'Impact Wear of Materials', Elsevier Scientific Publishing Company, 1976.
- [44] Smeltzer, C.E., Gulden, M.E. and Compton, W.A., 'Mechanisms of Metal Removal by Impacting Dust Particles', Trans. ASME, J. Basic Eng., Vol. 92, 1970, p. 639.
- [45] Levy, A.V. and Chik, P., 'The Effects of Erodent Composition and Shape on the Erosion of Steel', Wear, Vol. 89, 1983, p. 151.
- [46] Sheldon, G.L. and Finnie, I., 'The Mechanism of Material Removal in the Erosive Cutting of Brittle Materials', Trans. ASME, J. Eng. for Ind., Vol. 88B, 1966, p. 393.
- [47] Sheldon, G.L., 'Similarities and Differences in the Erosion Behaviour of Materials', Trans. ASME, J. Basic Eng., Vol. 92, 1970, p. 619.
- [48] Lawn, B.R. and Wilshaw, T.R., 'Review Indentation Fracture : Principles and Applications', J. Mater. Sci., Vol. 10, 1975, p. 1049.
- [49] Oh, H.L., Oh, K.P.L., Vaidyanathan, S. and Finnie, I., 'The Science of Ceramic Machining and Surface Finish', N.B.S. Special Publication 348, Edited by Schneider, S.J. and Rice, R.W., 1972, p. 119.

- [50] Evans, A.G. and Wilshaw, T.R., 'Quasi-static Solid Particle Damage in Brittle Solids - I: Observation, Analysis and Implications', *Acta Metallurgica*, Vol. 24, 1976, p. 939.
- [51] Swain, M.V. and Hagan, J.T., 'Indentation Plasticity and the Ensuing Fracture of Glass', *J. Phys. D : Appl. Phys.*, Vol. 9, 1976, p. 2201.
- [52] Studman, C.J. and Field, J.E., 'The Indentation of Hard Metals : The Role of Residual Stresses', *J. Mater. Sci.*, Vol. 12, 1977, p. 215.
- [53] Evans, A.G., 'Impact Damage in Ceramics', *Fracture Mechanics of Ceramics*, Plenum Press, Vol. 3, 1978, p. 303.
- [54] Lawn, B.R. and Marshall, D.B., 'Indentation Fracture and Strength Degradation', *Fracture Mechanics of Ceramics*, Plenum Press, Vol. 3, 1978, p. 205.
- [55] Lawn, B.R., Wiederhorn, S.M. and Johnson, H.H., 'Strength Degradation of Brittle Surfaces; Blunt Indenter', *J. Am. Ceram. Soc.*, Vol. 58, 1975, p. 428.
- [56] Frank, F.C. and Lawn, B.R., 'On the Theory of Hertzian Fracture', *Proc. Royal Soc. London*, Vol. A299, 1967, p. 291.
- [57] Langitan, F.B. and Lawn, B.R., 'Hertzian Fracture Experiments on Abraded Glass as Definitive Evidence for an Energy Balance Explanation of Auerbach's Law', *J. Appl. Phys.*, Vol. 40, 1969, p. 4009.
- [58] Evans, A.G., 'Strength Degradation by Projectile Impacts', *J. Am. Ceram. Soc.*, Vol. 56, 1973, p. 405.
- [59] Wiederhorn, S.M. and Lawn, B.R., 'Strength Degradation of Glass Resulting From Impact with Spheres', *J. Am. Ceram. Soc.*, Vol. 60, 1977, p. 451.
- [60] Knight, C.G., Swain, M.V. and Chaudhri, M.M., 'Impact of Small Steel Spheres on Glass Surfaces', *J. Mater. Sci.*, Vol. 12, 1977, p. 1573.
- [61] Lawn, B.R., Fuller, E.R. and Wiederhorn, S.M., 'Strength Degradation of Brittle Surfaces : Sharp Indenters', *J. Am. Ceram. Soc.*, Vol. 59, 1976, p. 193.

- [62] Lawn, B.R. and Swain, M.V., 'Microfracture Beneath Point Indentation in Brittle Solids', J. Mater. Sci., Vol. 10, 1975, p. 113.
- [63] Evans, A.G., Gulden, M.E. and Rosenblatt, M., 'Impact Damage in Brittle Materials in the Elastic-Plastic Response Regime', Proc. Royal Soc. London, Series A, Vol. 361, 1978, p. 343.
- [64] Hockey, B.J., 'Plastic Deformation of Aluminium Oxide by Indentation and Abrasion', J. Am. Ceram. Soc., Vol. 54, 1971, p. 223.
- [65] Hockey, B.J. and Lawn, B.R., 'Electron Microscopy of Microcracking About Indentations in Aluminium Oxide and Silicon Carbide', J. Mater. Sci., Vol. 10, 1975, p. 1275.
- [66] Wiederhorn, S.M. and Lawn, B.R., 'Strength Degradation of Glass Impacted with Sharp Particles; 1, Annealed Surface', J. Am. Ceram. Soc., Vol. 62, 1979, p. 66.
- [67] Hockey, B.J., Wiederhorn, S.M. and Johnson, H., 'Erosion of Brittle Materials by Solid Particle Impact', Fracture Mechanics of Ceramics, Plenum Press, Vol. 3, 1978, p. 379.
- [68] Schuon, S.R. and Subramanian, K.N., 'Impact Erosion of Single Crystal of LiF and CaF<sub>2</sub> by Sharp Projectile', Wear, Vol. 81, 1982, p. 357.
- [69] Lawn, B.R. and Evans, A.G., 'A Model for Crack Initiation in Elastic/Plastic Indentation Fields', J. Mater. Sci., Vol. 12, 1977, p. 2195.
- [70] Marshall, D.B., Evans, A.G., Gulden, M.E., Routbort, J.L. and Scattergood, R.O., 'Particle Size Distribution Effect on the Solid Particle Erosion of Brittle Materials', Wear, Vol. 71, 1981, p. 363.
- [71] Scattergood, R.O. and Routbort, J.L., 'Velocity and Size Dependence of the Erosion Rate in Silicon', Wear, Vol. 67, 1981, p. 227.
- [72] Tabakoff, W., Kotwal, R. and Hamed, A., 'Erosion Study of Different Materials Affected by Coal Ash Particles', Wear, Vol. 52, 1979, p. 161.



- [73] Gulden, M.E., 'Solid Particle Erosion of  $\text{Si}_3\text{N}_4$  Materials'', Wear, Vol. 69, 1981, p. 115.
- [74] Mehrotra, P.K., Sargent, G.A. and Conrad, H., 'A Computer Simulation of the Time Dependence of the Erosion of Pyrex Glass by Glass Beads'', J. Mater. Sci., Vol. 17, 1982, p. 1049.
- [75] Wiederhorn, S.M. and Hockey, B.J., 'Effect of Material Parameters on the Erosion Resistance of Brittle Materials'', J. Mater. Sci., Vol. 18, 1983, p. 766.
- [76] Tien, C.L., 'Fluid-Solid Mixture in a Pipe'', J. of Heat. Trans., Vol. 83, 1961, p. 183.
- [77] Tien, C.L., 'Heat Transfer by a Turbulently Flowing Fluid-Solid Mixture in a Pipe'', J. of Fluid Mech., Vol. 10, 1961, p. 183.
- [78] Cox, R.G. and Mason, S.G., 'Suspended Particles in Fluid Flow Through Tubes'', Annual Rev. Fluid Mech., Vol. 3, 1971, p. 291.
- [79] Soo, S.L. and Tien, C.L., 'Effect of the Wall on Two-Phase Turbulent Motion'', Trans. ASME, J. Fluid Mech., Series E, Vol. 27, 1960, p. 5.
- [80] Soo, S.L., 'Gas Dynamic Processes Involving Suspended Solids'', AIChE. Journal, Vol. 7, 1961, p. 384.
- [81] Rannie, W.D., 'A Perturbation Analysis of One Dimensional Heterogeneous Flow in Rocket Nozzle'', Progress in Astronautics and Rocketry, Academic Press, Vol. 6, 1962.
- [82] Hoglund, R.F., 'Recent Advances in Gas-Particle Nozzle Flows'', ARS Journal, Vol. 32, 1962, p. 662.
- [83] Kliegel, J.R., "Gas-Particle Nozzle Flows", Ninth Int. Symp. on Combustion, Academic Press, 1963, p. 811.
- [84] Ishii, R. and Kawaski, K., 'Limiting Particle Streamline of Gas-Particle Mixture in Axially Symmetric Nozzles'', AIAA Journal, Vol. 18, 1980, p. 1397.
- [85] Chang, I.S., 'One and Two-Phase Nozzle Flow'', AIAA Journal, Vol. 18, 1980, p. 1455.

- [86] Hassan, H.A., 'Exact Solutions of Gas-Particle Nozzle Flows', AIAA Journal, Vol. 2, 1964, p. 395.
- [87] Neilson, J.H. and Gilchrist, A., 'An Analytical and Experimental Investigation of the Velocities of Particles Entrained by the Gas Flow in Nozzles', J Fluid Mech., Vol. 33, 1968, p. 131.
- [88] Okuda, S. and Choi, W.S., 'Gas-Particle Mixture Flow in Various Types of Convergent-Divergent Nozzle', J. Chem. Eng. of Japan, Vol. 11, 1978, p. 432.
- [89] Marble, F.E., 'Nozzle Contours for Minimum Particle Lag Loss', AIAA Journal, Vol. 1, 1963, p. 2793.
- [90] Soo, S.L., 'Fluid Dynamics of Multi-phase Systems', Blaisdell Publishing Co., 1967.
- [91] Corrsin, S. and Lumley, J.L., 'On the Equation of Motion for a Particle in a Turbulent Fluid', Appl. Sci. Res., Sec. A, Vol. 6, 1956, p. 114.
- [92] Hinze, J.O., 'Turbulence', McGraw Hill Pub., 1959.
- [93] Stokes, G.G., 'On the Effect of the Internal Friction of Fluid on the Motion of Pendulums', Trans. Cambr. Phil. Soc., Part II, Vol. 9, 1851, p. 8.
- [94] Gilbert, M., Davis, L., and Altman, D., 'Velocity Lag of Particle in Linearly Accelerated Combustion Gases', Jet Propulsion, Vol. 25, 1955, p. 26.
- [95] Crowe, C.T., 'Review-Numerical Models for Dilute Gas-Particle Flows', Trans. ASME, J. Fluids Eng., Vol. 104, 1982, p. 297.
- [96] Sproull, W.T., 'Viscosity of Dusty Gases', Nature, Vol. 190, 1961, p. 976.
- [97] Saffman, P.G., 'Flow of a Dusty Gas Between Rotating Cylinders', Nature, Vol. 193, 1962, p. 463.
- [98] Mande, A.D., 'The Viscosity of a Suspension of Spheres', J. Fluid Mech., Vol. 7, 1959, p. 230.

- [99] Soo, S.L., ''Dynamics of Multiphase Flow System'', Ind. Eng. Chem. Fundamentals, Vol. 4, 1965, p. 426.
- [100] Schlichting, H., ''Boundary Layer Theory'', McGraw Hill Book Co., 1968.
- [101] Pai, S.I., ''A Review of Fundamental Equations of the Mixture of a Gas with Solid Particles'', Institute For Fluid Dynamics and Applied Mathematics, University of Maryland, Tech. Note BN 668, 1970.
- [102] Gebhart, B., ''Heat Transfer'', McGraw Hill Book Co., 1961.
- [103] Pai, S.I., ''Fluid Dynamics of Jets'', D. Van Nostrand Company, Inc., 1954.
- [104] Abramovich, G.N., ''The Theory of Turbulent Jets'', The MIT Press Massachusetts Inst. of Tech., 1963.
- [105] Prandtl, L., ''The Mechanics of Viscous Fluids'', In Durand, W.F., Aerodynamic Theory III, California Inst. of Tech., Pasadena, California, 1943.
- [106] Albertson, M.L., Dai, Y.B., Jensen, R.A., and Rouse, H., ''Diffusion of Submerged Jets'', Proc. Am. Soc. Civil Engrs., Vol. 74, 1948, p. 1751.
- [107] Lawn, B.R., Swain, M.V., and Phillips, K., ''On the Mode of Chipping Fracture in Brittle Solids'', J. Mater. Sci., Vol. 10, 1975, p. 1236.
- [108] Timoshenko, S., and Goodier, J.N., ''Theory of Elasticity'', McGraw Hill Book Co., 1951.
- [109] Davies, R.M., ''The Determination of Static and Dynamic Yield Stresses Using a Steel Ball'', Proc. Roy. Soc. London, Series A, Vol. 197, 1949, p. 416.
- [110] Marsh, D.M., ''Plastic Flow in Glass'', Proc. Roy. Soc. London, Series A, Vol. 297, 1964, p. 420.
- [111] Tabor, D., ''Hardness of Solids'', Endeavour, Vol. 13, 1954, p. 49.
- [112] Evans, A.G., and Wilshaw, T.R., ''Dynamic Solid Particle Damage in Brittle Materials : An Appraisal'', J. Mater. Sci., Vol. 12, 1977, p. 97.

- [113] Hill, R., 'The Mathematical Theory of Plasticity', Oxford : Clarendon Press, 1950.
- [114] Johnson, K.L., 'The Correlation of Indentation Experiments', J. Mech. Phys. Solids, Vol. 18, 1970, p.115.
- [115] Zenz, F.A., 'Conveyability of Materials of Mixed Particle Size', Ind. and Eng. Chem. Fundamentals, Vol. 3, 1964, p. 65.
- [116] Wen, C.Y. and O'Brien, W.S., 'Pneumatic Conveying and Transporting', Chemical Processing and Engineering (Gas Solids Handling in the Process Industries), Vol.8, Marcel Dekker, Inc., 1976, p. 89.
- [117] Boothroyd, R.G., 'Flowing Gas-Solid Suspension', Chapman and Hall, 1971.
- [118] Zenz, F.A. and Othmer, D.F., 'Fluidization and Fluid-Particle Systems', Reinhold Publishing Corp., 1960.
- [119] Cambel, A.B. and Jennings, B.H., 'Gas Dynamics', McGraw Hill Book Co., 1958.
- [120] Kunii, D. and Levenspiel, O., 'Fluidization Engineering' John Wiley and Sons, Inc., 1969.
- [121] Matsumoto, S., Kikuta, M. and Maeda, S., 'Effect of Particle Size on the Minimum Transport Velocity for Horizontal Pneumatic Conveying of Solids', J. Chem. Eng. of Japan, Vol. 10, 1977, p. 273.

## APPENDIX - I

DIMENSIONLESS FORM OF THE CROSS-SECTIONAL AREA OF  
NOZZLE AND ITS DERIVATIVE

Considering Fig. I.1 the distances  $l_1$  and  $l_2$  measured along the nozzle length from inlet to the end of I convergent region and to the end of II convergent region can be expressed as

$$l_1 = \frac{(d_{n1} - d_{n2})}{2 \tan \beta_1} \quad (\text{I.1})$$

and

$$l_2 = l_1 + \frac{(d_{n2} - d_{no})}{2 \tan \beta_2} \quad , \quad (\text{I.2})$$

respectively. Here  $d_{n1}$ ,  $d_{n2}$  and  $d_{no}$  are the diameters at the inlet, at the end of I convergent region and at the nozzle exit, respectively.  $\beta_1$  and  $\beta_2$  are the semi-entrance angle for the I and II convergent regions of the nozzle.

For any section at a distance  $x$  from the nozzle inlet in I convergent region, the diameter of nozzle passage  $d_n$  can be expressed as

$$d_n = d_{n1} - 2 x \tan \beta_1 \quad \text{for } x \leq l_1 \quad . \quad (\text{I.3})$$

The area  $A_n$  of the nozzle at the considered section is given as

$$A_n = \frac{\pi}{4} (d_{n1} - 2 x \tan \beta_1)^2 \quad \text{for } x \leq l_1 \quad (\text{I.4})$$

Using dimensionless variables discussed in Chapter 2 [Sec. 2.5.2 equation (2.64)], equations (I.1), (I.2) and (I.4) can be written in dimensionless form as

$$l_1^* = \frac{(d_{n1}^* - d_{n2}^*)}{2 \tan \beta_1}, \quad (\text{I.5})$$

$$l_2^* = \frac{d_{n1}^*}{2 \tan \beta_1} + \frac{(\tan \beta_1 - \tan \beta_2) d_{n2}^*}{2 \tan \beta_1 \tan \beta_2} - \frac{1}{2 \tan \beta_2} \quad (\text{I.6})$$

and

$$A_n^* = \left(1 - \frac{2 x^* \tan \beta_1}{d_{n1}^*}\right)^2 \quad \text{for } x^* \leq l_1^* \quad (\text{I.7})$$

Here dimensionless diameters  $d_{n1}^*$  and  $d_{n2}^*$  can be expressed as

$$d_{n1}^* = \frac{d_{n1}}{d_{no}} \quad (\text{I.8})$$

$$\text{and} \quad d_{n2}^* = \frac{d_{n2}}{d_{no}} \quad (\text{I.9})$$

Differentiation of equation (I.7) with respect to  $x^*$  yields

$$\frac{dA_n^*}{dx^*} = -4\left(1 - \frac{2x^* \tan\beta_1}{d_{n1}^*}\right) \left(\frac{\tan\beta_1}{d_{n1}^*}\right) \text{ for } x^* \leq l_1^* \quad (\text{I.10})$$

Similarly in the II convergent region the diameter  $d_n$  of the nozzle passage can be expressed as

$$d_n = (d_{n1} - d_{n2}) \frac{\tan\beta_2}{\tan\beta_1} + d_{n2} - 2x \tan\beta_2 \quad \text{for } l_1 < x \leq l_2 \quad (\text{I.11})$$

The area  $A_n$  can be expressed as

$$A_n = \frac{\pi}{4} \left[ (d_{n1} - d_{n2}) \frac{\tan\beta_2}{\tan\beta_1} + d_{n2} - 2x \tan\beta_2 \right]^2 \quad \text{for } l_1 < x \leq l_2 \quad (\text{I.12})$$

Using dimensionless variables of equation (2.64) equation (I.12) can be written as

$$A_n^* = \left[ \left(1 - \frac{d_{n2}^*}{d_{n1}^*}\right) \frac{\tan\beta_2}{\tan\beta_1} + \left(\frac{d_{n2}^*}{d_{n1}^*}\right) - \frac{2x^* \tan\beta_2}{d_{n1}^*} \right]^2$$

$$\text{for } l_1^* < x^* \leq l_2^* \quad (\text{I.13})$$

Differentiating equation (I.13) with respect to  $x^*$  gives

$$\frac{dA_n^*}{dx^*} = - \frac{4 \tan\beta_2}{d_{n1}^*} \left[ \left(1 - \frac{d_{n2}^*}{d_{n1}^*}\right) \frac{\tan\beta_2}{\tan\beta_1} + \left(\frac{d_{n2}^*}{d_{n1}^*}\right) - \frac{2x^* \tan\beta_2}{d_{n1}^*} \right]$$

$$\text{for } l_1^* < x^* \leq l_2^* \quad (\text{I.14})$$

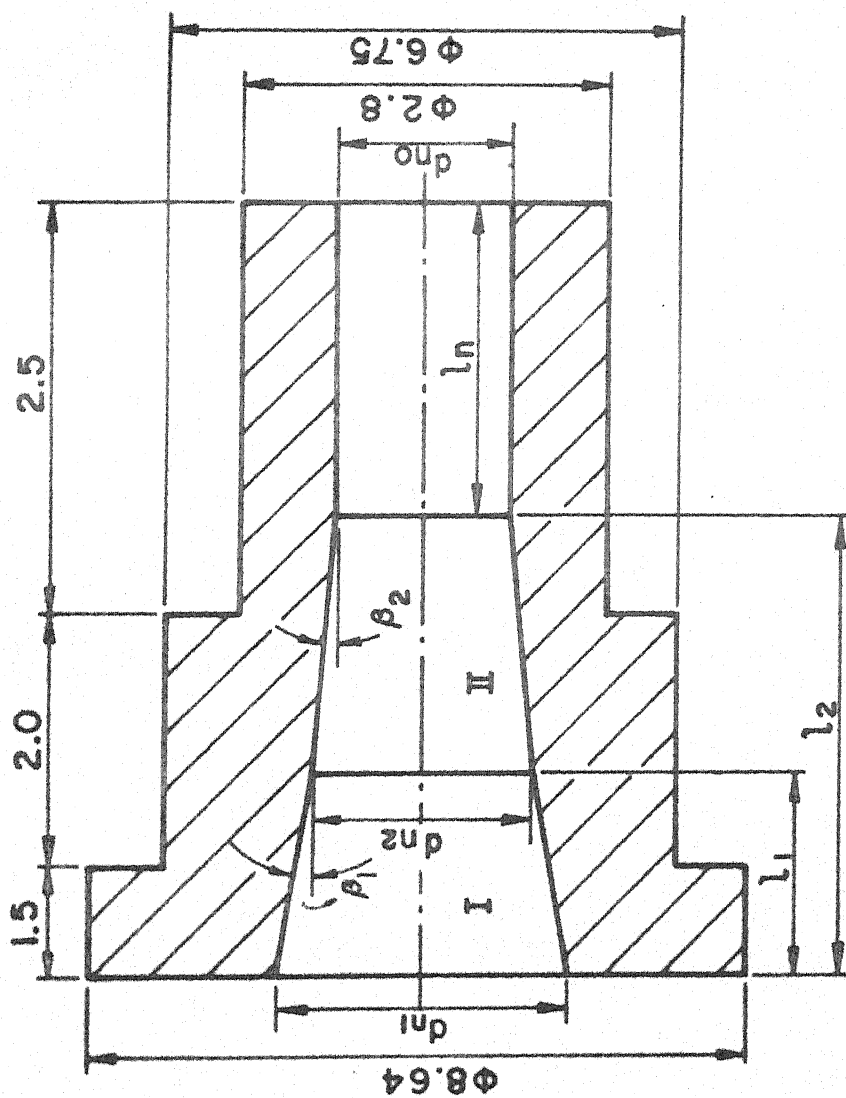
After II convergent region i.e., in the straight region of the flow passage the nozzle diameter is constant and is equal to the exit diameter of the nozzle  $d_{no}$ . In this region the nozzle flow area in dimensionless form can be expressed as

$$A_n^* = \left( \frac{1}{d_{n1}^*} \right)^2 \quad \text{for } x^* > l_2^* \quad (\text{I.15})$$

Differentiation of equation (I.15) with respect to  $x^*$  yields

$$\frac{dA_n^*}{dx^*} = 0 \quad \text{for } x^* > l_2^* \quad (\text{I.16})$$





$d_{n1} : 3 \text{ mm}$   
 $d_{n2} : 1.5 \text{ mm}$   
 $d_{n0} : 0.712 \text{ mm}$   
 $\beta_1 : 27.5^\circ$   
 $\beta_2 : 11.2^\circ$   
 $l_n : 2.57 \text{ mm}$

Fig. 1.1 Geometry of convergent-straight nozzle .

## APPENDIX - II

## MAXIMUM CONTACT FORCE DURING ELASTIC COLLISION

Using Hertz relation [108] the contact force  $F_e$  during elastic collision of a spherical particle with a flat body can be related to the elastic deformation depth  $z_e$ , impacting particle diameter  $d_p$  and elastic constants of the impacting particle and the target material as

$$F_e = z_e^{\frac{3}{2}} \left[ \frac{4}{3} \left( \frac{1}{\frac{1-\nu_t^2}{E_t} + \frac{1-\nu_p^2}{E_p}} \right) \right] \left( \frac{d_p}{2} \right)^{\frac{1}{2}} . \quad (\text{II.1})$$

During collision when the impacting particle comes in contact with the flat body, the compressive force  $F_e$  is set up which resists the penetration of the impacting particle into the target surface. The equation of motion of the colliding particle can be written as

$$\left( \frac{\pi}{6} d_p^3 \rho_p \right) \frac{du_p}{dt} = - F_e \quad (\text{II.2})$$

and the term  $\frac{du_p}{dt}$  as

$$\frac{du_p}{dt} = \frac{d}{dt} \left( \frac{dz_e}{dt} \right) = \frac{d^2 z_e}{dt^2} . \quad (\text{II.3})$$

Equations (II.1), (II.2) and (II.3) give

$$\frac{d^2 z_e}{dt^2} = -z_e^{\frac{3}{2}} \left[ \frac{4}{3} \left( \frac{1}{\frac{1-v_t^2}{E_t} + \frac{1-v_p^2}{E_p}} \right) \right] \left( \frac{d_p}{2} \right)^{\frac{1}{2}} / \left( \frac{\pi}{6} d_p^3 \bar{\rho}_p \right) . \quad (\text{II.4})$$

Multiplication of  $\frac{dz_e}{dt}$  on both sides of equation (II.4) gives

$$\frac{1}{2} d \left( \frac{dz_e}{dt} \right)^2 = - \frac{4\sqrt{2}}{\pi} \left[ \frac{1}{\left( \frac{1-v_t^2}{E_t} + \frac{1-v_p^2}{E_p} \right) (\bar{\rho}_p d_p^{\frac{5}{2}})} \right] z_e^{\frac{3}{2}} dz_e . \quad (\text{II.5})$$

When impacting particle touches the target surface, the deformation rate will be equal to the velocity of impingement and at full penetration the velocity becomes zero.

Thus the above equation (II.5) can be integrated as

$$\int_{u_p}^0 \frac{1}{2} d \left( \frac{dz_e}{dt} \right)^2 = - \frac{4\sqrt{2}}{\pi} \left[ \frac{1}{\left( \frac{1-v_t^2}{E_t} + \frac{1-v_p^2}{E_p} \right) (\bar{\rho}_p d_p^{\frac{5}{2}})} \right] \int_0^{(z_e)_{\max}} z_e^{3/2} dz_e . \quad (\text{II.6})$$

Here  $(z_e)_{\max}$  is the maximum value of elastic deformation depth at the end of impact cycle when particle velocity reaches a zero value. Integration of equation (II.6) gives

$$(z_e)_{\max} = \left[ \frac{5\pi \bar{\rho}_p}{16\sqrt{2}} \left( \frac{1-v_t^2}{E_t} + \frac{1-v_p^2}{E_p} \right) \right]^{\frac{2}{5}} d_p u_p^{\frac{4}{5}}. \quad (\text{II.7})$$

Substitution of  $z_e = (z_e)_{\max}$  in equation (II.1) gives

$$(F_e)_{\max} = \left( \frac{20\pi}{3} \bar{\rho}_p \right)^{\frac{3}{5}} d_p^2 \left[ \frac{1}{192 \left( \frac{1-v_t^2}{E_t} + \frac{1-v_p^2}{E_p} \right)} \right]^{\frac{2}{5}} u_p^{\frac{6}{5}}. \quad (\text{II.8})$$

## APPENDIX - III

## SALTATION VELOCITY FOR HORIZONTAL CONVEYING

The saltation velocity  $u_{gs}$  for horizontal conveying of solid particles can be estimated using the procedure presented by Zenz [115]. From Fig. III.1, the minimum velocity  $(u_{gs})_{\min}$  needed to convey a single particle of largest size is obtained. For this the constants  $A_3$  and  $A_4$  are evaluated using equations

$$A_3 = \left[ \frac{4 g_c \bar{\mu}_g (\bar{\rho}_p - \bar{\rho}_{gs})}{3 \bar{\rho}_{gs}^2} \right]^{\frac{1}{3}}, \quad \text{cm/sec} \quad (\text{III.1})$$

and

$$A_4 = \left[ \frac{3 \bar{\mu}_g^2}{4 g_c \bar{\rho}_{gs} (\bar{\rho}_p - \bar{\rho}_{gs})} \right]^{\frac{1}{3}}, \quad \text{cm} \quad (\text{III.2})$$

Here  $\bar{\mu}_g$  is the viscosity of the carrier fluid g/cm-sec,  $g_c$  is the acceleration due to gravity cm/sec<sup>2</sup>,  $\bar{\rho}_p$  is the material density of the solid particles g/cm<sup>3</sup> and  $\bar{\rho}_{gs}$  is the material density of the carrier fluid g/cm<sup>3</sup>.

In the present case aluminium oxide particles (max. 50  $\mu\text{m}$ ) are to be transported using air at the temperature of 30° and pressure of 0.5 MN/m<sup>2</sup> (abs) as carrier fluid.

For this condition the values of different variables used in equation (III.1) and (III.2) are

$$\bar{\mu}_g = 1.86 \times 10^{-4} \text{ g/cm-sec},$$

$$\bar{\rho}_{gs} = 57.44 \times 10^{-4} \text{ g/cm}^3,$$

$$\bar{\rho}_p = 3.85 \text{ g/cm}^3,$$

$$\text{and } g_c = 981 \text{ cm/sec}^2.$$

Using equations (III.1) and (III.2) the constants  $A_3$  and  $A_4$  for the above conditions are

$$A_3 = 30.792 \text{ cm/sec}$$

and

$$A_4 = 1.0516 \times 10^{-3} \text{ cm}.$$

For  $d_p = 0.005 \text{ cm}$ ,

$$\frac{d_p}{A_4} = \frac{0.005}{0.0010516} = 4.755$$

and from Fig. III.1 for spherical particles

$$\frac{(u_{gs})_{\min}}{A_3} = 4.76$$

which gives  $(u_{gs})_{\min} = 146.57 \text{ cm/sec}$ . Also from Fig. III.1 the slope of the tangent( $n_3$ ) on the considered curve at this point is zero. Since the data of Fig. III.1 pertains to the flow in 6.35 cm tube, the correct saltation velocity  $(u_{gs})'_{\min}$  for the actual size of the tube can be obtained from the following equation :

$$(u_{gs})'_{\min} = (u_{gs})_{\min} \left( \frac{d_t}{6.35} \right)^{0.4}, \quad (\text{III.3})$$

where  $d_t$  is the actual size of the tube.

In the present case the minimum diameter of the nozzle is 0.7 mm, the system inlet pressure and temperature are  $0.5 \text{ MN/m}^2$  (abs) and  $30^\circ\text{C}$ , the nozzle exit pressure and temperature are  $0.101 \text{ MN/m}^2$  (abs) and  $30^\circ\text{C}$ , respectively. The carrier fluid velocity at the nozzle exit in the present case is taken to be  $34000 \text{ cm/sec}$  (see Sec. 4.3). The continuity relation for the flow between nozzle exit and the tube gives

$$d_t = \left[ \frac{34000 (d_{no}^2 \bar{\rho}_{go})}{\bar{\rho}_{gs} (u_{gs})_{\min}} \right]^{\frac{1}{2}}, \quad (\text{III.4})$$

where  $d_{no}$  is the nozzle exit diameter in cm,  $\bar{\rho}_{go}$  is the density of carrier fluid in  $\text{g/cm}^3$  at nozzle exit conditions and  $\bar{\rho}_{gs}$  is the density of carrier fluid in  $\text{g/cm}^3$  at system working conditions in the tube.

Substitution of numerical values of  $\bar{\rho}_{go}$ ,  $d_{no}$ ,  $\bar{\rho}_{gs}$  and  $(u_{gs})_{\min}$  into equation (III.4) gives

$$d_t = \left[ \frac{34000 \times (0.07)^2 \times 1.164 \times 10^{-3}}{5.744 \times 10^{-3} \times 146.57} \right]^{\frac{1}{2}} = 0.48 \text{ cm}$$

From equation (III.3) the corrected value of minimum saltation velocity for the tube diameter ( $d_t$ ) of 0.48 cm is

$$(u_{gs})'_{\min} = 146.57 \left( \frac{0.48}{6.35} \right)^{0.4} = 52.17 \text{ cm/sec}.$$

This value of saltation velocity  $(u_{gs})'_{\min}$  pertains to single particle conveying which is further corrected for the actual mixture ratio through equation

$$\frac{\dot{M}_p}{\dot{M}_g} \left( \frac{\bar{\rho}_{gs}}{\bar{\rho}_p} \right) u_{gs} = A_5 \frac{[u_{gs} - (u_{gs})'_{\min}]}{(u_{gs})'_{\min}}, \quad (\text{III.5})$$

where  $\dot{M}_p$  is the mass flow rate of solid particle in g/sec and  $\dot{M}_g$  is the mass flow rate of carrier fluid in g/sec in the mixture. The constant  $A_5$  is

$$\begin{aligned} A_5 &= 21.4 n_3^{1.5} & \text{for } n_3 \geq 0.068 \\ &= 0.32 & \text{for } -0.11 \leq n_3 \leq -0.068 \end{aligned} \quad (\text{III.6})$$



For the value of mixture ratio considered ( $\alpha = 0.4$ ), the ratio  $\dot{M}_p/\dot{M}_g$  comes out to be 0.667. Since  $n_3 = 0$ , the constant  $A_5$  may be taken to be 0.32. Substitution of these values in equation (III.5) gives

$$0.667 \left( \frac{57.44 \times 10^{-4}}{3.965} \right) u_{gs} = 0.32 \frac{(u_{gs} - 52.17)}{52.17},$$

which after solution gives  $u_{gs} = 61.93$  cm/sec. Thus, in the present case to transport 50  $\mu$ m diameter aluminium oxide spherical particles of uniform size through a horizontal tube at mixture ratio ( $\alpha$ ) of 0.4, the saltation velocity comes out to be 0.62 m/sec.

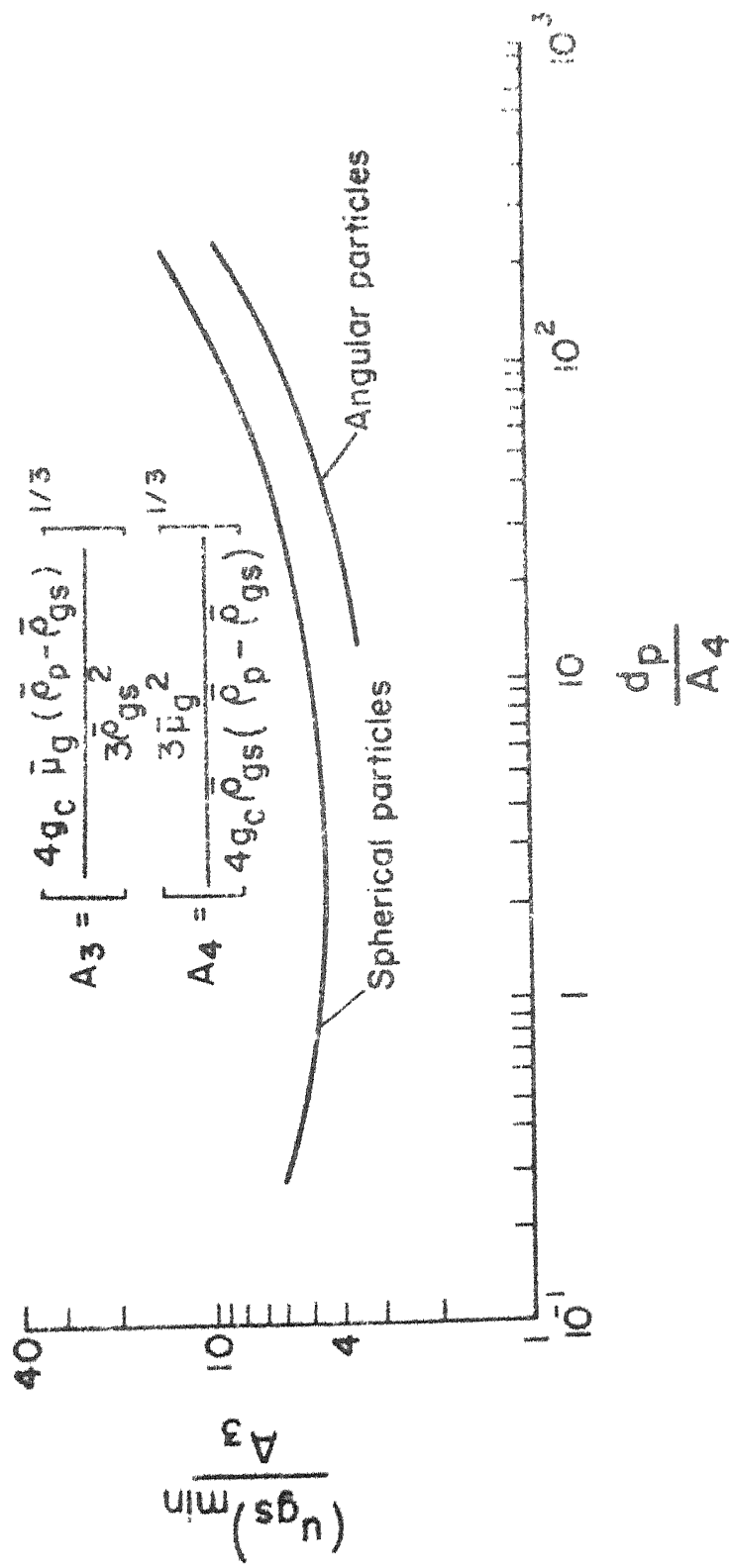


Fig. III. 1 Saltation velocity  $(u_{gs})_{min}$  of uniform sized solid particles in a 6.35 cm ID tube [After Zenz (115)].

## APPENDIX - IV

## DESIGN OF MIXING CHAMBER AND MIXTURE CONVEYING TUBE

The present set-up has been designed for the system inlet pressure of  $0.5 \text{ MN/m}^2$  (abs) and temperature of  $30^\circ\text{C}$  at which the carrier fluid (air) density  $\bar{\rho}_{gs} = 5.744 \times 10^{-3} \text{ g/cm}^3$ . The exit pressure and temperature are  $0.101 \text{ MN/m}^2$  (abs) and  $30^\circ\text{C}$ , respectively at which carrier fluid density  $\bar{\rho}_{go} = 1.164 \times 10^{-3} \text{ g/cm}^3$ . The minimum size of the nozzle for which the set-up is to be designed is  $0.07 \text{ cm}$ . As mentioned in Sec. 4.3 the exit velocity of the carrier fluid for the above stated conditions of flow is  $34000 \text{ cm/sec}$  at the nozzle exit. The minimum safe velocity of the carrier gas in the mixing chamber ( $u_{gch}$ ) and the mixture conveying tube ( $u_{gst}$ ) are  $62 \text{ cm/sec}$  and  $362 \text{ cm/sec}$ , respectively (see Sec. 4.3).

The continuity relation for the flow between nozzle exit and mixing chamber gives

$$d_m = \left[ \frac{34000 d_{no}^2 \bar{\rho}_{go}}{\bar{\rho}_{gs} u_{gch}} \right]^{\frac{1}{2}}, \quad (\text{IV.1})$$

where  $d_m$  is the diameter of the mixing chamber in cm.

Substitution of the numerical values of  $d_{no}$ ,  $\bar{\rho}_{go}$ ,  $\bar{\rho}_{gs}$  and  $u_{gch}$  in equation (IV.1) gives

$$d_m = \left[ \frac{34000 \times (0.07)^2 \times 1.164 \times 10^{-3}}{5.744 \times 10^{-3} \times 62} \right]^{\frac{1}{2}}$$

$$= 0.7379 \text{ cm.}$$

The safe value for the mixing chamber diameter is 7.3 mm.

Similarly the continuity relation for the flow between mixture conveying tube and nozzle exit gives

$$d_{mt} = \left[ \frac{34000 d_{no}^2 \bar{\rho}_{go}}{\bar{\rho}_{gs} u_{gst}} \right]^{\frac{1}{2}}, \quad (\text{IV.2})$$

where  $d_{mt}$  is the mixture conveying tube diameter in cm.

Substitution of numerical values of the variables in equation (IV.2) gives

$$d_{mt} = \left[ \frac{34000 \times (0.07)^2 \times 1.164 \times 10^{-3}}{5.744 \times 10^{-3} \times 362} \right]^{\frac{1}{2}}$$

$$= 0.3054 \text{ cm.}$$

Thus, the safe value for the mixture conveying tube diameter is 3 mm.

## APPENDIX - V

## CALCULATION OF MIXTURE RATIO

The manufacturer's calibration of the flow meter for air at 30°C temperature indicates 1 division (1 mm) to be 50.39 ml/min at system pressure of 372.454 kN/m<sup>2</sup> (gauge) and 51.92 ml/min at system pressure of 344.863 kN/m<sup>2</sup> (gauge). The air density  $\bar{\rho}_g$  is given by

$$\bar{\rho}_g = \frac{0.001293}{(1 + 0.00367 T)} \cdot \left(\frac{P}{76}\right) \quad , \quad (V.1)$$

where P is the pressure in terms of cm of mercury and T is the temperature in °C. For 30°C temperature equation (V.1) gives  $\bar{\rho}_g = 51.265 \times 10^{-4}$  g/ml at a pressure of 344.863 kN/m<sup>2</sup> (gauge) and  $\bar{\rho}_g = 54.435 \times 10^{-4}$  g/ml at a pressure of 372.453 kN/m<sup>2</sup> (gauge).

From manufacturer's calibration chart supplied with the meter the equivalent number of divisions (mm) are obtained for the flow meter reading (reading at the centre of flow meter ball) which for appropriate values of system pressure with corresponding values of density gives the air flow rate in g/min. Using equation (1.1) the mixture ratio can be obtained for the known mass flow rate of abrasive particles.

## APPENDIX - VI

## PARTICLE VELOCITY RATIO AT NOZZLE INLET

Using equation (2.2) and (2.3) the motion of spherical particle (following the particle path) in a uniform stream of gas can be expressed as

$$\frac{du_p}{dt_p} = \frac{3}{4} \left( \frac{\bar{\rho}_g}{\bar{\rho}_p} \right) \left( \frac{C_d}{d_p} \right) (u_g - u_p)^2 \quad (\text{VI.1})$$

The solution of equation (VI.1) for particle initially at rest ( $x=0$ ,  $t_p=0$ ,  $u_p=0$ ) is

$$x = \frac{1}{\xi} \left[ \left( \frac{u_p}{u_g - u_p} \right) - \ln \left( \frac{u_g}{u_g - u_p} \right) \right], \quad (\text{VI.2})$$

$$\text{where } \xi = \frac{3}{4} \left( \frac{\bar{\rho}_g}{\bar{\rho}_p} \right) \frac{C_d}{d_p}, \quad (\text{VI.3})$$

and  $x$  is the distance required to accelerate the particle from zero velocity to a velocity  $u_p$ .

Equation (VI.2) can be rewritten as

$$\frac{u_p}{u_g} \left( 1 - \frac{u_p}{u_g} \right)^{-1} + \ln \left( 1 - \frac{u_p}{u_g} \right) = x\xi. \quad (\text{VI.4})$$

In the present study for  $\dot{M}_p = 4.973 \times 10^{-5} \text{ kg/sec}$   
 $\alpha = 0.148$ ,  $T_{g1} = 303^\circ\text{K}$ ,  $P_1 = 24.8536 \times 10^4 \text{ N/m}^2 \text{ (abs)}$ ,  
 $\bar{\mu}_g = 0.186 \times 10^{-4} \text{ N s/m}^2$ ,  $d_{nl} = 3 \times 10^{-3} \text{ m}$ , equation  
(2.66) gives  $u_{g1} = 14.17 \text{ m/sec}$  and equation (2.67) gives  
 $\rho_{g1} = 2.858 \text{ kg/m}^3$ . For aluminium oxide particles with  
material density  $\bar{\rho}_p = 3850 \text{ kg/m}^3$  and  $30 \text{ }\mu\text{m}$  size, equation (2.5)  
gives the particle Reynold's number  $N_{Re} = 65.32$ . Equations  
(2.6) and (2.7) give the corrected drag coefficient  $C_d = 1.28$ .  
Substitution of this value of  $C_d$  in equation (VI.3), gives  
 $\xi = 23.75$ .

The tube length for conveying air-abrasive mixture  
from mixing chamber to nozzle inlet is  $0.5 \text{ m}$  (i.e.  $x=0.5 \text{ m}$ ).  
Thus, for  $x = 0.5 \text{ m}$  and  $\xi = 23.75$ , equation (VI.4) gives  
the particle velocity ratio  $c_s$  as

$$c_s = \frac{u_p}{u_g} \approx 0.935 \quad . \quad (\text{VI.5})$$

## APPENDIX -- VII

INPUT PARAMETERS FOR THEORETICAL EVALUATION  
OF PARTICLE VELOCITY AND EROSION RATE

## Carrier Fluid

Carrier gas	:	Air
Gas constant ( $R_g$ )	:	287 J/kg <sup>o</sup> K
Nozzle pressure ( $P_1$ )	:	248.475 kN/m <sup>2</sup> (abs)
Inlet temperature ( $T_{g1}$ )	:	303 <sup>o</sup> K
Viscosity ( $\bar{\mu}_g$ )	:	1.86 x 10 <sup>-5</sup> N s/m <sup>2</sup>
Thermal conductivity ( $k_g$ )	:	26.753 x 10 <sup>-3</sup> J/m s <sup>o</sup> K
Specific heat ( $c_{pg}$ )	:	1004.6 J/kg <sup>o</sup> K
Density at nozzle exit ( $\bar{\rho}_{g0}$ )	:	1.164 kg/m <sup>3</sup>
Prandtl number ( $N_{Pr}$ )	:	0.701

## Abrasive Particles

Type	:	Aluminium oxide
Modulus of elasticity ( $E_p$ )	:	36.55 x 10 <sup>10</sup> N/m <sup>2</sup>
Poisson's ratio ( $\nu_p$ )	:	0.25
Material density ( $\bar{\rho}_p$ )	:	3850 kg/m <sup>3</sup>
Specific heat ( $c_{pp}$ )	:	795.5 J/kg <sup>o</sup> K
Particle temperature ( $T_{p1}$ )	:	303 <sup>o</sup> K



## Work Material

Type	: Glass
Modulus of elasticity ( $E_t$ )	: $6.9 \times 10^{10} \text{ N/m}^2$
Fracture toughness ( $K_c$ )	: $7.5 \times 10^5 \text{ N/m}^{3/2}$
Vicker's hardness ( $H_t$ )	: $5.6 \times 10^9 \text{ N/m}^2$
Shear modulus ( $G_t$ )	: $2.76 \times 10^{10} \text{ N/m}^2$
Poisson's ratio ( $\nu_t$ )	: 0.25

---

S.No.	Mass flow rate of particles (kg/sec)	Mixture ratio
1.	$3.193 \times 10^{-5}$	0.095
2.	$4.974 \times 10^{-5}$	0.148
3.	$6.755 \times 10^{-5}$	0.201
4.	$9.000 \times 10^{-5}$	0.268

---

